Université catholique de Louvain
Secteur des Sciences et Technologies
Faculté des bioingénieurs
Louvain Institute of Biomolecular Science & Technology
Nanobiophysics lab

Study of the binding of viral glycoproteins by atomic force microscopy: application to Ebola and SARS-CoV-2

Thesis submitted to fulfil the requirements for the degree of Philisophae Doctor in Bio-engineering of the Université catholique de Louvain

Qingrong Zhang

Supervisor:
Prof. David Alsteens, Université catholique de Louvain

Members of the examination Committee:
Prof. Michel Ghislain, Université catholique de Louvain (President)
Prof. Yves Dufrêne, Université catholique de Louvain
Prof. Patrice Soumillon, Université catholique de Louvain
Prof. Christian Sieben, Helmholtz centre for Infection Research, Germany
Dr. Vincent Duprès, Université de Lille, France

Louvain-la-Neuve, November 2023

Acknowledgements

I have completed my doctoral training after four years of study. It is time for me to thank everyone who helped me in my early academic career and supported me along the way.

First and foremost, I would like to thank my PhD supervisor, Professor David Alsteens. Thank you for creating a lab with such positive energy and a great atmosphere, which has benefited my PhD career. When I applied for my PhD, you generously accepted me and lived with my language and technical deficits. This gave me the confidence to start my early academic career. During my PhD training, you gave me great freedom and allowed me to explore any projects I was interested in, which encouraged me to adopt independent thinking. More importantly, thanks to your high level of professionalism and profound knowledge, you always helped me overcome challenges when my project encountered them. This has helped me to strengthen my knowledge system so that I can deal with problems when they arise in my future academic career. I will benefit from your comprehensive knowledge, unselfish mentoring, rigorous academic approach, flexible mindset, and effective working style throughout my academic career.

Many thanks to all the members of the jury: Professor Patrice Soumillion, Professor Yves Dufrêne, Professor Christian Sieben, and Doctor Vincent Dupres for their careful and critical reading of my thesis manuscript and for their constructive suggestions for relevant changes. Among them are Professor Yves Dufrêne and Professor Patrice Soumillion, who were members of my support committee and provided me with their expertise in carrying out this work. Many thanks to Professor Michel

Ghislain, who agreed to serve as president of the jury and expertly chaired the session during the two defense proceedings.

I would like to thank all the members of the nBio lab, including Rita, Ankita, Jinsung, Joshua, Melanie, Andra, Simon, Cristina, Gol, Irem, Federico, Deven, Paloma, Bhanu, Savannah, Sylvie, Céline, Kim, Marie, Sueli, Marion, Constance, Albertus, Can, Telmo and others, for their constant care and support. Special thanks to Ankita and Joshua for their great contributions to the revision of the thesis manuscript. Gol, Jinsung, Rita, Melanie and Simon, Ankita, who skilfully contributed to my thesis and taught me a lot with their optimistic attitude and insightful questions. Many thanks to Sylvie, Kim, Marie, and Sueli for their availability and technical help since the beginning of my work and to Céline for her frequent administrative support.

Thank you also to Professor Zongqiang Cui for the very rewarding collaboration that made this research possible and for all that you contributed to this work

My heartfelt thanks go to my sister who has meant so much to our family. You have helped me with many family responsibilities and supported me in an incomparable way so that I could work in peace. Thank you to my parents for their endless love and support.

A special thanks to my partner, Zehan. I could not possibly list everything for which I am grateful. In short, I appreciate your help, your advice, your company, and your contribution to my balance inside and outside the lab.

Finally, I would like to thank my family, mentors, and friends for their presence and support, which have made these years of work so enjoyable.

Abstract

A multitude of human diseases stem from infections caused by enveloped viruses. For enveloped viruses, the infection begins with virions attaching to the surface of host cells, and then sets off a fusion process between viral and cellular membranes, enabling the viruses to penetrate the host cells. Grasping the molecular intricacies of how enveloped viruses enter cells is of utmost importance for the advancement of novel vaccines and therapeutics targeted at this process. Despite the wealth of insights provided by experimental studies into the entry of enveloped viruses, the finer details of their molecular mechanisms, particularly their dynamic aspects, remain significantly underexplored.

This thesis centers around unraveling the kinetics and thermodynamics involved in the process of enveloped viruses entering cells. The approach taken involves utilizing atomic force microscopy (AFM)-based single molecule force spectroscopy (SMFS) to investigate the interaction between viruses and receptors at an individual virus level. Notably, a specialized AFM-SMFS operating in height-clamp mode was developed to dissect the binding of fusion peptides to the lipid membrane.

We initially studied Ebola virus (EBOV) binding to vital receptors: the C-type lectin dendritic cell-specific intercellular adhesion molecule-3-grabbing nonintegrin receptor (DC-SIGNR) and the T-cell Ig and mucin domain 1 (TIM-1). We demonstrated that EBOV, activated by host enzymes, exhibits a preference for binding to TIM-1 over DC-SIGNR. TIM-1, binding to glycoprotein or phosphatidylserine in the envelope, functions as a dual-receptor for EBOV. Through analysis of kinetics and

thermodynamics at the single virus level, we confirmed EBOV's strong affinity for both receptors.

Our subsequent focus was on the interaction between the fusion peptide of Severe Acute Respiratory Syndrome Coronavirus 2 (SARS-CoV-2 FP) and the host membrane. We demonstrated that cholesterol within the membrane, as opposed to sphingomyelin, increases the affinity of SARS-CoV-2 FP binding to the lipid membrane. Notably, the internal disulfide bond of SARS-CoV-2 FP was found to play a crucial role in enhancing its binding to the membrane—a conclusion supported by single-molecule kinetics and thermodynamics analyses. Additionally, we observed effective inhibition of SARS-CoV-2 infection through cholesterol removal from target cell membranes.

In summary, this thesis uncovers new insights into enveloped virus entry mechanisms, spanning different steps and viruses. Additionally, the AFM experiments and theories introduced could have broader applications in studying novel virus-cell interactions and protein-membrane processes.

List of abbreviations

ACE2	angiotensin-converting enzyme 2
AFM	atomic force microscopy
AM	amplitude modulation
BE	Bell-Evans model
BLI	biolayer interferometry
Cat-B/L	cathepsin-B and cathepsin-L
Chol	cholesterol
COVID-19	coronavirus disease 2019
DC-SIGNR	C-type lectin dendritic cell-specific intercellular adhesion molecule-3-grabbing nonintegrin receptor (also called L-SIGN)
DFS	Dynamic force spectroscopy
DHS	Dudko, Hummer, and Szabo model
DOPC	1,2-dioleoyl-sn-glycero-3-phosphocholine
EBOV	Ebola virus
EDC	1-Ethyl-3-[3-dimethylaminopropyl] carbodiimide hydrochloride
FD	force-distance curve
FNdY	Friddle-Noy-de Yoreo model
FP	fusion peptide
FV	Force-volume
GP	glycoprotein
HSV	herpes simplex virus
HVEM	herpesvirus entry mediator
K_D	dissociation constant
k_{off}	kinetic off-rate
k_{on}	kinetic on-rate
MβCD	Methyl-β-cyclodextrin
NHS	N-hydroxysulfosuccinimide
pN	piconewton
PS	Phosphatidylserine
RBD	receptor-binding domain

S	spike protein of SARS-CoV-2
SARS-CoV-2	Severe Acute Respiratory Syndrome Coronavirus 2
SM	sphingomyelin
SMFS	single-molecule force spectroscopy
STaSI	step transition and state identification
SVFS	single-virus force spectroscopy
TACE	tumor necrosis factor-α converting enzyme
TCEP	Tris(2-carboxyethyl)phosphine hydrochloride
TIM-1	T-cell Ig and mucin domain 1
TMPRSS2	transmembrane protease serine 2
VLP	virus-like particle
VSV	vesicular stomatitis virus
WE	Williams-Evans model
x_β	free-energy barrier
τ	lifetime

Foreword

Pandemics are among the greatest global challenges, causing massive economic losses and posing a serious threat to human life and health. These pandemics are caused by viruses, most of which are enveloped viruses, including the Ebola virus and Severe Acute Respiratory Syndrome Coronavirus 2 (SARS-CoV-2). Infection with enveloped viruses begins when the virus enters a host cell. Understanding the molecular mechanisms of enveloped viruses during cell entry, therefore, helps to address current challenges. Although structural and molecular ensemble studies have characterized the entry process of these viruses and provided a wealth of insights into the interactions between the viruses and the target cells, the molecular mechanisms of entry into the cell have not yet been elucidated. In this context, the aim of my thesis is to investigate the molecular mechanisms of these viruses during cell entry. I have studied the interactions of Ebola virus with receptors and the effects of host protease during these interactions. In particular, I studied the fusion peptide of SARS-CoV-2 that binds to the host membrane. Consequently, the work focused on the specific kinetics and thermodynamics of these processes to elucidate and focus knowledge on the entry of the enveloped virus.

Table of Contents

Chapter 1:

General introduction

This section outlines the two main scientific topics that support this work: i) the general mechanisms of enveloped virus entry into host cells, ii) and the use of atomic force microscopy (AFM) to investigate the early binding steps to host cells at the single virus level. In the frame of this thesis, we will focus on studying the molecular mechanisms of receptors-binding and membrane fusion of the Ebola virus (EBOV) and the Severe Acute Respiratory Syndrome Coronavirus 2 (SARS-CoV-2). Moreover, state-of-the-art concepts related to the theory and principle of AFM and the study of viral infections at the single molecule level are presented.

1.1 Entry mechanism of enveloped viruses

General features of viruses

Viruses exist in all aspects of our environment, including atmosphere, seawater, and minute soil particles. Since the discovery of the first tobacco mosaic virus in 1898, a causative agent of disease that infects tobacco plants, more than 10,000 of the millions of virus species have been described in details (*1*). Considered non-living organisms, viruses are infectious agents that exclusively depend on living cells, including bacteria, plants, and mammals in order to replicate. Examples of common human diseases caused by viruses include Influenza, Common cold, Lassa fever, and Varicella (*2*), as well as many serious diseases such as Smallpox, Rabies, Acquired Immunodeficiency Syndrome, Ebola virus disease, and

COVID-19, are also caused by viruses (*3*). A viral disease (or viral infection) occurs when an organism is invaded by pathogenic viruses, and the infectious virus particles (virions) succeed in binding to and entering susceptible cells. In this context, better understanding the molecular mechanisms utilized by viruses to obtain access to the cell interior is a critical research issue.

Once inside the cell, viruses hijack the replication machinery of the host and use it to generate the necessary proteins and nucleic acids for assembling new virus particles. These molecules are produced based on the viral genetic material, which contains all the information needed to generate descendant virus particles. This genetic material can be either deoxyribonucleic acid (DNA) or ribonucleic acid (RNA). Viruses have a diverse collection of genomes that vary in size, ranging from 1,000 to 250,000 nucleotides. These genomes can exist in either circular forms or linear forms, as seen in human papillomavirus and herpes viruses respectively (*4*). Furthermore, the size of the viral genome has a direct influence on the size and shape of viral particles (*5*) Therefore, the wide range of virus genome sizes results in a diverse range of particle sizes and structures (*5, 6*). For example, SARS-CoV-2 is spherical with a diameter of 80-100 nm and EBOV is filamentous with a total length of up to 1400 nm and diameters of only about 80 nm (*7*).

As the viral genetic material is fragile, it is enclosed within an architecture of protein capsids to shield it from potential harm that may be caused by physical and chemical factors, such as nucleases and radiation. The packaging strategies of viruses are generally related to the type of genome. For instance, a molecular motor is used to pack the genomes of double-stranded DNA viruses into their capsid shell, and a

cooperative mechanism is employed to assemble the genomes of single-stranded DNA or RNA (*8*). The capsid proteins and their packaged genomes ultimately dictate the characteristics of geometry and size.

Notably, most viruses are considerably smaller than bacteria and cells, it can only be visualized using high-resolution imaging instruments such as transmission electron microscopes (*9*). Further classification of viral particles is employed based on the presence or absence of an outer lipid bilayer, derived from the host cell membrane, known as a viral envelope that surrounds the whole capsid. Those virus particles possessing a lipid coating are referred to as enveloped viruses, while those without are labelled non-enveloped viruses (**Figure 1.1**).

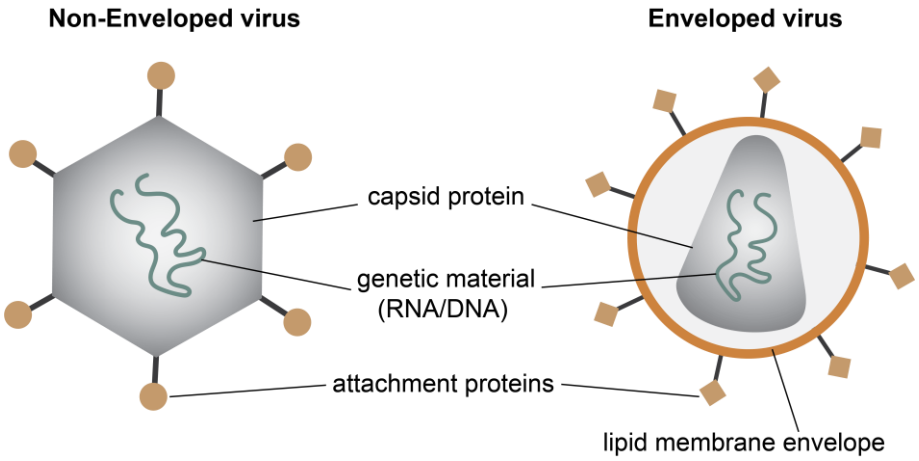

Figure 1.1: Schematic showing basic features of non-enveloped (left) and enveloped (right) virus particles. Non-enveloped viruses are constituted of nucleic acid shielded by capsid proteins, of particular note are the surface attachment proteins. In enveloped viruses, the capsid is surrounded by a lipid bilayer envelope in which attachment proteins are embedded (*10*).

The viral envelope consists of phospholipids and neutral lipids (predominantly cholesterol) derived from host cell membranes during the assembly and budding phases of the viral lifecycle. The viral proteins only associate with particular lipids during budding, thus even while all of the lipids in the viral envelope come from the cell, their relative proportions do not necessarily match those in the cell membrane (*11*). Moreover, the viral surface is decorated with particular attachment proteins (either a capsid protein for the non-enveloped viruses or an envelope glycoprotein for the enveloped viruses), which usually play a significant role in the initial stages of viral attachment to host cells. These viral attachment proteins play a crucial function in targeting and recognition of host cell receptors required for surface adhesion and cellular internalization.

The interaction between viruses and cell surfaces is a complex cascade involving a spectrum of specificity levels (*12*). At the outset, these interactions are relatively non-specific in nature, primarily serving to bring the virus in close proximity to the cell surface. They also facilitate the virus's diffusion along glycan structures that coat the cell membrane, creating a conducive environment for the next steps of infection.

In the early stages of this interaction, viruses typically engage with low-affinity, non-specific primary receptors (*12-14*). These primary receptors are often broadly distributed on the cell surface and exhibit a general affinity for viral particles. An example of such a primary receptor is heparan sulfate proteoglycan, which is found on the surface of many cells. Viruses, such as herpes simplex virus (HSV), initially interact with heparan sulfate proteoglycans (*15, 16*), allowing them to attach to the cell surface.

Once tethered to the cell surface, the virus then begins its quest for a specific secondary receptor (*12*). This secondary receptor is characterized by a higher affinity for the virus and is essential for mediating the virus's entry into the host cells. For instance, in the case of HSV, the virus eventually encounters a specific secondary receptor known as herpesvirus entry mediator (HVEM) (*17*). This interaction is much more selective and tightly regulated, ensuring that the virus gains access only to host cells that express the appropriate secondary receptor.

The engagement of the virus with this specific secondary receptor triggers a series of events, such as conformational changes in viral envelope proteins or the activation of cellular signaling pathways (*12*, *18*). These processes are instrumental in facilitating viral entry into the cell, initiating replication, and ultimately enabling the virus to complete its infectious life cycle.

Host tropism and receptors of enveloped viruses

Individual virus taxa are only able to infect a limited range of host cells and/or tissues, depending on the availability of key cell surface factors and receptors. This selectivity and specificity are referred to as viral tropism and is the reason that without the accrual of mutations, infection is frequently limited to one or two host species. Over the course of evolution, each virus has developed tailored strategies to first bind the cell surface and hijack host cell machinery, enabling cell entry and subsequently replication within the cytoplasm. In most cases, the host tropism of viruses for their specific host(s) relies on two factors: the viral attachment proteins (from this point forward, referred to as glycoproteins) and the receptors present on host cells.

In addition to glycoproteins, a lipid membrane surrounds the exterior of enveloped viruses. The ability of enveloped viruses to penetrate host cells and infect them is commonly connected to membrane characteristics (e.g. lipids and glycoproteins), because viruses employ them to recognize host cell receptors and initiate internalization into host cells. Moreover, the viral lipids and glycoproteins have a significant impact on different phases of viral life cycles, such as helping adenovirus and influenza virus to evade the host immune system (*19, 20*).

Productive infection of enveloped virus is initiated through the landing of a virus particle to a cell surface. During this phase, viral surface components (either viral glycoproteins or lipids) contact the cell surface and bind to attachment factors (such as heparan sulfate proteoglycans and other glycans) (*21*). These interactions are currently thought to be nonspecific in the initial stages, being driven by electrostatic forces that serve as the foothold for the virus to eventually find and bind to specific entry receptors. The nonspecific attachment of the virus to the surface of the cell allows for lateral diffusion across the outer membrane, eventually leading it to encounter specific entry receptors consequently activating viral entry pathways. For instance, the attachment of the vesicular stomatitis virus is made stronger by a specific phospholipid known as monoacylglycerol (*22*). The glycoprotein of the human immunodeficiency virus (HIV) connects to cell surfaces through cell adhesion factors, such as integrins and intercellular adhesion molecules (**Figure 1.2**) (*23*). Once bound, the virus subsequently recruits and attaches to protein receptors (CD4) and chemokine co-receptors (CCR5/CXCR4) before initiating membrane fusion (**Figure 1.2**) *(24)*. In the case of influenza viruses, the first step in entry and infection involves binding to sialylated glycan

receptors on host cells using glycoproteins and glycolipids (**Figure 1.2**) (*25*). Consequently, the specialized surface membrane lipids and glycoproteins of enveloped viruses play a role in the initial interactions of the virus and the host cell surface.

Usually found in the inner leaflet of living cell membranes (*26*) and exposed on the cell surface upon cell death, phosphatidylserine (PS) is a lipid component recognized by circulating phagocytes in order to clear apoptotic debris through employing various types of PS-binding receptors (*27*). This PS also accumulates within viral envelopes and can in turn be used to exploit various types of host PS-recognizing molecular mechanisms to facilitate the early binding steps of virus, such as T cell immunoglobulin mucin protein family (TIMs) *(28)*. These proteins have become recognized as a novel group of cell surface proteins that may play a role in controlling different physiological functions that may be exploited by viruses (*29*). Two specific proteins, TIM-1 and TIM-4, have been found to interact with viral PS, which enables them to facilitate the absorption of dying cells (**Figure 1.2**) (*30*) and enhance the infection caused by various types of enveloped viruses (*31, 32*). Protein S and Gas6, vitamin K-dependent proteins with high structural homology (*33*), have also been found tho play a crucial role in attaching viruses to the surface of cells. They act as bridges between the viral PS molecule on the viral membrane and the TYRO3-AXL-MERTK (TAM) receptors on the cell surface (*34, 35*). Additionally, some enveloped viruses can employ another type of lipid, phosphatidylethanolamine (PE), to engage the PE-binding receptor CD300A, allowing them to adhere to host cells, such as Dengue Virus (*36*). In addition to particular proteins and lipids found on the viral surface, glycans on glycoproteins can be extremely important in

pathophysiological processes.

More generally, enveloped viruses have proteins on their surface that are highly glycosylated. These glycans are modified on the viral proteins during post-modification of proteins after synthesis by the host cell. Early binding steps of numerous enveloped viruses rely on the interaction between glycosylation of viral proteins and glycan-binding receptors of host cells. A subfamily of glycan-binding receptors known as C-type lectin receptors (CLRs) have a structurally conserved carbohydrate-recognition domain (CRD) involved in the binding to glycans (**Figure 1.2**). CLRs have a crucial function in the infection process of many enveloped viruses. For instance, DC-SIGN and DC-SIGNR, belonging to the CLRs family, enhance infection and dissemination of Marburg virus, SARS-CoV-2, and Ebola virus (EBOV) by binding to the viral glycoprotein (*37*). HIV attaches to the host cell surface via the lectins Langerin and macrophage mannose receptors (*38*), and the asiaglycoprotein receptor also interacts with the hepatitis B and C viruses (*39, 40*), demonstrating that numerous viruses employ lectin binding to promote their infectivity (**Figure 1.2**).

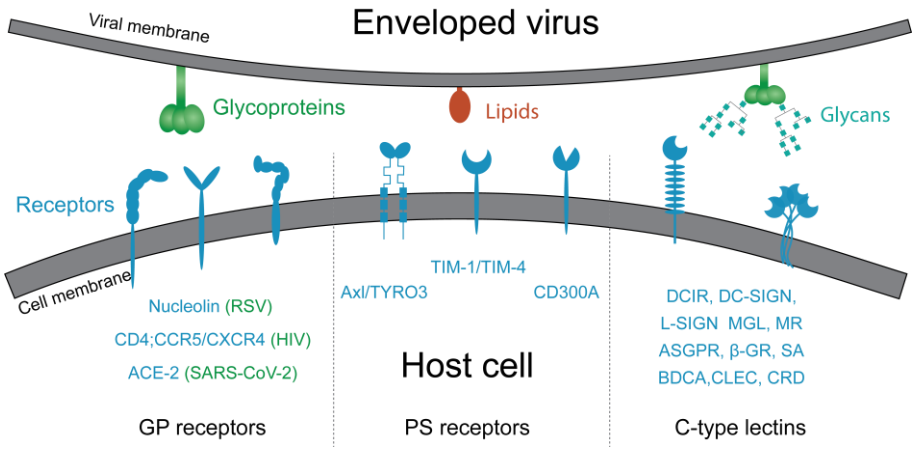

Figure 1.2: Examples of attachment factors and entry receptors utilized by select enveloped viruses. The specialized surface glycoproteins and lipids of enveloped viruses, as well as the glycans on glycoproteins, bind to the specialized receptors on the cell surface to trigger viral infection and endocytosis. Abbreviations: CD4, cluster of differentiation 4; CCR5, C-C chemokine receptor type 5; CXCR-4, C-X-C chemokine receptor type 4; ACE2, angiotensin-converting enzyme 2; Axl/TYRO3, tyrosine-protein kinase receptor encoded by the Axl/TYRO3 gene; TIM-1/TIM-4, T-cell immunoglobulin and mucin domain 1/4; CD300A, cluster of differentiation 300A; DCIR, dendritic cell immunoreceptor; DC-SIGN, dendritic cell-specific intercellular adhesion molecule-3-grabbing non-integrin; L-SIGN, c-type lectin domain family 4 member M encoded by the CLEC4M gene; MGL, Monoglyceride Lipase; MR, mannose receptor; ASGPR, asialoglycoprotein receptors; β-GR, glucocorticoid receptor β; SA, salicylic acid receptors; BDCA, blood DC antigen; CLEC, C-type lectin receptor; CRD, carbohydrate recognition domain.

Mechanisms involved in infections by enveloped virus

Enveloped viruses rely on host cells for metabolic and replication functions during their life cycle, as they are obligate intracellular parasites (*41*). Although enveloped viruses vary widely in terms of host species and viral taxon, generally most undergo the same fundamental steps of the viral life cycle. The life cycle of an enveloped virus can be conceived of in several major stages: attachment, entry, uncoating, replication, assembly, and release/budding (**Figure 1.3**).

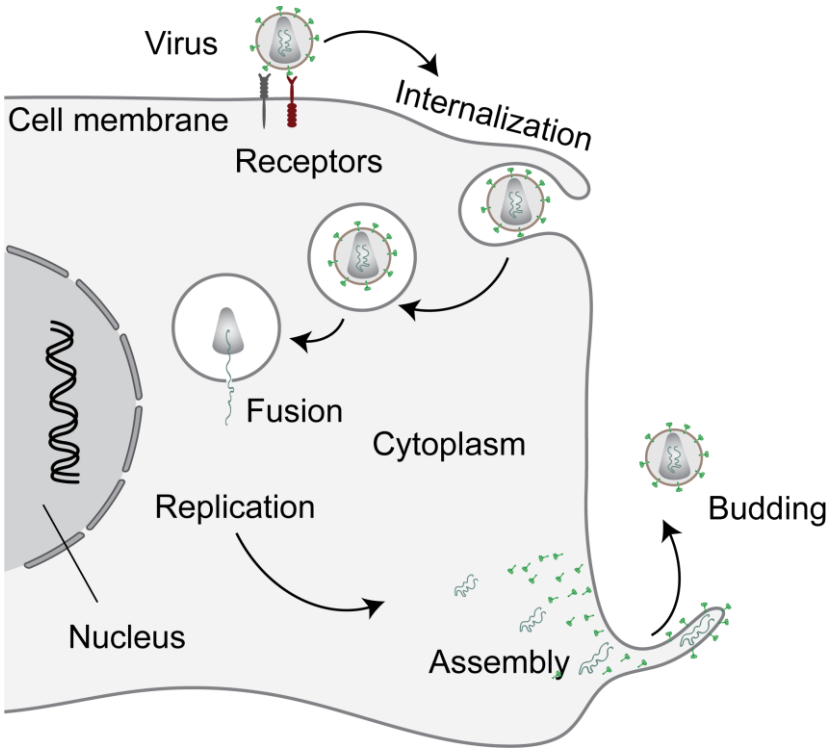

Figure 1.3: A classic schematic of the viral life cycle. Virions bind to a target receptor and fuse with the host cell membrane allowing it to internalize into the cell. After fusion, the viral genome is replicated in cytoplasm or nucleus, viral proteins are produced, and subsequently undergo assembly with the viral genome. Homogeneous mature virus particles undergo and then egress through the cellular membrane.

To begin the infective cycle, an enveloped virus has to release its genetic material into its host cell. As previously mentioned, viral invasion begins when the lipids or glycoproteins of the viral envelope bind to specific factors on the host cell surface (*42*). By this way, virus particles are concentrated on the cells surface by a variety of attachment factors, and then brought into close proximity to more specific receptors responsible for virus entry into host cells. Those specific receptors interact with the enveloped virus through their glycoproteins or lipids. As a result of these interactions, multiple cellular signaling pathways are triggered. The enveloped viruses are internalized via one of several endocytic mechanisms, including cell membrane fusion, clathrin or caveolin-mediated endocytosis, clathrin-independent endocytosis, or macropinocytosis (*43*) (**Figure 1.4**).

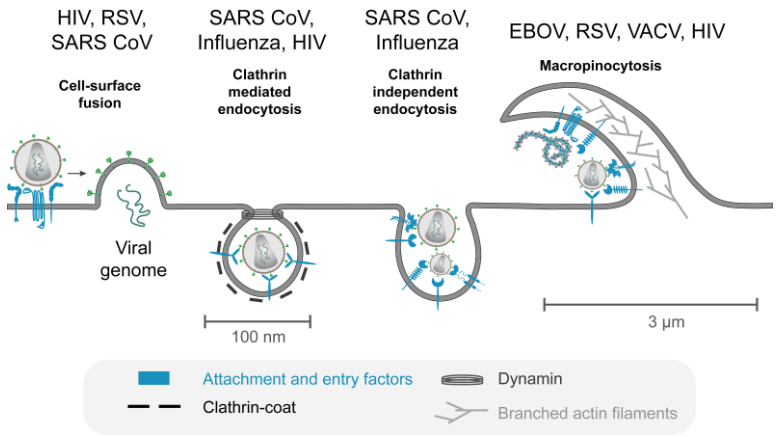

Figure 1.4: Schematic illustrating several common entry mechanisms utilized by enveloped viruses: After binding to receptors, some viruses can fuse their envelope with the host membrane on the cell surface. Most internalized viruses are delivered to the early endosome via vesicular (clathrin- or caveolin-coated vesicles) or tubular intermediates. Other viruses can be endocytosed by mechanisms that are independent of the coat protein clathrin. Larger viral particles (such as EBOV) require ingress pathways with increased cargo capacity and thus utilize mechanisms such as macropinocytosis, which is induced by actin-dependent cell extensions to envelop the virion.

In some cases, the fusion of enveloped viral with the host cellular membrane occurs at the host cell surface. For example, HIV fusion with the host cell membrane occurs after the attachment of envelope glycoproteins to cell surface receptors, catalyzing membrane fusion (*44*). Fusion events that takes place at the cell surface does not require a low pH, but do necessarily need a receptor (*45*). Co-receptors (one of multiple members of the chemokine receptor family) will also aid in determining the susceptibility or not of certain cell types. For instance, CD4 binding causes a conformational change in HIV glycoproteins (gp120/gp41), increasing proteolytic cleavage of the gp120 moiety, favoring glycoprotein binding to the co-receptor (*46*). Fusion arises from co-receptor attachment, likely as a result of the co-receptor's induction of glycoprotein dissociation, fusion peptide exposure, and refolding (*47*). In other cases, the fusion of membranes requires the virus to be taken into endocytic compartments, where the fusion process is initiated by the lower pH and protease content within maturing endocytic compartments.

Endocytic entry pathways offer several advantages for enveloped viruses (**Figure 1.4**). By virtue of their entry vesicles, these viruses can utilize actin- or microtubule-based transport to relocate within the cell after being internalized. This mechanism eliminates the need for the virus to supply accessory proteins. Moreover, initially these enveloped viruses manage to avoid detection by the immune system as initially there is no evidence of infection at the cell surface. Additionally, specific proteases present in trafficking vesicles, such as furin and cathepsins, can facilitate fusion of the enveloped viruses membrane with the endocytic membranes through proteolytic activation (*43*). Host cells possess several mechanisms to take in materials from their surroundings, such as

clathrin-mediated or independent endocytosis and micropinocytosis (**Figure 1.4**). These mechanisms enable the cells to engulf different types of enveloped viruses, which vary in size and shape. These entry vesicles can range from small clathrin-coated pits measuring around 100 nm through to larger macropinosomes, which can be as big as 10 μm (**Figure 1.4**). Finally, each pathway, initiated by different receptors, will determine the critical cell factors (such as actin and dynamin), which are essential for the formation, closure, and scission of primary entry vesicles from the membrane *(43, 48)*.

Once a virus has entered a host cell, the subsequent stages of the viral life-cycle are triggered, including uncoating, replication and assembly. Enveloped viruses hijack proteins and organelles within host cells to complete their replication process. Cellular components essential for viral gene expression and replication are frequently organized into a replication center, where the proteome and genome required to create virions are synthesized (*49*). Some viruses replicate in the cytosol, whereas others such as herpesviruses and influenza viruses is navigated to the nucleus for replication (*50*). These replicated proteins and nucleic acids eventually lead to the formation of new virions. The last stage of viral replication is the release of the new virions produced within the host cell to finish the life cycle (**Figure 1.3**). These daughter virions are then able to infect adjacent cells and repeat the replication cycle.

Ebola virus (EBOV)

Within the enveloped virus, Ebola virus (EBOV) is a negative-sense, single-stranded RNA virus from the filoviridae family. The EBOV leads to severe hemorrhagic fever in both humans and other primates, with mortality rates reaching up to 90% (*51*). The Ebola virus genus has been circulating in several African countries since Belgian virologists Groen and Piot first discovered the Sudan Ebolavirus species in 1976 (*52*). The most significant outbreak to date occurred between 2014 and 2016 in West Africa, and resulted in more than 2,000 fatalities (*53*). In February 2021, the Democratic Republic of the Congo declared the re-emergence of an Ebola epidemic, which has caused international concern and apprehension (*54*). Although in December 2019, a vaccine against EBOV was approved, at current, a drug for the treatment of ebolavirus disease is not available. Improving our understanding of EBOV infection mechanisms could provide new clues for developing prevention and treatment strategies.

The EBOV genome contains seven linearly arranged genes and is ~19 kb in length, encoding seven corresponding structural proteins (**Figure 1.5**). The viral genomic RNA is surrounded by a helical nucleocapsid protein (NP). Expression of the virion associated protein viral protein 30 (VP30), VP35 and RNA polymerase L, are required for the transcription and replication of the viral genomic RNA (*55, 56*). VP24 and VP40 are involved with viral assembly and budding to form the filamentous virions (*57*). A viral surface glycoprotein (GP) is embedded in the viral envelope and is required for virus binding to host cell receptors and cellular membrane fusion. In addition, it has recently been shown that the PS present in the viral envelope is also involved in viral binding to cell

receptors and necessary for the membrane fusion (*58*).

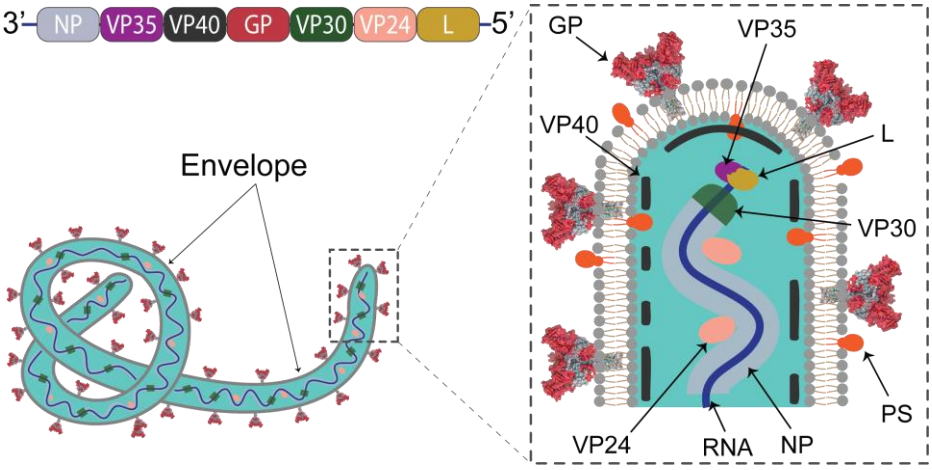

Figure 1.5: Schematic representation of mature EBOV virion. EBOV possesses a filamentous architecture and is approximately 80 nm in diameter and 1000 nm long. Nucleoprotein (NP) forms a protein-RNA complex by encasing the viral RNA genome. The virion-associated protein VP24, transcriptional activator VP30, polymerase cofactor VP35, and polymerase L interact with the viral RNA genome. The matrix protein VP40, which surrounds this complex, is primarily responsible for regulating virion shape and budding. These internal elements are enclosed in phosphatidylserine (PS)-containing lipid bilayer, which also contains trimers of the glycoprotein (GP) spike.

EBOV surface glycoprotein (GP) and phosphatidylserine (PS)

A trimeric protein consisting of 676 amino acids, EBOV GP contains an extracellular topological domain, a transmembrane helical domain, and a cytoplasmic domain (**Figure 1.6a**). The trimeric GP complexes consist of GP1 and GP2, which are two distinct subunits formed from the GP precursor cleaved by furin in the producer cell. GP1 is not directly anchored to the viral envelope, but instead forms a disulphide linked complex with GP2 at the virion surface (*59*).

In mature virions, GP1 is responsible for the binding to host cellular receptors, whereas GP2 is required for the fusion of virus and host membranes. The viral surface GP forms a cup shape, with the three GP1 subunits protruding outwards, bound together at the bottom by the three GP2 fusion subunits (*59*). During the membrane fusion process, GP1 is released from the GP1-GP2 complex. Subsequently, a significant conformational change occurs in GP2, transforming it from a metastable prefusion state to a more stable six-helix bundle. The stable post-fusion GP2 consists of a long and triple-stranded coiled coil, the three heptad repeat, and the outside shorter helices (*60*).

Each of GP1 and GP2 subunits have different subdomains. The head of GP1 is the receptor binding domain, which is decorated with a glycan cap with several N-linked glycosylation sites (*59, 61*). This glycan cap is surrounded by a flexible, heavily N- and O-glycosylated, mucin-like domain (*62*). The mucin-like domain is quite flexible and is involved in EBOV cell entry and immune evasion (*63*). The GP2 subunit contains an N-terminal peptide, an internal fusion loop, and two heptad repeats that flank a CX_6CC switch region (*59*). Many structures have been determined for filovirus GP in complex with antibodies, revealing a variety of antibody

epitopes that target different regions of the protein. These epitopes include the stalk of GP2, as well as the glycan cap, receptor-binding site, head, and mucin-like domain of GP1, revealing that an array of sites on GP can be targeted by antibodies in response to immunization or natural infection (*64-67*).

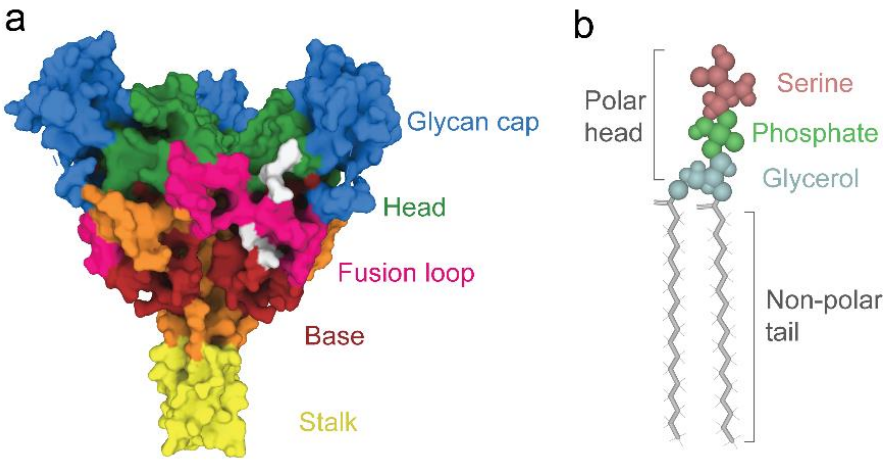

Figure 1.6: Overall structure of EBOV GP and PS. The crystal structure of EBOV GP reveals a three-lobed chalice-like structure. **a** The Glycan cap (blue) covers its top to shield the head domain (green), which mediates attachment to host cells. The stalk (yellow) connects the glycoprotein to the viral membrane proximal through a base subdomain in which the fusion loop (pink) is located on top. **b** Schematic of PS, showing components of the polar head, Serine (pink), Phosphate (green), Glycerol (grey), and non-polar tail, which consists of two fatty acids ester-linked to the first and second carbons of glycerol and serine phosphodiester-linked to the third carbon of glycerol.

Usually located in the inner layer of the cell membrane of healthy cells, PS is a glycerophospholipid, with a structure consisting of a polar head (including the phosphoserine group, a glycerol backbone, and serine) and a non-polar tail of two fatty acid chains (**Figure 1.6b**). Upon virus egress, PS is externalized onto the outer leaflet of the viral envelope EBOV virions *(68)*. As PS is a marker for apoptosis it is likely that EBOV utilizes apoptotic mimicry as a mechanism to facilitate its entry into scavenging and immune cells (*28*). Studies detailing the exact role of PS are needed, and may lead to the development of new broad-spectrum antivirals targeting the PS-dependent infection process.

EBOV attachment and entry mechanisms of GP- and PS-dependent

The first crucial stage in the effective infection of EBOV is the landing and attachment of free virions to the host cell surface. Two types of receptors have been well-documented to bind EBOV, C-type lectins (carbohydrate-binding receptors) and PS-specific receptors, which mediate virion attachment to the host cell surface (*69*). As noted previously, the glycan cap on EBOV GP is highly glycosylated with N- and O-glycans (*62*), the presence of these glycans favours EBOV entry, as they serves as a ligand for multiple C-type lectins including: lymph node sinusoidal endothelial cell C-type lectin (LSECTin) *(70),* human macrophage galactose- and acetylgalactosamine-specific C-type lectin (hMGL) (*71*), asialoglycoprotein receptor 1 (ASGPR1), dendritic cell-specific ICAM-3-grabbing non-integrin (DC-SIGN) *(72, 73)*, and liver/lymph node-specific ICAM-3 grabbing non-integrin (L-SIGN, also called DC-SIGNR) (*72, 73*). These C-type lectins are receptors that are expressed in a variety of cells and interact with specific carbohydrates. For instances, DC-SIGN is expressed on myeloid cells, while L-SIGN is

expressed on some endothelial cells, both bind to high mannose (*74*). LSECtin (which is expressed on liver and lymph node sinusoidal endothelial cells), ASGPR1 (which is expressed on hepatocytes), and hMGL (which is expressed on macrophages) bind to N-acetylglucosamine-β1, galactose, and N-acetylgalactosamine, respectively (*75*). It should be noted that other C-type lectins likely interact with the glycans of GP and thus play an important role facilitating EBOV infection, such as mannose-binding lectin (MBL) and ficolin-1 (*76, 77*).

Another group of receptors are those that bind PS, which predominantly belong to two major subfamilies: TYRO3-AXL-MERTK (TAM) receptors and T cell immunoglobulin mucin domain receptor (TIMs). TAM receptors were identified to increase EBOV infection (*78*). Interaction between TAMs and PS is bridged by a serum protein known as growth arrest-specific factor 6 (Gas6), and a second PS-binding serum protein (Protein S) (*79*). Both Gas6 and Protein S contain glutamic acid residues in their N-terminal domain which enable binding to PS. Additionally, they have a globulin-like structure in their C-terminal region that binds to the Ig-like domains of the TAM receptors (*80*). Two TIM family members (TIM-1 and TIM-4) have also been identified to facilitate for EBOV cell entry (*58, 81*). The immunoglobulin variable-like domains (IgV) of these TIMs have a conserved binding pocket specifically for PS (*82, 83*). This binding pocket enables a direct interaction with PS from the outer leaflet of the EBOV envelope membrane (*32*). Both TAMs and TIMs have been identified to increase EBOV infectivity, however, those interactions are poorly described from a thermodynamic point of view.

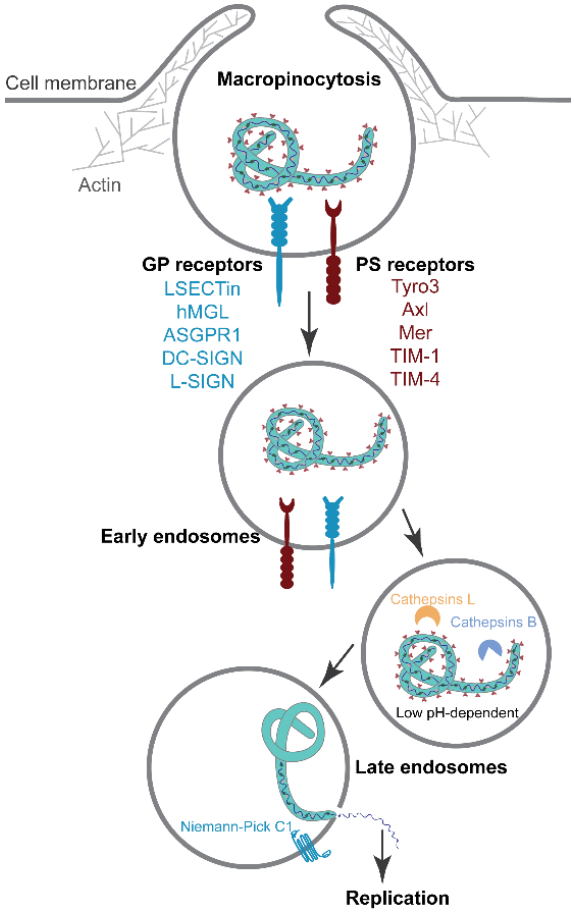

Figure 1.7: Schematic representation of EBOV host factors and entry. Following interaction with attachment factors, the virion is internalized by the macropinocytosis pathway. Inside the membrane-bound vesicle, GP is cleaved by cysteine proteases to activate its fusogenic potential. Cleaved GP is then able to interact with the specific NPC1 viral receptor triggering the fusion between the viral envelope and the endosomal/lysosomal membrane, leading to viral genome release followed by transcription and replication.

After binding to its target receptor, EBOV is internalized into macropinosomes and reach their intracellular destination through interacting with multiple host factors (*84*). EBOV are internalized through a macropinocytosis pathway (*85, 86*), which in contrast to other pathways, can handle cargo sizes up to the micron scale (*87*). Internalization is

initiated in an actin-dependent manner, wherein a protrusion extends from the cell membrane and then invaginates to create macropinosomes (*88*). This process leads to extracellular EBOV virions being engulfed into entry vesicles, which through endocytic processing develop into early endosomes and subsequently traffics to the late endosome or lysosome (*84*). The EBOV GP is then cleaved by cathepsins L and B in a low pH-dependent manner within the endosome to expose the receptor binding domain of 19 kDa (*85*). The exposed domain interacts with the late endosomal protein, Niemann-Pick C1 enabling the release of the EBOV genome into the cytoplasm and to start the virus replication (*87*) (**Figure 1.7**).

Since attachment of EBOV to the surface of host cells is the very first step in its life cycle (**Figure 1.7**), focusing on this stage is critical for defining EBOV biology and pathogenesis and for discovering vaccines and therapeutic treatments. Despite the great potential of preventing and inhibiting EBOV attachment through targeted virus-receptor interactions, and despite the numerous molecules that have shown beneficial effects, few such antiviral drugs have been approved and are effectively used against EBOV diseases (61, 64, 66, 90-92). Therefore, gaining new insights into the molecular details of viral attachment to cell surface receptors is critical to effectively advance the development of anti-EBOV strategies based on receptor-binding inhibitors.

Severe acute respiratory syndrome coronavirus 2 (SARS-Cov-2)

The coronavirus disease 2019 (COVID-19) pandemic, caused by the novel SARS coronavirus 2 (SARS-CoV-2), has spread rapidly across the globe since it the first reported in 2019. As of February 22, 2023, more than 757 million confirmed cases of COVID-19 have been reported worldwide, which have resulted in approximately 6.8 million deaths (*93*). This disease is mostly transmitted through airborne droplets containing infectious virions. The SARS-CoV-2 virions can survive inside the droplets for days under appropriate humidity and temperature (*94*). COVID-19 disease shows multiple characteristics, including fever, cough, sore throat, and headache. COVID-19 typically results in modest signs and symptoms, but infection can also lead to a more severe form of the disease particularly in those with pre-existing conditions or lowered immunity. To stop the pandemic COVID -19, many efforts have been made in recent years to better understand the molecular mechanism underlying the infection of SARS-CoV-2. However, the understanding of the molecular mechanism of SARS-CoV-2 infection is still incomplete.

In terms of phylogenetics, SARS-CoV-2 belongs the subgenus *Sarbecovirus* of *Betacoronavirus,* which are known to undergo zoonosis (*95*). This particular taxon has close genetic homology with its relatives, for instance bat-derived severe acute respiratory syndrome like coronaviruses, severe acute respiratory syndrome coronavirus (SARS-CoV), and Middle East respiratory syndrome coronavirus, share 88%, 79%, and 50% sequence identity with SARS-CoV-2 respectively (*96*). Despite slight variation at some amino acid residues in genome sequence, SARS-CoV-2 has a similar receptor-binding domain structure with SARS-CoV. SARS-CoV-2 also relies on angiotensin-converting enzyme 2 (ACE2)

which was originally identified in 2003 as the primary receptor for SARS-CoV to enter cells (*97, 98*).

As with other members of its genus, SARS-CoV-2 is an enveloped and positively sensed single-stranded RNA virus. The viral particles of SARS-CoV-2 are spherical virions with a diameter of approximately 80-120 nm (*99*). The SARS-CoV-2 RNA genome encodes four major structural proteins, including spike (S), envelope (E), membrane (M), and nucleocapsid (N) (**Figure 1.8a**). In addition, the viral proteome also contains approximately 16 nonstructural proteins and five to eight accessory proteins. To form virions, the M protein is responsible for the shape and assembly of the virus and leads to the formation of the mature viral envelope with the assistance of the E protein. The SARS-CoV-2 genomes are encapsulated by N proteins and combined with structural proteins. They are surrounded by a lipid envelope that contains a combination of the membrane (M), envelope (E), and spike (S) proteins, leading to the assembly of the complete virion. The S protein is a homotrimer forming a spike-like structure at the virion's surface and playing a key role in host cell binding. Surface glycoproteins of enveloped viruses, including EBOV and coronaviruses, are cleaved by enzymes of host cells after the infection. Unlike other coronaviruses, the SARS-CoV-2 S protein is cleaved into S1 and S2 subunits by proprotein convertases such as furin during their biosynthesis in the infected cells (*100*). It has been found that certain proportion of cleaved S2 subunit exists on the surface of native virus particles (*101*).

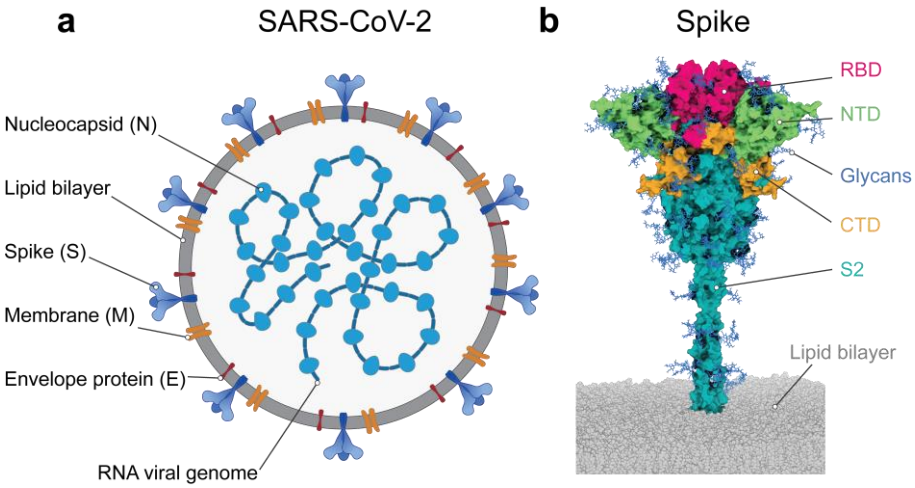

Figure 1.8: Schematic structure of SARS-CoV-2 and its trimeric spike protein. **a** The majority of the viral structure is made up of structural proteins such as spike (S), membrane (M), envelope (E), and nucleocapsid (N). The viral envelope, a lipid bilayer produced from the host cell membrane, contains the S, M, and E proteins. **b** The N protein interacts with the viral RNA in the virion's core. The architecture of SARS-CoV-2 S is highly glycosylated, comprising the S1 and S2 subunits. The S1 consists of the N-terminal domain (NTD), receptor-binding domain (RBD), and C-terminal domain (CTD). S2 is located on the viral membrane, containing fusion peptide (FP), heptad repeats 1 and 2 (HR1 and HR2), transmembrane domain (TM), and cytoplasmic tail (CT).

SARS-CoV-2 surface spike protein (S)

As previously mentioned, the GP of EBOV forms a heterodimer consisting of 676 residues connected by a disulfide bond between GP1 and GP2. In contrast, the spike protein (S) of the SARS-CoV-2 virus is a larger heterodimer comprising 1273 residues that are non-covalently linked between the S1 and S2 subunits. One of the distinctive features of the virus, SARS-CoV-2 S protein is a type I membrane protein anchored to the viral membrane by its transmembrane segment. Identified through use of x-ray crystallography and cryo-electron microscopy, various structural conformations of S protein have been observed. These

independently discovered structures are mostly in agreement with one another, allowing us to understand both the overall architecture and atomic structural details of S protein. In the prefusion conformation, the S protein forms a trimer, every monomer can be divided into two subunits (S1 and S2) (**Figure 1.8b**). S1 can be further divided into several subdomains, including the N-terminal domain (NTD), receptor-binding domain (RBD), and C-terminal domains (CTDs) (*102*). The wrapped prefusion S2 by S1 subunits consists of a central helical bundle with heptad repeat, transmembrane segment, and the cytoplasmic tail (*103*). Among the structures identified, the RBD can be found in an 'open' or 'closed' conformation corresponding to a receptor-accessible state and a receptor-inaccessible state respectively (*101, 104*). In the post-fusion state, conformational changes or receptor binding lead to S1 subunit dissociation from S2, while S2 undergoes a substantial refolding and rearrangement to form a stable six-helix bundle (*105*).

The NTD of the S1 subunit consists mainly of an antiparallel β-sandwich fold and a number of connecting flexible loops, decorated by glycans. It plays a functional role in SARS-CoV-2 entry, which facilitate the prefusion to post-fusion transition of the S protein and is identified by NTD-targeting neutralizing antibodies (*94, 106, 107*). Similarly, the CTDs of S1, connecting the NTD and the RBD on its two ends, are also formed by β-structures of segments and can be divided into two regions, CTD1 and CTD2. CTD1 is located beneath the RBD and can help it pivot outwards to reach the receptor-accessible state. CTD2 is linked to S2 subunits by a cleavage site consisting of a polybasic sequence that can be cleaved by furin and is a key element for the structural rearrangements of S protein required for membrane fusion (*108*).

The RBD of S protein consists of a core of the twisted antiparallel β-sheet connected by the α-helices and an extended loop (*109, 110*). In the closed conformation of prefusion S protein, RBD is constrained by the central helical bundle of S2 subunit, which dependent on the CTD1 of the same protomer and the NTD of the neighboring protomer, preventing its binding to the ACE2 receptor. To ensure receptor engagement, RBD is required for the transition from the closed to the upward conformation. Binding of the ACE2 receptor to an open RBD then leads to other RBD transition to an open conformation (*104*). Notably, the RBD is the major target for neutralizing antibodies after natural infection or vaccination. There are three major non-overlapping antigenic sites on the RBD: the directed neutralizing antibodies of RBD, the exposed surface of the RBD, and the buried side of the RBD (*111*). The high potency of these antibodies makes them promising therapeutic agents. Moreover, a recombinant human ACE2 was also shown to successfully prevent SARS-CoV-2 infection *in vitro* (*112*). Although the efficacy and safety profile of these antibodies and recombinant proteins still require further validation, they are potential inhibitors of viral entry and thus could potentially ameliorate the threat or severity of the COVID-19 disease.

Sructural analysis revealed that S2 subunits have both prefusion and post-fusion conformations. The prefusion conformation of the S2 subunit is stabilized by the formation of a stable three-stranded coiled-coil bundle surrounding the central helices. The fusion peptide, is tucked into a pocket formed by two neighboring S protomers and serves as an important functional unit on the S2 subunits as it is required for membrane fusion. The prefusion conformation undergoes a transition that can insert the fusion peptide FP into the target cell membrane,

subsequently an irreversible structural refolding and rearrangement occurs resulting in the post-fusion conformation (*113, 114*). The stability of the post-fusion conformation of S2 is significantly higher when compared to that of the prefusion state. It is important to note that post-fusion S2 is not only present after membrane fusion but is also widely spread across the surface of the mature virion (*101*). The post-fusion S2 also undergoes glycosylation modifications, which have the potential to play critical roles in viral infections and immune responses. (*114*).

SARS-CoV-2 attachment and fusion mechanisms of S-dependent

One of the essential tasks of the spike protein is to facilitate viral attachment to the target cell surface via its specific receptors. As the main receptor for SARS-CoV-2, ACE2 interacts with the S protein RBD in the very early stages of the infection process. (*115*). The interface between the RBD of the S protein and ACE2 forms interaction networks of multiple residues to result in a high binding affinity. As mentioned previously, the sequence and structure of the spikes of the SARS-CoV virus from 2002 and SARS-CoV-2 are very similar, although the RBD of SARS-CoV-2 S protein shows a 10 times higher affinity to ACE2 (*102*). This huge difference explains why SARS-CoV-2 spread more easily through the population than did the previous virus. Research has shown that SARS-CoV-2 enters the body primarily through the respiratory and gastrointestinal tracts, but can also infect cells of the kidneys, liver, heart, brain, and blood (*1116*). Due to the ability of SARS-CoV-2 to infect different organs, it is possible that other host receptors aid in viral spread *in vivo*. As such, several SARS-CoV-2 candidate receptors have been suggested (*117*), including heparan sulfate (*118*), sialic acid (*119*), Axl (*120*), NRP1 (*121*), and DC-SIGN/L-SIGN (*122*), which could act as an

alternative entry point or play cooperative functions to identified entry pathways. These host factors represent attractive targets for antiviral therapy as they are genetically more stable than viral targets.

Upon receptor engagement, the dissociation of S1 from S1-S2 complex, followed by major conformational changes in the S2 subunit, initiates virus-host cell membrane fusion (**Figure 1.9**). In addition, the S2′ site is also primed to fully expose the fusion peptide either by TMPRSS2 on the cell surface or by cathepsin L in endosomes. In both cases, the hydrophobic fusion peptide is exposed to insert into the target-cell membrane or endosomes. S2 subunit undergoes a significant conformational change, especially in the heptad repeat 1 region, propelling the fusion peptide forward into the target membrane, initiating membrane fusion (*105*). Finally, the formation of a fusion pore between viral and cellular membranes allows viral RNA to be released into the host cell cytoplasm for replication.

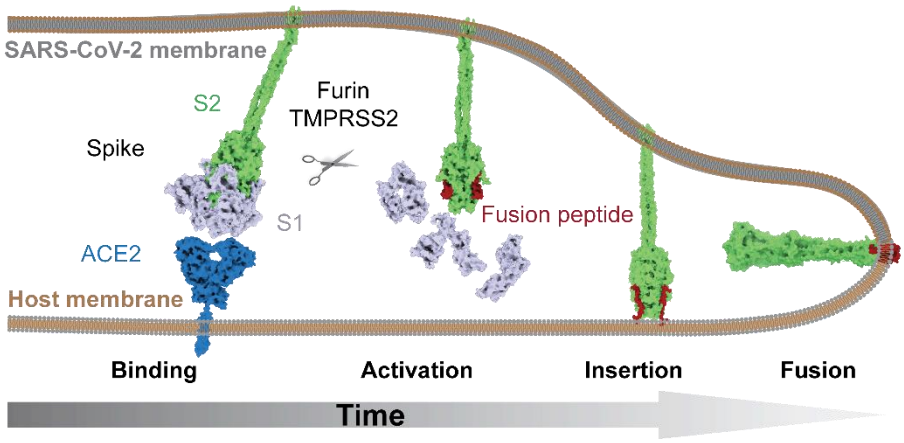

Figure 1.9: Model of interaction between SARS-CoV-2 and the host cell membrane. The interaction between hACE2 on the host cell membrane and SARS-CoV-2 prefusion S on the viral envelope triggers S1 dissociation. Subsequently, S2 unfolds and inserts into the host membrane. Refolding of S2 to a post-fusion state leads to membrane fusion.

As mentioned earlier, several vaccines and therapeutic agents against RBD of S proteins have been produced, and some of them have been approved and are successful against COVID-19 diseases (*99, 110, 112*). Unfortunately, RBD has a high number of mutations that lead to the different variants and the failure of vaccines and therapeutics (*123*). In contrast, all coronaviruses share a highly conserved domain and mechanism of membrane fusion (*124, 125*). However, there are currently no effective preventive or therapeutic treatments for fusion processes and domains. Therefore, understanding the mechanism of the fusion domain that mediates membrane fusion has the potential to be used for prophylaxis or therapy and to inform the development of vaccines that elicit broadly protective immunity.

In general, the infection process by an enveloped virus commences when the virus attaches itself to the host cell's surface. Subsequently, a complex series of events unfolds to complete the infection process, involving receptor binding and fusion with the cell membrane. Understanding the intricacies of these early steps in enveloped virus infection is a pivotal challenge in biology and a crucial step towards the development of vaccines and antiviral agents to combat diseases caused by enveloped viruses. To delve into the molecular mechanics of enveloped virus entry during the initial stages of infection, we utilized AFM to investigate the interactions between the glycoprotein of the EBOV and host cell receptors, as well as the interactions of the fusion peptide of SARS-CoV-2 with the host cell membrane.

1.2 Atomic force microscopy as a powerful technique for studying the viral entry mechanisms

Atomic force microscopy: setup and principle

For biologists, the ability to directly visualize the structure and function of macromolecules is a long-held dream, and microscopy has always been a crucial technique in this field. Optical microscopes have spatial resolution (typically from hundreds of nanometers to micrometers) and can track the location of tagged proteins. Although these methods have proven successful in capturing the dynamic behavior of various proteins, the resolution is limited. These techniques do not provide detailed information about the dynamics of protein interactions at the single-molecule level. This means that we still need to draw conclusions about the functioning and dynamics of protein molecules based on the recorded optical data.

In 1986, this status quo changed with the invention of atomic force microscopy (AFM) (*126*). This technique is characterized by its ability to visualize atoms on flat surfaces. Because AFM can work in fluids, pioneering scientists soon applied it to biological systems. These studies were mainly conducted in two directions: (i) acquiring high-resolution images of biological samples and (ii) exploring the functions of biomolecules. Regarding the first direction, Andreas Engel's laboratory obtained high-resolution images of several proteins, including bacteriorhodopsin embedded in a lipid membrane (*127, 128*) and a regular surface layer of proteins on bacterial cell envelopes (*129*). As part

of the second line of study, which focuses on the function of biomolecules, AFM imaging was performed to study dynamic processes such as the binding of antibodies to proteins (*130*), the infection of living cells by a virus (*131*), and many others (*132*).

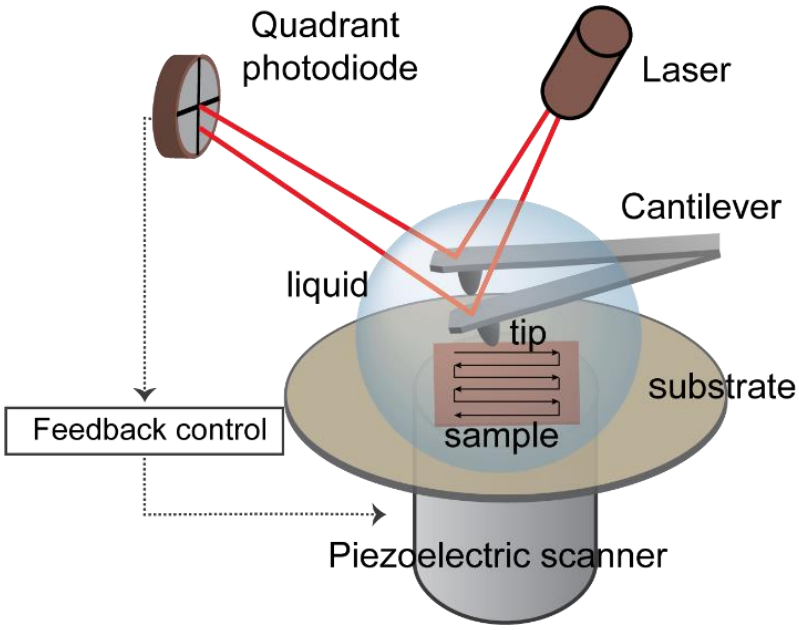

Figure 1.10: Schematic representation of the AFM. A conventional optical feedback AFM system works by scanning an AFM probe with a sharp AFM tip over a sample surface in a raster pattern. AFM tips are usually made of silicon or silicon nitride and are placed near the free end of a flexible AFM cantilever. The lateral and vertical position of the AFM probe relative to the surface is controlled by a piezoelectric ceramic scanner. The deflection of the AFM cantilever changes as the AFM tip passes over objects of different heights. A laser beam reflected from the back of the AFM cantilever and directed into a position-sensitive photodetector tracks this deflection. A feedback loop controls the vertical extent of the scanner to ensure a nearly constant deflection of the AFM cantilever and thus a constant contact force. The AFM tip coordinates acquired during the scan are extracted to obtain a three-dimensional topographic representation of the surface.

AFM uses a sharp nanoscale tip to detect minute forces from the sample surface based on the interaction between the tip and the sample surface. Due to the highly localized nature of the atomic force, nanoscale features can be resolved by raster scanning the tip across the surface while a feedback loop keeps the force constant (**Figure 1.10**). AFM is capable of imaging almost any type of surface by using various feedback signals to maintain the tip-sample interaction.

Distance feedback mode (also called contact mode) is the most direct AFM mode. In contact mode, the tip is brought in contact with the sample surface and the force between the tip and the sample is kept constant by the feedback loop to adjust the distance during scanning. The change in distance (Δz) of the cantilever deflection caused by the tip-sample contact can be used to measure the vertical contact force as $k_c \times \Delta z$, where k_c is the cantilever spring constant. The resolution of the image produced by AFM in contact mode depends on the applied force, which is determined by the cantilever spring constant. Since the tip is in contact with the surface during scanning, a significant shear force can be generated, resulting in damage to sample, especially for very soft biomolecules and living cells. To minimize this damage, it is advisable to use a soft cantilever when examining biological samples.

Since the invention of the AC mode (also called amplitude modulation mode or tapping mode), the contact mode is rarely used for biological samples in solution except for very low-height samples (*133*). In AC mode, the cantilever oscillates at (or near) its first resonant frequency. Therefore, the tip intermittently contacts the sample. The AC mode is further divided into amplitude modulation (AM), phase modulation (PM), and frequency modulation (FM) modes, each of which respectively uses

an amplitude change, a phase shift relative to the cantilever's excitation signal, and a resonant frequency shift for feedback control to keep these quantities constant (*134*). For AM-AFM and PM-AFM, the cantilever excitation frequency is usually set to the original peak frequency. The oscillatory response of the cantilever is modified by intermittent tip-sample contact. For biological samples, the phase delay caused by damping interactions is generally very small when tip-sample interactions are weak, resulting in a broad drive frequency. For FM-AFM in liquid, the cantilever is excited by a self-oscillating circuit so that the drive frequency is always set to the varying resonant frequency of the cantilever. To make the oscillation as large as possible, the cantilever tip should almost always be in the range of the repulsive force. Therefore, the recommended range for the cantilever vibration amplitude is typically 0.4 nm or less. Because of this limitation, FM-AFM is only suitable for samples with small surface roughness (*134*).

Of these noncontact methods, the AM method is most commonly used for imaging biological samples in solution because it is simple, stable (and causes little disturbance to the sample), and the amplitude of the cantilever oscillation is not limited. The amplitude of the oscillation can be reduced not only by the energy dissipative damping interaction, but also by the phase shift or delay. As a result, the amplitude signal is somewhat more sensitive to the tip-sample interaction than the phase shift and resonant frequency shift, although the sensitivity of these values varies depending on other parameters such as the amplitude of the free oscillation of the cantilever and the resonant frequency (*134*).

AFM-based high-resolution and/or high-speed imaging

In the resolution, AFM is determined by the properties of the atomic wavefunctions of the tip and sample. The vertical AFM resolution (also called sensitivity) is mainly limited by the thermal noise of the deflection detection system. For the optical lever system, the thermal noise of a free rectangular cantilever can be calculated by the equation $\Delta z = \sqrt{\frac{4k_BT}{3k}}$, where k_B is the Boltzmann constant, k is the spring constant of the cantilever, T is the absolute temperature. Most commercially available AFM instruments achieve a vertical resolution in 0.01 nm, which is not surpassed by other traditional surface analysis techniques.

The high lateral resolution of the AFM is closely related to its vertical resolution in sub-Å level (*126*). By analogy with light microscopy, the lateral resolution of AFM is defined as the minimum detectable distance between two sharp spikes of different heights (**Figure 1.11**). This minimum detectable distance (d) is related to the tip curvature radius of the tip (R) and the vertical resolution (Δz), assuming a small relative height (Δh) of the two peaks: $d = \sqrt{2R}\left(\sqrt{\Delta z} + \sqrt{\Delta z + \Delta h}\right)$. In this context, the sharpness of the tip is the key resolution-limiting factor (*135*). The resolution of AFM is determined by the geometry of the probe, which is different from optical microscopy. Because AFM tips have limited sharpness, the apparent width of a surface feature is greater than its actual width, as shown in illustration **Figure 1.11**. To accurately interpret the dimensions of the observed topography, tip convolution is a crucial factor to consider.

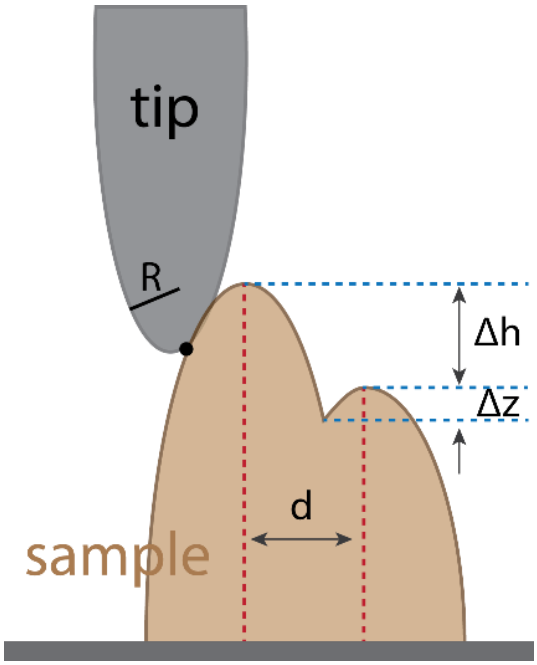

Figure 1.11: Schematic representation of AFM resolution. Two sample spikes of various heights are scanned by the tip of the radius of curvature *R*. The minimum lateral distance d resolvable by the tip depends on the measurable limit of the dimple *Δz* and the relative height *Δh* of the two spikes.

The exceptionally high resolution and signal-to-noise ratio of AFM have made it possible to determine the structure and functional state of numerous membrane and water-soluble proteins (*136, 137*). AFM has, for example, visualized the morphological dynamics of cells (*138*), and the growth of pathological amyloid fibrils (*139*), and provided insights into the functioning of pores in the outer bacterial membrane (*140*), nuclear pore complexes (*141*), ribonucleic acid (*142*) and lipid membranes (*143*). Other exciting examples were the observation of the infiltration of pathological toxins into membranes (*144*) and the supramolecular architecture of photosynthetic membranes that change in response to light (*145*). Thanks to these studies, static structural models could be

complemented by functional dynamics (*146*).

Achieving atomic resolution with AFM on biological samples remains a challenge, as this has only been accomplished for hard samples. The best resolution achieved on membrane proteins was ~ 1 nm in the vertical direction and ~ 0.1 nm in the lateral direction, which allowed the detection of sub-structural features of individual membrane proteins (*147*). The key factors limiting lateral resolution are the sharpness of the cantilever probe and the control of probe-sample interactions. The resulting topography is a convolution of the surface structure of the sample and the shape of the stylus, which physically follows the contours of the sample surface. Consequently, sharper tips with smaller radii can capture higher-resolution images. However, even a sharp tip can not produce a high-resolution image if the forces between the tip and the sample are not precisely controlled. More sensitive AFM devices and imaging modes that allow controlled application of forces with piconewton (pN) precision would improve the resolution of the image.

The relatively low temporal resolution of AFM imaging is a significant disadvantage compared to fluorescence microscopy. In recent years, tremendous technological advances have enabled an improvement in imaging speed, providing a means to study dynamic molecular processes. Among AFM components, the cantilever is the main limiting factor for AFM speed. To achieve high speed (HS-AFM), the response time of the cantilever must be shortened. It is also important to suppress the mechanical vibrations of the Z-scanner, which moves at much higher frequencies than X- and Y-scanners (*148, 149*). The current HS-AFM has a temporal resolution of less than 100 ms, a lateral resolution of 2–3 nm, and a vertical resolution of ~0.1 nm, with these measurements causing

little disturbance to sensitive biological samples. Despite this moderate resolution, HS-AFM remains the most important technique for simultaneously assessing the structure and dynamics of individual molecules during their functional activity. HS-AFM has been continuously and increasingly performed on a wide variety of protein molecules, demonstrating the innovative power of this novel microscopy to reveal details of dynamic molecular action that are inaccessible to other approaches (*150-152*).

AFM-based single molecule force spectroscopy and dynamic force spectroscopy

In addition to capturing topographic images, the AFM is capable of providing a wealth of nanomechanical data about the surface or sample under investigation. The instrument can be used to measure the force felt by the cantilever when the probe tip is brought close to a sample surface. The basic goal of AFM force spectroscopy is to acquire force-distance (FD) or force-time (FT) curves that measure the force applied to or felt by the AFM tip as a function of the distance between the tip and the sample surface or as a function of time. As the tip approaches the sample, touches it, applies pressure to it and then moves away, we can evaluate the physical properties of the sample, such as its elasticity and adhesion. The functionalized tip or cantilever with cells, biomolecules, or chemical groups allows us to measure the adhesion of single cells and specific interactions.

Among the rapidly expanding single-molecule techniques, AFM-based single-molecule force spectroscopy (SMFS) stands out as the best approach for studying intra- and inter-molecular forces with excellent spatial resolution and force sensitivity from 1 pN to 100 nN (*153*). Early versions of SMFS were designed to explore specific ligand-receptor combinations, such as the intensively studied streptavidin-biotin binding, complementary DNA strands, and antibody-antigen couplings, all grafted at low density onto the AFM tip and sample surface (*154*). The study to determine the specific binding forces between ligand-receptor pairs establishes the essential criteria that form the basis for subsequent SMFS studies. Nowadays, AFM-based SMFS is improved by a number of factors, including (i) revising the geometric shape, size, and materials of the tips,

(ii) reducing non-specific interactions between the tip and the sample, and (iii) using molecular linkers to tether the binding partners to give them sufficient flexibility so that their interaction is not disturbed by the linker while revealing the "fingerprint" of a specific force. Researchers are now able to study a variety of biological systems, including cell adhesion, single-cell sorting, cell mechanics, membrane assembly, protein (un)folding pathways, enzyme kinetics, ligand-receptor (un)binding and DNA mechanics (*155, 156*).

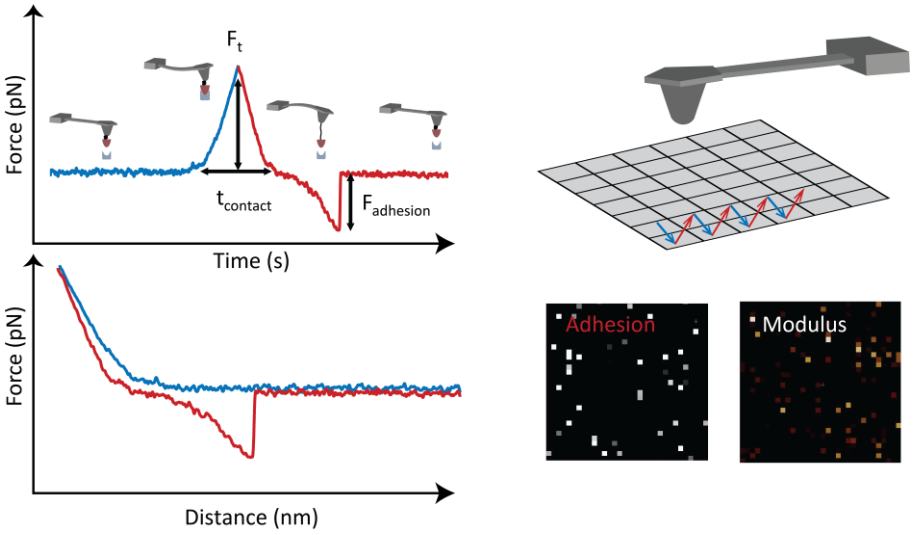

Figure 1.12: Schematic representation of single molecule force spectroscopy, force volume, and quantitative imaging. Generation of force-time curves (top) and force-distance curves (bottom) with SMFS. The Z-piezo brings the functionalized AFM tip from the initially away surface into contact with the sample until a certain force threshold is reached (approach curve in blue). During retraction (retraction curve in red), adhesion forces are observed at a distance that depends on the presence of a polymeric linker that tethers a molecular probe of interest to the AFM tip. FV records force curves for each pixel of the samples scanned by the tips, which can be analyzed to extract the adhesion force and elastic modulus of the samples.

AFM tips typically have radii of curvature in the range of 1-100 nm and can be positioned with nanoscale precision over the biosystem of interest to capture biomolecular interactions and biophysical properties of a specific structural or morphological region. AFM-based SMFS imaging can plot FD curves for each pixel of the resulting sample topography. Force-volume (FV)-AFM is another name for this AFM mode, which provides biophysical maps of the various physical properties of the sample. At FV-AFM, the tip deflection is modulated by a triangular waveform. A topographic image is combined with the acquisition of force-distance (FD) curves at each pixel of the image. Adhesion maps, modulus maps, etc. can be extracted from the resulting force-volume image (**Figure 1.12**). The method was demonstrated as a proof-of-concept by photographing a streptavidin pattern with a biotinylated tip and comparing topography and adhesion maps representing the separation of single streptavidin-biotin bonds (*157*). Similar research was conducted to map the distribution of a substrate covered with pure intracellular adhesion molecules using AFM tips functionalized with antibodies (*158*). FV-AFM has quickly become a preferred tool for the analysis of a wide range of biological materials due to its ability to map biophysical properties at high resolution (*159*).

A bond or complex is shifted from the equilibrium state to the non-equilibrium state when it is pulled apart under different mechanical loads using AFM-based SMFS. The force-load rate, denoted by LR, is the rate at which the external force acting on the molecule under study increases with time **(Figure 13a** and **b**). The plot of the forces required to rupture the bond over a wide range of force loading rates shows a transition from near-equilibrium mechanics to far-equilibrium mechanics, followed by an

increasing strength regime (*160*). This plot of the rupture force as a function of loading rate is termed dynamic force spectroscopy (DFS) and investigates the free energy landscape of dissociative and associative bonding, which is normally inaccessible in bulk assays. To assess the stochastic process of bond dissociation and to extract the kinetic and thermodynamic properties of binding from AFM-based SMFS measurements out-of-equilibrium and near-equilibrium, a variety of widely used theoretical frameworks of biophysical models exist (*160-162*).

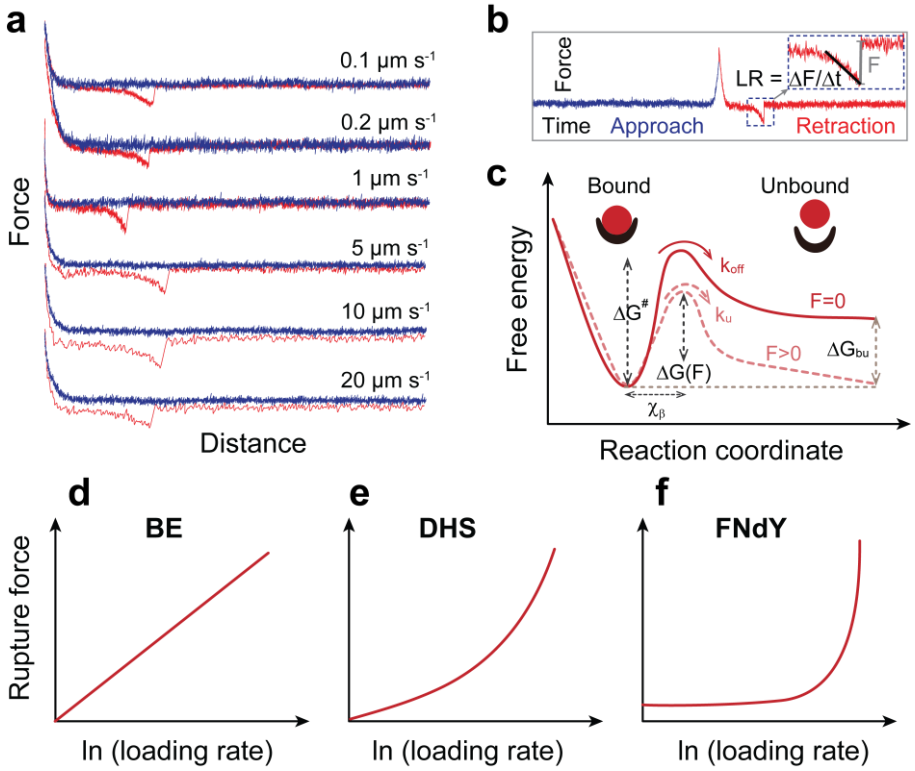

Figure 1.13: Extraction of kinetic and thermodynamic properties of specific biomolecular interactions from dynamic force spectroscopy. **a, b** Representative force-distance curves were plotted at different retraction velocities (from 0.1 to 20 µm s^{-1}) on the model surface and showed specific adhesion events. Force- time curve where the slope of the curve extracted just before the unbinding event is determined to extract the loading rate (LR=ΔF/Δt). **c** The interaction forces of a (bio)molecular bond over a wide range of loading rates allow the parameters describing the binding free-energy landscape to be extracted. These parameters include the binding free-energy difference ΔG_{bu} between the bound state and the unbound state, $\Delta G^{\#}$ the reaction barrier of the transition state, the distance x_β separating the bound from the transition state, and the transition rates k_{on} and k_{off}. **d, e, f** There are several biophysical models for interpreting the DFS data. Based on various hypotheses discussed in the text, the resulting theoretical relationships between force versus loading rate are presented schematically.

Noncovalent bonds have limited lifetimes and dissociate under nearly any amount of force when pulled on for a long enough time. If the dissociation durations of the noncovalent bonds in complexes increase

strictly exponentially with the applied force, then those bonds are said to be "ideal bonds". An ideal bond is represented by a bound state that is separated from the unbound state by a single energy barrier positioned at a fixed distance x_β. For an ideal bond, the transition between bound and unbound states exhibits first-order kinetics in their on-rate (k_{on}) and off-rate (k_{off}) rates (**Figure 1.13c**). The free-energy differential ΔG_{bu} between the bound and unbound states is commonly used to describe the thermodynamic bond strength. The height of the crossing entry barrier (ΔG_b) and exit barrier ($\Delta G^\#$), in relation to the unbound state, respectively, affects the kinetic on and off rates in an exponential manner. The binding free energy ΔG_{bu} is equal to the difference between the free energy barriers $\Delta G^\#$-ΔG_b, and the dissociation constant at equilibrium is represented by their ratio k_{off}/k_{on}.

According to physics, the strength of an isolated bond is proportional to the force required to separate the two binding partners. The analogous quantity for a macromolecule in solution is the gradient of free-energy in the direction of the pulling force. If all molecular motions and the cantilever reaction are fast compared to the motion in this direction, then the molecular partners should separate "spontaneously" after the externally applied force exceeds the steepest free energy gradient (*163*). From a purely mechanical perspective, it appears that the strength of bonds is not affected by the height of the energy barrier or other features of the energy landscape, except for the maximum gradient. This suggests that there may be a hidden aspect of the energy landscape that does not affect bond strength (*161*). In fact, when a force is applied to a bond of complex, a mechanical potential is added that tilts the free energy landscape and reduces the free-energy barrier to dissociation,

accelerating the process of bond dissociation. Bonds dissociate orders of magnitude faster when pulled by forces many times the thermal force ($f_\beta = k_B T / x_\beta$), i.e. the force exerted on the bond due to thermal fluctuations.

To explain how an external force pulling on a bond lowers the activation free energy barrier toward dissociation, Bell derived a theoretical model from Kramers' analytical reaction rate theory. This model recovers the Arrhenius dependence of the dissociation rate on the height of the free-energy barrier ($k_{off} \propto \exp(-\Delta G / k_B T)$). It bases on an assumption that the activation energy is large compared to the thermal energy scale, $\Delta G \gg k_B T$. The presence of an external pulling force F along the reaction coordinate "tilts" the internal binding potential and shortens the lifetime of the bond (*160, 164*). According to one assumption of the Bell model (**Figure 1.13d**), the separation of the bound state from the transition state along the reaction coordinate, x_β, must remain constant under the influence of the external force and the externally applied force is assumed to be constant in time. The force-dependent unbinding rate is described as:

$$k_{off}(F) = k_{off}(0) \exp\left(\frac{G_0 - F x_\beta}{k_B T}\right) \quad (1)$$

Where the k_{off}(F) is the off-rate of bonds under a force, $k_{off}(0)$ is the off-rate of bonds at equilibrium, G_0 is the energy of the bond at equilibrium, k_B is the Boltzmann constant), and T is the temperature.

Evans and Ritchie, starting from the Bell model, looked at the AFM investigations using cantilevers to break molecular interactions in a way similar Hooke's stretching. As the cantilevers retract, they exert a pressure that increase proportionally to the distance, leading to a general explanation for the distribution of rupture forces observed in SMFS (*163*).

The most likely rupture force F in the thermally activated regime scales linearly with the logarithm of the loading rate as predicted by the Bell-Evans model (BE) for a single dominant barrier to rupture as:

$$F^*(LR) = f_\beta \ln\left(\frac{LR}{f_\beta k_{off(o)}}\right); f_\beta = \frac{k_B T}{x_\beta} \quad (2)$$

The dependence $F^* \approx ln\ LR$ can account for nonlinear strain of elastic force transducers, such as polymeric linkers (*165*). The BE model has been widely used to explain the kinetics of various molecule bonds (*166-168*). Based on the BE model, Williams and Evans developed the predictive Williams-Evans (WE) model, which depicts multivalent interactions as uncorrelated bonds loaded in parallel (*169*). These multivalent interactions can be obtained from the predictive model as follows:

$$LR = k_{off}\left(\frac{k_B T}{x_\beta}\right)\left[\sum_{i=1}^{N} \frac{1}{i^2} \exp\left(\frac{\mathrm{F} x_\beta}{i k_B T}\right)\right]^{-1} \quad (3)$$

However, the BE model has some limitations, and as the experiments became more dynamic, deviations from the expected behaviour were noted. At high forces, when the transition barrier and the well must necessarily converge until they finally merge at a critical force when the barrier potential evaporates, the assumption of a force-independent x_β is not always valid.

Dudko, Hummer, and Szabo (DHS) revisited the assumption in the BE model that the distance to the transition state, x_β, does not depend on the externally applied force (**Figure 1.13e**). The DHS model implies that the free-energy potential well and the barrier eventually merge at a critical force when the barrier to rupture disappears, focusing on an external force that scales up linearly in time (*170*). This model incorporates the BE model as a limiting case, but predicts that, in general, both the logarithm

of the lifetime at constant force and the average rupture force are nonlinear functions of the force and the logarithm of LR, respectively. The DHS formalism adds a parameter to the BE model that enables a smooth interpolation between different potential shapes, namely the apparent free energy of activation ΔG^*. The DHS model has been validated as a simple method for determining the force-dependent lifetimes $\tau(F)$ from rupture-force histograms collected at different pulling speeds:

$$\tau(F) = \tau_0 \left(1 - \left(\frac{aFx_\beta}{\Delta G^*}\right)\right)^{1-\frac{1}{a}} e^{-\beta \Delta G^* [1-(1-(aFx_\beta/\Delta G^*))^{\frac{1}{a}}]} \quad (4)$$

The scaling factor a specifies the nature of the underlying free-energy profile (*171*): a = 1/2 corresponds to a cusp-shaped potential, while a = 2/3 corresponds to a linear-cubic binding potential. The BE expression is recovered for a = 1. The advantage of the DHS model is that it largely eliminates the need to make model-dependent assumptions about the functional form of $\tau(F)$.

According to the DHS model, it is possible to include the molecular linker in the calculation of LR (*170*). The equation $LR = k_c v$ can be used to calculate the loading rate at which a rupture event occurs. LR represents the loading rate in newtons per second (N/s), k_c is the cantilever spring constant in newtons per meter (N/m), and v is the retraction velocity in meters per second (m/s). The loading rate for two molecules connected by a linker, and following the dynamics of a worm-like chain (WLC) can be accurately modelled with the following equation:

$$LR = v \left(\frac{1}{k_c} + \frac{2\beta l_c l_p (1+\beta F l_p)}{3+5\beta F l_p + 8(\beta F l_p)^{5/2}}\right)^{-1} \quad (5)$$

In this equation, the retraction velocity is denoted by v, the contour length by l_c, β as $k_B T^{-1}$, and l_p as the persistence length of the system containing the linker or peptide. The first term in the brackets represents

the contribution of the loading rate of the cantilever, while the second term represents the contribution of the loading rate of the molecular linker. The advantage is that the DHS model absorbs the influence of flexible polymeric linkers in a force-dependent loading rate:

$$\frac{v}{LR} = \frac{1}{k_c} + \frac{dl(F)}{dF} \tag{6}$$

where v is the retraction velocity, k_c is the spring constant of the cantilever, and $l(F)$ is the force-dependent extension of the linker (*172*). The bond lifetime, τ(F), is approximated by the following equation:

$$\tau(F) \cong \frac{\left[\frac{\pi}{2}(\langle F^2\rangle - \langle F\rangle^2)\right]^{1/2}}{LR} \tag{7}$$

Where $\langle F^2\rangle$ is the mean squared rupture force at a given loading rate LR.

The BE and DHS models are extensively used to extract kinetic information from SMFS experiments, while the estimation of thermodynamic parameters is still a challenge. A theoretical foundation for estimating thermodynamic parameters is provided by the fluctuation theorems, which include the Jarzynski equation and its generalization, and the Crooks fluctuation theorem (*173-176*). This theory has shown how to estimate the difference in free-energy between the bound and unbound states from an irreversible non-equilibrium process to bridge the gap between statistical mechanics equilibrium and nonequilibrium.

A Friddle-Noy-de Yoreo (FNdY) model (**Figure 1.13f**) predicts that the DFS representation of a complex bond attached to a force transducer consists of two primary regimes, a near-equilibrium regime of the bond-transducer system characterized by an equilibrium force F_{eq} and a kinetic regime characterized by a fast rupture of a bond in non-equilibrium (*162*). According to the FNdY model, the transition rates of rebinding and

unbinding intersect at F_{eq}:

$$F_{eq} = \sqrt{2k_{eff}\Delta G_{bu}} \quad (8)$$

$$k_{eff} = \frac{k_c k_{linker}}{k_c + k_{linker}} \quad (9)$$

The mean rupture force is defined as:

$$< F > = F_{eq} + f_\beta \ln\left(1 + e^{-\gamma} R\left(F_{eq}\right)\right) \quad (10)$$

$$R\left(F_{eq}\right) = \frac{r}{k_{off}(F_{eq}) f_\beta} \quad (11)$$

Where $k_{off}(F_{eq})$ is the unbinding rate scaled by the Boltzmann weighted energy of a spring extending between the location of the barrier and the relative displacement of the spring minimum under F_{eq}, k_{eff} is the effective spring constant of the transducer, ΔG_{bu} is the equilibrium free energy, γ is Euler's constant. The FNdY model has been extensively used in recent FD-based AFM studies that map (bio)chemical information and where nonlinear DFS plots have been obtained (*177-179*).

The extraction of kinetic on-rate coefficients from force spectroscopy experiments is achieved by varying the contact times. the binding frequencies (*BF*) are determined for different contact times (*t*, the time the tip is in contact with the surface) (*180-183*). With increasing contact time, the interaction time (τ) also increases. The relationship between τ and BF is described by the following equation:

$$BF = A\left[1 - \exp\left(-\frac{(t - t_0)}{\tau}\right)\right] \quad (12)$$

To relate measurements obtained at the single molecule level to bulk measurements, k_{on} must be converted to a concentration dependent on-rate with units of $M^{-1}s^{-1}$. The k_{on} assumes that the interaction follows pseudo-first-order kinetics:

$$k_{on} = \left(c_{eff}\tau\right)^{-1} = \frac{\frac{1}{2}*4\pi r_{eff}^3*N_A}{3n_b\tau} \quad (13)$$

Where N_A is the Avogadro constant =6.023×10^{23}/mol, n_b is the number of binding partners (typically 1) within a free volume accessible to the molecule tethered to the tip, r_{eff} is the radius of the sphere. The dissociation constant for the binding reaction is then $K_D = k_{off}/k_{on}$.

AFM-based force distance curve and multiparametric imaging

For the dynamic AFM technique, there are two fundamental disadvantages of imaging in the tapping mode modulated by amplitude, phase or frequency. First, it is difficult to control the normal force acting on the sample surface. Second, imaging in tapping mode is limited to measuring the amplitude and phase shift, which depends on a large number of variables such as elasticity, viscosity, adhesion, and surface charge. There is no straightforward way to separate the influences of four or more variables with only two measurable quantities. To overcome these inherent problems, the force-distance (FD) curve-based AFM mode was introduced (also called the Peak Force tapping or off-resonance tapping mode) (*184*). Peak Force tapping mode modifies the Z-piezo in a sinusoidal low-frequency oscillation mode at ≤ 4 kHz with a wide range of peak force amplitude. The imaging feedback signal is then the highest interaction force of each of these force curves. As the system scans the tip across the sample, the system feedback loop maintains the instantaneous peak force at a constant value by adjusting the extent of Z piezo. Unlike the tapping mode, where the feedback loop keeps the oscillation amplitude of the cantilever vibration constant, Peak Force tapping controls the maximum force (Peak Force) on the tip. This minimizes the contact force between the tips and the sample at the same time that protects the sample from damage.

As previously stated, FV-AFM has limitations, such as very large forces used in topographic imaging, long acquisition (15-90 min) and low lateral resolution (>20-30 nm). Furthermore, due to discontinuities at the turning point of the cantilever between the approach and retraction segments, artifacts can occur when the force curves are acquired at high

speed. These limitations were removed by the FD-based AFM mode, which introduced a sinusoidal waveform as an alternative to the triangular waveform characteristic of FV-AFM. FD-based AFM records hundreds of thousands of FD curves per topography to map mechanical properties and interactions. Commercially available AFMs take tens of minutes to record this amount of data. Therefore, fast measurements are desirable to reduce image acquisition time and enable mapping of dynamic biological processes. Moreover, FD-based AFM mode has evolved into a nanoscopic tool that enables imaging of biological systems and simultaneous mapping of their numerous features at the nanoscale or sub-nanometer scale (*185-189*). The tip of an oscillating cantilever is approached and retracted from the sample. The path of a laser reflected from the cantilever to a position-sensitive detector changes as the tip interacts with the sample surface and is deflected by approach and retraction. An oscillating tip is raster-scanned over the surface sample as it performs the single approach and retract motion, recording FD curve for each pixel. The curves are then analyzed to obtain the mechanical properties of the sample (adhesion, modulus, deformation, and dissipation) and the information is sent to one of the image data channels while imaging continues at the usual imaging speed (**Figure 1.14**).

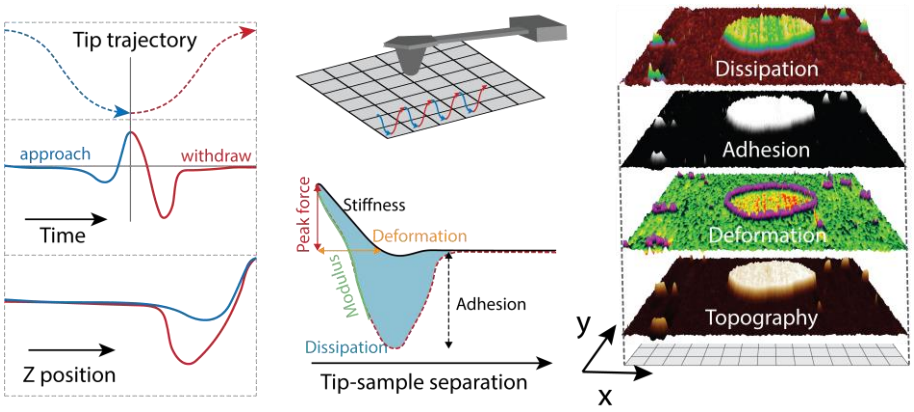

Figure 1.14: Force curves and information from FD-based AFM. Plotting force and piezo Z position as a function of time, including jump-to-contact, peak force, and adhesion. In a conventional force curve, the time variable is eliminated and the force is plotted against Z piezo position. Pixel by pixel, the AFM tip is approached (blue curve) towards the sample and retracted from it (red curve). For fitting purposes, it is more useful to plot the force against the separation, where the separation is calculated from the Z piezo position and the deflection of the cantilever. The parameters extracted from the individual force curves can be displayed as in the forms of maps, e.g. the topography of the sample (height image) contoured at a certain imaging force, the adhesion force, the deformation of the sample, and the work of dissipation.

Functionalization of the AFM tip with chemical groups, ligands, receptors or viruses allows the detection of specific interactions with their interaction pairs. Furthermore, this technique allows the simultaneous mapping of these interactions onto the topography of the sample. Examples include the mapping of chemical groups, glycans, or proteins on the surfaces of bacterial and mammalian cells (*190, 191*), the electrostatic properties of membranes (*192*), membrane proteins (*193, 194*) and the interactions between ligands and human G protein-coupled receptors (*178, 187, 189*). It has also been shown that two ligands can bind to the same receptor and that larger protein complexes can image ligand binding events with great precision (2-5 nm) (*195-197*). In

conjunction with a new theoretical model, the approach has been extensively used to image biomolecules and quantify the biophysics of these samples (*159*).

In complex biological systems, AFM suffers from the difficulty of identifying the detailed morphological and structural information in the image. Although recognizing imaging can identify and localize one or a few components (*195-198*), the complexity of, for example, a cell surface with its thousands of different biomolecules (e.g. sugars, lipids, membrane proteins, associated water-soluble proteins) is extremely high. This situation is further complicated by the fact that biomolecules dynamically assemble and disassemble into macromolecular complexes depending on the functional state of the cell. Therefore, it is difficult to correlate the physical information observed by AFM with cell state, morphology, and compartments. Combining FD-based AFM with optical microscopy (e.g. super-resolution optical microscopy and confocal microscopy) is an interesting way to overcome this problem (*179, 199, 200*). Details of the structures and properties as well as their specific composition in molecules or in the membrane can be addressed by AFM-based imaging. Fluorescence microscopy is used to image and map the correlated large compartments and structures and to monitor and localize processes in the cell.

As a proof-of-concept, this advanced approach was used to map the first binding steps of pseudotyped rabies viruses to MDCK cells engineered to express viral receptors to facilitate virus binding and entry (*179*). The combination of FD-based AFM with confocal microscopy allows the simultaneous imaging of cell surfaces expressing fluorescently labelled viral receptors and topographic mapping of their binding to

single viruses at high-resolution (<50 nm). The confocal microscopy images, AFM topography, and virus adhesion maps showed that rabies viruses only bind only to cell surfaces expressing the fluorescently labeled receptor, while they cannot bind to adjacent cells lacking the receptor. Furthermore, a theoretical framework was also established to extract the mechanical, kinetic, and thermodynamic parameters that govern the complex interactions of virus with cell surface receptors. This approach contours the free-energy landscape of a virus binding to cell surface receptors in living systems and provides mechanistic insights into how viruses initiate infection *via* successive binding events that enhance their binding to the host cells.

The method is very versatile and is currently used to map the interaction of different types of viruses, such as herpesviruses (*167, 201*), reovirus (*166, 202, 203*), SARS-CoV-2 (*119, 122, 181, 182*), and Rotavirus (*183*). In one such case, the S1 subunit of SARS-CoV-2 was covalently connected to the AFM tip *via* PEG linkers to map its binding to living cells *in situ* (**Figure 1.15**). According to the confocal microscopy images, AFM topography, and virus binding maps, the S1 subunit of SARS-CoV-2 could only bind to cell surfaces expressing the fluorescently labeled receptor, while it could not bind to adjacent cells without the receptor (**Figure 1.15**). Similarly, this approach was utilized to study the purple membrane adsorbed on mica (*199*). The individual purple membrane patches were identified and localized by the confocal fluorescence microscopy. High-resolution AFM was used to scan the topography of the purple membrane at sub-nanometer resolution. Finally, the folding of the membrane protein and the interaction forces that stabilize the protein were characterized.

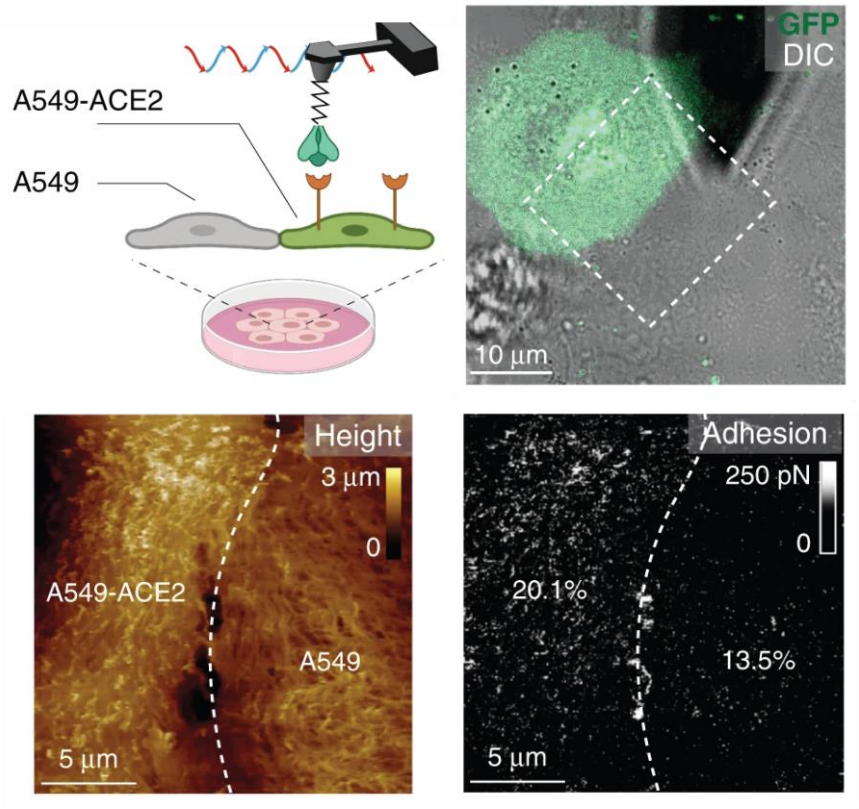

Figure 1.15: Principle of combining confocal microscopy and FD-based AFM to detect the binding of the molecule of interest (such as biomolecules and viruses) to animal cells. The wild-type cell and the cell (green) expressing receptors were mixed cultures scanned using the functionalized AFM tip with the molecule of interest. The image of the overlapping fluorescence channel with differential interference contrast (DIC) was obtained by confocal microscopy. The confocal image was used to control the AFM scan area. The FD-based AFM height image and the adhesion channel of the scan area of interest were acquired in the dashed square in the confocal image. The used images are adapted from ref (*182*).

AFM-based SMFS on force-clamp and height-clamp mode

Another broad application of the AFM is force sensor functions that can monitor and control the biological processes of molecules, viruses, and cells. The AFM system can drive the oscillation of a cantilever at different frequencies, making this device a sensing platform with simple stress and frequency detection. The shift in resonance frequency correlated with the quality of the substances bound on the surface of the cantilever. The sensitivity of the method was sufficient to detect single cell binding and antigen–antibody interactions (*204, 205*). More specifically, the microcantilever was used to detect the tiny change in cellular volume and mass during the cell cycle for milliseconds (*206, 207*).

The force-clamp mode controls the force applied to a sample through a feedback mechanism that maintains the applied force constant and quickly corrects the distance between the sample and the AFM tip. The force feedback, which is based on a proportional, integral, and differential amplifier, is directly linked to the timing response of the feedback and the piezo. The frequency response of the current amplifiers is currently in the sub-millisecond range, which means that the change of cantilever position is recorded with a high temporal resolution. Conversely, by controlling the Z-piezo of the AFM (height-clamp mode), the system can precisely manipulate the tip position with sub-nanometer precision (<1 nm). In height-clamp mode, force-time curves are collected by recording the force over time (**Figure 1.16**).

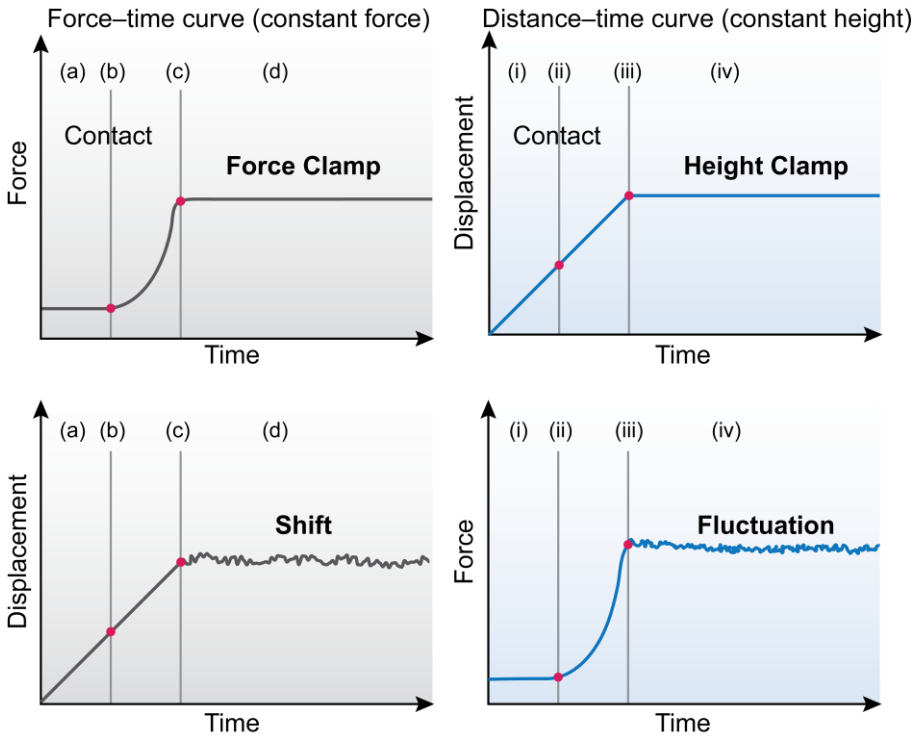

Figure 1.16: Schematic representation of the AFM-based force and height clamps-. Constant force: the AFM tip is brought towards the sample while the cantilever is held at a constant deflection (force). The deflection of the cantilever measures the position response of the samples. Constant height: the AFM tip is placed on the sample and then held at a fixed height. The force measured by the cantilever measures the force response of the samples over time.

Force and height clamp modes are currently used to solve fundamental problems in biology such as viral infection. The invasion process of a single human enterovirus 71 and Singapore Grouper iridovirus was monitored using force and height-clamp mode (*208, 209*). The dynamic process and mechanisms of virus invagination into cell were demonstrated by controlling the position of the virus on the cell surface. As the depth of engulfment increases, the density of binding energy also increases, suggesting that additional binding interactions between viral ligands and receptors gradually take place to provide sufficient energy for

viral invagination. The techniques offer the potential to study the entry of virus, rod-shaped nanostructures, and nano-drugs entry into living cells and allow direct investigation of the entry mechanism and kinetics (*86, 210-212*).

An extensive application of force and height clamp modes is the unfolding and refolding of proteins. The differential mechanical stability of the I27 and I28 domains of the human cardiac titin protein was demonstrated using force-clamp mode at the single-molecule level (*213*). This experiment inspired researchers to characterize the structural stability and unfolding, misfolding, and refolding pathways of various proteins. Such force-clamp assays, make accessible the end-to-end length of the small protein ubiquitin during its folding reaction (*214*), the pathways of protein unfolding and refolding, the enzymatic catalysis, the effects of osmolytes and chaperones on protein stability and folding (*215*), the kinetics and the length of unfolding of the small protein ubiquitin (*216-218*), and the mechanical unfolding of cold shock protein B (*219*). Most importantly, this technique allows independent measurements of the formation of the disulfide and protein folding (*220, 221*) and shows how non-native disulfides formed early in the folding pathway can trigger misfolding. In contrast, a protein disulfide isomerase domain favors native disulfides by catalyzing oxidation at the late stage of the folding pathways. This general mechanism explains how protein disulfide isomerase catalyzes oxidative folding in a variety of structurally unrelated substrates. In addition, the AFM-based height clamp mode was used to investigate how an insertase introduces the polypeptide into the membrane (*222*). This shows that the insertase binds the polypeptide in two steps. Subsequently, the hydrophilic groove of the insertase

transiently interacts with the polypeptide to introduce it into the membrane.

1.3 References

1. E. J. Lefkowitz *et al.*, Virus taxonomy: the database of the International Committee on Taxonomy of Viruses (ICTV). *Nucleic Acids Research* **46**, D708-D717 (2017).
2. M. Silasi *et al.*, Viral Infections During Pregnancy. *Am. J. Reprod. Immunol.* **73**, 199-213 (2015).
3. M. Asif *et al.*, Viral outbreaks: A real threat to the world. *Advancements in Life Sciences* **8**, 08-19 (2020).
4. N. Philippe *et al.*, Pandoraviruses: Amoeba Viruses with Genomes Up to 2.5 Mb Reaching That of Parasitic Eukaryotes. *Science* **341**, 281-286 (2013).
5. H. V. Chaudhari, M. M. Inamdar, K. Kondabagil, Scaling relation between genome length and particle size of viruses provides insights into viral life history. *iScience* **24**, 102452 (2021).
6. J. Cui, T. E. Schlub, E. C. Holmes, An Allometric Relationship between the Genome Length and Virion Volume of Viruses. *Journal of Virology* **88**, 6403-6410 (2014).
7. Z. Dogic, Filamentous Phages As a Model System in Soft Matter Physics. *Frontiers in Microbiology* **7**, (2016).
8. R. J. Bingham, R. Twarock, C. P. Mata, P. G. Stockley, in *Encyclopedia of Virology,* D. H. Bamford, M. Zuckerman, Eds. (Academic Press, Oxford, 2021), pp. 488-494.
9. P. Roingeard, P.-I. Raynal, S. Eymieux, E. Blanchard, Virus detection by transmission electron microscopy: Still useful for diagnosis and a plus for biosafety. *Reviews in Medical Virology* **29**, e2019 (2019).
10. J. Louten, in *Essential Human Virology,* J. Louten, Ed. (Academic Press, Boston, 2016), pp. 19-29.
11. P. T. Ivanova *et al.*, Lipid Composition of the Viral Envelope of Three Strains of Influenza Virus—Not All Viruses Are Created Equal. *ACS Infectious Diseases* **1**, 435-442 (2015).
12. M. S. Maginnis, Virus–Receptor Interactions: The Key to Cellular Invasion. Journal of Molecular Biology 430, 2590-2611 (2018).
13. J. E. Stencel-Baerenwald, K. Reiss, D. M. Reiter, T. Stehle, T. S. Dermody, The sweet spot: defining virus–sialic acid interactions. Nature Reviews Microbiology 12, 739-749 (2014).
14. Y. Yamauchi, A. Helenius, Virus entry at a glance. Journal of Cell Science 126, 1289-1295 (2013).
15. M. T. Shieh, D. WuDunn, R. I. Montgomery, J. D. Esko, P. G. Spear, Cell surface receptors for herpes simplex virus are heparan sulfate proteoglycans. Journal of Cell Biology 116, 1273-1281 (1992).

16. D. Shukla et al., A novel role for 3-O-sulfated heparan sulfate in herpes simplex virus 1 entry. Cell 99, 13-22 (1999).

17. K. Madavaraju, R. Koganti, I. Volety, T. Yadavalli, D. Shukla, Herpes Simplex Virus Cell Entry Mechanisms: An Update. Frontiers in Cellular and Infection Microbiology 10, (2021).

18. S. Boulant, M. Stanifer, P.-Y. Lozach, Dynamics of Virus-Receptor Interactions in Virus Binding, Signaling, and Endocytosis. Viruses. 2015 (10.3390/v7062747).

19. Y. Tufail *et al.*, Phosphatidylserine Exposure Controls Viral Innate Immune Responses by Microglia. *Neuron* **93**, 574-586.e578 (2017).

20. D. Eggink, P. H. Goff, P. Palese, Guiding the Immune Response against Influenza Virus Hemagglutinin toward the Conserved Stalk Domain by Hyperglycosylation of the Globular Head Domain. *Journal of Virology* **88**, 699-704 (2014).

21. D. S. Dimitrov, Virus entry: molecular mechanisms and biomedical applications. *Nature Reviews Microbiology* **2**, 109-122 (2004).

22. S. L. Roth, G. R. Whittaker, Promotion of vesicular stomatitis virus fusion by the endosome-specific phospholipid bis(monoacylglycero)phosphate (BMP). *FEBS Letters* **585**, 865-869 (2011).

23. C. Jolly, I. Mitar, Q. J. Sattentau, Adhesion Molecule Interactions Facilitate Human Immunodeficiency Virus Type 1-Induced Virological Synapse Formation between T Cells. *Journal of Virology* **81**, 13916-13921 (2007).

24. B. Chen, Molecular Mechanism of HIV-1 Entry. *Trends Microbiol.* **27**, 878-891 (2019).

25. M. Sempere Borau, S. Stertz, Entry of influenza A virus into host cells — recent progress and remaining challenges. *Current Opinion in Virology* **48**, 23-29 (2021).

26. P. A. Leventis, S. Grinstein, The Distribution and Function of Phosphatidylserine in Cellular Membranes. *Annual Review of Biophysics* **39**, 407-427 (2010).

27. S. Pietkiewicz, J. H. Schmidt, I. N. Lavrik, Quantification of apoptosis and necroptosis at the single cell level by a combination of Imaging Flow Cytometry with classical Annexin V/propidium iodide staining. *J. Immunol. Methods* **423**, 99-103 (2015).

28. A. Amara, J. Mercer, Viral apoptotic mimicry. *Nature Reviews Microbiology* **13**, 461-469 (2015).

29. J. H. Meyers *et al.*, TIM-4 is the ligand for TIM-1, and the TIM-1–TIM-4 interaction regulates T cell proliferation. *Nature Immunology* **6**, 455-464 (2005).

30. N. Kobayashi *et al.*, TIM-1 and TIM-4 Glycoproteins Bind Phosphatidylserine and Mediate Uptake of Apoptotic Cells. *Immunity* **27**, 927-940 (2007).

31. L. Meertens *et al.*, The TIM and TAM Families of Phosphatidylserine Receptors Mediate Dengue Virus Entry. *Cell Host & Microbe* **12**, 544-557 (2012).

32. S. Jemielity *et al.*, TIM-family Proteins Promote Infection of Multiple Enveloped Viruses through Virion-associated Phosphatidylserine. *PLOS Pathogens* **9**, e1003232 (2013).

33. J. H. M. van der Meer, T. van der Poll, C. van 't Veer, TAM receptors, Gas6, and protein S: roles in inflammation and hemostasis. *Blood* **123**, 2460-2469 (2014).

34. L. Meertens *et al.*, Axl Mediates ZIKA Virus Entry in Human Glial Cells and Modulates Innate Immune Responses. *Cell Reports* **18**, 324-333 (2017).

35. K. Morizono *et al.*, The Soluble Serum Protein Gas6 Bridges Virion Envelope Phosphatidylserine to the TAM Receptor Tyrosine Kinase Axl to Mediate Viral Entry. *Cell Host & Microbe* **9**, 286-298 (2011).

36. X. Carnec *et al.*, The Phosphatidylserine and Phosphatidylethanolamine Receptor CD300a Binds Dengue Virus and Enhances Infection. *Journal of Virology* **90**, 92-102 (2016).

37. A. Marzi *et al.*, DC-SIGN and DC-SIGNR Interact with the Glycoprotein of Marburg Virus and the S Protein of Severe Acute Respiratory Syndrome Coronavirus. *Journal of Virology* **78**, 12090-12095 (2004).

38. S. G. Turville *et al.*, Diversity of receptors binding HIV on dendritic cell subsets. *Nature Immunology* **3**, 975-983 (2002).

39. U. Treichel, K. H. M. zum Büschenfelde, H. P. Dienes, G. Gerken, Receptor-mediated entry of hepatitis B virus particles into liver cells. *Arch. Virol* **142**, 493-498 (1997).

40. B. Saunier *et al.*, Role of the Asialoglycoprotein Receptor in Binding and Entry of Hepatitis C Virus Structural Proteins in Cultured Human Hepatocytes. *Journal of Virology* **77**, 546-559 (2003).

41. W.-S. Ryu, in *Molecular Virology of Human Pathogenic Viruses,* W.-S. Ryu, Ed. (Academic Press, Boston, 2017), pp. 31-45.

42. V. Más, J. A. Melero, in *Structure and Physics of Viruses: An Integrated Textbook,* M. G. Mateu, Ed. (Springer Netherlands, Dordrecht, 2013), pp. 467-487.

43. J. Mercer, M. Schelhaas, A. Helenius, Virus Entry by Endocytosis. *Annual Review of Biochemistry* **79**, 803-833 (2010).

44. E. Zaitseva *et al.*, Fusion Stage of HIV-1 Entry Depends on Virus-Induced Cell Surface Exposure of Phosphatidylserine. *Cell Host & Microbe* **22**, 99-110.e117 (2017).

45. P. D. Uchil, W. Mothes, HIV Entry Revisited. *Cell* **137**, 402-404 (2009).

46. Q. Wang, A. Finzi, J. Sodroski, The Conformational States of the HIV-1 Envelope Glycoproteins. *Trends Microbiol.* **28**, 655-667 (2020).

47. S. C. Harrison, in *Adv. Virus Res.* (Academic Press, 2005), vol. 64, pp. 231-261.

48. J. Mercer, J. E. Lee, E. O. Saphire, S. A. Freeman, SnapShot: Enveloped Virus Entry. *Cell* **182**, 786-786.e781 (2020).

49. J.-h. Wang, Protein recognition by cell surface receptors: physiological receptors versus virus interactions. *Trends in Biochemical Sciences* **27**, 122-126 (2002).

50. J. M. Casasnovas, in *Structure and Physics of Viruses: An Integrated Textbook,* M. G. Mateu, Ed.

(Springer Netherlands, Dordrecht, 2013), pp. 441-466.

51. Ebola Virus Disease in West Africa — The First 9 Months of the Epidemic and Forward Projections. *New England Journal of Medicine* **371**, 1481-1495 (2014).

52. S. Pattyn, G. van der Groen, W. Jacob, P. Piot, G. Courteille, Isolation of Marburg-like virus from a case of haemorrhagic fever in Zaire. *Lancet* **1**, 573-574 (1977).

53. A. S. Magassouba *et al.*, Impact of the Ebola virus disease outbreak (2014–2016) on tuberculosis surveillance activities by Guinea's National Tuberculosis Control Program: a time series analysis. *BMC Public Health* **20**, 1200 (2020).

54. J. Sun *et al.*, Ebola virus outbreak returns to the Democratic Republic of Congo: An urgent rising concern. *Annals of Medicine and Surgery* **79**, (2022).

55. E. Mühlberger, M. Weik, V. E. Volchkov, H.-D. Klenk, S. Becker, Comparison of the Transcription and Replication Strategies of Marburg Virus and Ebola Virus by Using Artificial Replication Systems. *Journal of Virology* **73**, 2333-2342 (1999).

56. L. Baseler, D. S. Chertow, K. M. Johnson, H. Feldmann, D. M. Morens, The Pathogenesis of Ebola Virus Disease. *Annual Review of Pathology: Mechanisms of Disease* **12**, 387-418 (2017).

57. J. Timmins, S. Scianimanico, G. Schoehn, W. Weissenhorn, Vesicular Release of Ebola Virus Matrix Protein VP40. *Virology* **283**, 1-6 (2001).

58. S. Moller-Tank, W. Maury, Phosphatidylserine receptors: Enhancers of enveloped virus entry and infection. *Virology* **468-470**, 565-580 (2014).

59. J. E. Lee *et al.*, Structure of the Ebola virus glycoprotein bound to an antibody from a human survivor. *Nature* **454**, 177-182 (2008).

60. V. N. Malashkevich *et al.*, Core structure of the envelope glycoprotein GP2 from Ebola virus at 1.9-Å resolution. *Proceedings of the National Academy of Sciences* **96**, 2662-2667 (1999).

61 Y. Zhao *et al.*, Toremifene interacts with and destabilizes the Ebola virus glycoprotein. *Nature* **535**, 169-172 (2016).

62. E. E. H. Tran *et al.*, Spatial Localization of the Ebola Virus Glycoprotein Mucin-Like Domain Determined by Cryo-Electron Tomography. *Journal of Virology* **88**, 10958-10962 (2014).

63. J. A. Wilson *et al.*, Epitopes Involved in Antibody-Mediated Protection from Ebola Virus. *Science* **287**, 1664-1666 (2000).

64. J. Misasi *et al.*, Structural and molecular basis for Ebola virus neutralization by protective human antibodies. *Science* **351**, 1343-1346 (2016).

65. L. B. King, B. R. West, S. L. Schendel, E. O. Saphire, The structural basis for filovirus neutralization by monoclonal antibodies. *Curr. Opin. Immunol.* **53**, 196-202 (2018).

66. J. Pallesen *et al.*, Structures of Ebola virus GP and sGP in complex with therapeutic antibodies. *Nature Microbiology* **1**, 16128 (2016).

67. C. D. Murin *et al.*, Structures of protective antibodies reveal sites of vulnerability on Ebola virus. *Proceedings of the National Academy of Sciences* **111**, 17182-17187 (2014).

68. Molecular Mechanism of Externalization of Phosphatidylserine on the Surface of Ebola Virus Particles. *DNA Cell Biol.* **38**, 115-120 (2019).

69. R. A. Davey *et al.*, in *Marburg- and Ebolaviruses: From Ecosystems to Molecules,* E. Mühlberger, L. L. Hensley, J. S. Towner, Eds. (Springer International Publishing, Cham, 2017), pp. 323-352.

70. A. S. Powlesland *et al.*, A Novel Mechanism for LSECtin Binding to Ebola Virus Surface Glycoprotein through Truncated Glycans*. *Journal of Biological Chemistry* **283**, 593-602 (2008).

71. A. Takada *et al.*, Human macrophage C-type lectin specific for galactose and N-acetylgalactosamine promotes filovirus entry. *J Virol* **78**, 2943-2947 (2004).

72. C. P. Alvarez *et al.*, C-type lectins DC-SIGN and L-SIGN mediate cellular entry by Ebola virus in cis and in trans. *J Virol* **76**, 6841-6844 (2002).

73. G. Lin *et al.*, Differential N-Linked Glycosylation of Human Immunodeficiency Virus and Ebola Virus Envelope Glycoproteins Modulates Interactions with DC-SIGN and DC-SIGNR. *Journal of Virology* **77**, 1337-1346 (2003).

74. T. B. H. Geijtenbeek, A. Engering, Y. van Kooyk, DC-SIGN, a C-type lectin on dendritic cells that unveils many aspects of dendritic cell biology. *J. Leukocyte Biol.* **71**, 921-931 (2002).

75. N. J. Lennemann *et al.*, Comprehensive Functional Analysis of N-Linked Glycans on Ebola Virus GP1. *mBio* **5**, e00862-00813 (2014).

76. A.-L. Favier *et al.*, Enhancement of Ebola Virus Infection via Ficolin-1 Interaction with the Mucin Domain of GP Glycoprotein. *Journal of Virology* **90**, 5256-5269 (2016).

77. M. Brudner *et al.*, Lectin-Dependent Enhancement of Ebola Virus Infection via Soluble and Transmembrane C-type Lectin Receptors. *PLOS ONE* **8**, e60838 (2013).

78. M. Shimojima *et al.*, Tyro3 Family-Mediated Cell Entry of Ebola and Marburg Viruses. *Journal of Virology* **80**, 10109-10116 (2006).

79. T. N. Stitt *et al.*, The anticoagulation factor protein S and its relative, Gas6, are ligands for the Tyro 3/Axl family of receptor tyrosine kinases. *Cell* **80**, 661-670 (1995).

80. G. Lemke, C. V. Rothlin, Immunobiology of the TAM receptors. *Nature Reviews Immunology* **8**, 327-336 (2008).

81. A. S. Kondratowicz *et al.*, T-cell immunoglobulin and mucin domain 1 (TIM-1) is a receptor for Zaire Ebolavirus and Lake Victoria Marburgvirus. *Proc Natl Acad Sci U S A* **108**, 8426-8431 (2011).

82. B. A. Rhein, R. B. Brouillette, G. A. Schaack, J. A. Chiorini, W. Maury, Characterization of Human and Murine T-Cell Immunoglobulin Mucin Domain 4 (TIM-4) IgV Domain Residues Critical for Ebola Virus Entry. *Journal of Virology* **90**, 6097-6111 (2016).

83. S. Moller-Tank, A. S. Kondratowicz, R. A. Davey, P. D. Rennert, W. Maury, Role of the

Phosphatidylserine Receptor TIM-1 in Enveloped-Virus Entry. *Journal of Virology* **87**, 8327-8341 (2013).

84. M. F. Saeed, A. A. Kolokoltsov, T. Albrecht, R. A. Davey, Cellular Entry of Ebola Virus Involves Uptake by a Macropinocytosis-Like Mechanism and Subsequent Trafficking through Early and Late Endosomes. *PLOS Pathogens* **6**, e1001110 (2010).

85. K. Chandran, N. J. Sullivan, U. Felbor, S. P. Whelan, J. M. Cunningham, Endosomal Proteolysis of the Ebola Virus Glycoprotein Is Necessary for Infection. *Science* **308**, 1643-1645 (2005).

86. Q. Zhang *et al.*, Entry Dynamics of Single Ebola Virus Revealed by Force Tracing. *ACS Nano* **14**, 7046-7054 (2020).

87. A. Nanbo *et al.*, Ebolavirus Is Internalized into Host Cells via Macropinocytosis in a Viral Glycoprotein-Dependent Manner. *PLOS Pathogens* **6**, e1001121 (2010).

88. J. Mercer, A. Helenius, Virus entry by macropinocytosis. *Nature Cell Biology* **11**, 510-520 (2009).

89. M. Côté *et al.*, Small molecule inhibitors reveal Niemann–Pick C1 is essential for Ebola virus infection. *Nature* **477**, 344-348 (2011).

90. M. A. Whitt, Generation of VSV pseudotypes using recombinant ΔG-VSV for studies on virus entry, identification of entry inhibitors, and immune responses to vaccines. *Journal of Virological Methods* **169**, 365-374 (2010).

91. Q. Chen, K. Tang, X. Zhang, P. Chen, Y. Guo, Establishment of pseudovirus infection mouse models for in vivo pharmacodynamics evaluation of filovirus entry inhibitors. *Acta Pharmaceutica Sinica B* **8**, 200-208 (2018).

92. A. Marzi *et al.*, VSV-EBOV rapidly protects macaques against infection with the 2014/15 Ebola virus outbreak strain. *Science* **349**, 739-742 (2015).

93. A. Salgado-Barreira *et al.*, Effect of dapagliflozin on COVID-19 infection and risk of hospitalization. *J. Antimicrob. Chemother.*, (2023).

94. G. Kampf, D. Todt, S. Pfaender, E. Steinmann, Persistence of coronaviruses on inanimate surfaces and their inactivation with biocidal agents. *J. Hosp. Infect.* **104**, 246-251 (2020).

95. A. E. Gorbalenya *et al.*, The species Severe acute respiratory syndrome-related coronavirus: classifying 2019-nCoV and naming it SARS-CoV-2. *Nature Microbiology* **5**, 536-544 (2020).

96. R. Lu *et al.*, Genomic characterisation and epidemiology of 2019 novel coronavirus: implications for virus origins and receptor binding. *Lancet (London, England)* **395**, 565-574 (2020).

97. W. Li *et al.*, Angiotensin-converting enzyme 2 is a functional receptor for the SARS coronavirus. *Nature* **426**, 450-454 (2003).

98. P. Zhou *et al.*, A pneumonia outbreak associated with a new coronavirus of probable bat origin. *Nature* **579**, 270-273 (2020).

99. N. Wang, J. Shang, S. Jiang, L. Du, Subunit Vaccines Against Emerging Pathogenic Human

Coronaviruses. *Frontiers in Microbiology* **11**, (2020).

100. M. Hoffmann, H. Kleine-Weber, S. Pöhlmann, A Multibasic Cleavage Site in the Spike Protein of SARS-CoV-2 Is Essential for Infection of Human Lung Cells. *Molecular Cell* **78**, 779-784.e775 (2020).

101. Z. Ke *et al.*, Structures and distributions of SARS-CoV-2 spike proteins on intact virions. *Nature* **588**, 498-502 (2020).

102. D. Wrapp *et al.*, Cryo-EM structure of the 2019-nCoV spike in the prefusion conformation. *Science* **367**, 1260-1263 (2020).

103. J. Zhang, T. Xiao, Y. Cai, B. Chen, Structure of SARS-CoV-2 spike protein. *Current Opinion in Virology* **50**, 173-182 (2021).

104. D. J. Benton *et al.*, Receptor binding and priming of the spike protein of SARS-CoV-2 for membrane fusion. *Nature* **588**, 327-330 (2020).

105. T. C. Marcink *et al.*, Intermediates in SARS-CoV-2 spike-mediated cell entry. *Sci Adv* **8**, eabo3153 (2022).

106. X. Chi *et al.*, A neutralizing human antibody binds to the N-terminal domain of the Spike protein of SARS-CoV-2. *Science* **369**, 650-655 (2020).

107. M. McCallum *et al.*, N-terminal domain antigenic mapping reveals a site of vulnerability for SARS-CoV-2. *Cell* **184**, 2332-2347.e2316 (2021).

108. J. Zhang *et al.*, Structural impact on SARS-CoV-2 spike protein by D614G substitution. *Science* **372**, 525-530 (2021).

109. J. Shang *et al.*, Structural basis of receptor recognition by SARS-CoV-2. *Nature* **581**, 221-224 (2020).

110. J. Lan *et al.*, Structure of the SARS-CoV-2 spike receptor-binding domain bound to the ACE2 receptor. *Nature* **581**, 215-220 (2020).

111. P. Tong *et al.*, Memory B cell repertoire for recognition of evolving SARS-CoV-2 spike. *Cell* **184**, 4969-4980.e4915 (2021).

112. V. Monteil *et al.*, Inhibition of SARS-CoV-2 Infections in Engineered Human Tissues Using Clinical-Grade Soluble Human ACE2. *Cell* **181**, 905-913.e907 (2020).

113. Y. Cai *et al.*, Distinct conformational states of SARS-CoV-2 spike protein. *Science* **369**, 1586-1592 (2020).

114. L. Tai *et al.*, Nanometer-resolution in situ structure of the SARS-CoV-2 postfusion spike protein. *Proceedings of the National Academy of Sciences* **118**, e2112703118 (2021).

115. Q. Wang *et al.*, Structural and Functional Basis of SARS-CoV-2 Entry by Using Human ACE2. *Cell* **181**, 894-904.e899 (2020).

116. B. Schurink *et al.*, Viral presence and immunopathology in patients with lethal COVID-19: a prospective autopsy cohort study. *The Lancet Microbe* **1**, e290-e299 (2020).

117. J. Baggen, E. Vanstreels, S. Jansen, D. Daelemans, Cellular host factors for SARS-CoV-2 infection. *Nature Microbiology* **6**, 1219-1232 (2021).

118. T. M. Clausen *et al.*, SARS-CoV-2 Infection Depends on Cellular Heparan Sulfate and ACE2. *Cell* **183**, 1043-1057.e1015 (2020).

119. S. J. L. Petitjean *et al.*, Multivalent 9-O-Acetylated-sialic acid glycoclusters as potent inhibitors for SARS-CoV-2 infection. *Nature Communications* **13**, 2564 (2022).

120. S. Wang *et al.*, AXL is a candidate receptor for SARS-CoV-2 that promotes infection of pulmonary and bronchial epithelial cells. *Cell Research* **31**, 126-140 (2021).

121. L. Cantuti-Castelvetri *et al.*, Neuropilin-1 facilitates SARS-CoV-2 cell entry and infectivity. *Science* **370**, 856-860 (2020).

122. J. D. Simpson *et al.*, Single-Molecule Analysis of SARS-CoV-2 Binding to C-Type Lectin Receptors. *Nano Letters* **23**, 1496-1504 (2023).

123. V. P. Chavda, V. Apostolopoulos, COVID-19 vaccine design and vaccination strategy for emerging variants. *Expert Review of Vaccines* **21**, 1359-1361 (2022).

124. E. Shrock *et al.*, Viral epitope profiling of COVID-19 patients reveals cross-reactivity and correlates of severity. *Science* **370**, eabd4250 (2020).

125. K. W. Ng *et al.*, Preexisting and de novo humoral immunity to SARS-CoV-2 in humans. *Science* **370**, 1339-1343 (2020).

126. G. Binnig, C. F. Quate, C. Gerber, Atomic Force Microscope. *Physical Review Letters* **56**, 930-933 (1986).

127. D. J. Müller, G. Büldt, A. Engel, Force-induced conformational change of bacteriorhodopsin. *Journal of Molecular Biology* **249**, 239-243 (1995).

128. D. J. Müller, F. A. Schabert, G. Büldt, A. Engel, Imaging purple membranes in aqueous solutions at sub-nanometer resolution by atomic force microscopy. *Biophysical Journal* **68**, 1681-1686 (1995).

129. F. A. Schabert, A. Engel, Reproducible acquisition of Escherichia coli porin surface topographs by atomic force microscopy. *Biophysical Journal* **67**, 2394-2403 (1994).

130. F. Ohnesorge *et al.*, Scanning force microscopy studies of the S-layers from Bacillus coagulans E38-66, Bacillus sphaericus CCM2177 and of an antibody binding process. *Ultramicroscopy* **42-44**, 1236-1242 (1992).

131. W. Häberle, J. K. H. Hörber, F. Ohnesorge, D. P. E. Smith, G. Binnig, In situ investigations of single living cells infected by viruses. *Ultramicroscopy* **42-44**, 1161-1167 (1992).

132. H. Clausen-Schaumann, M. Seitz, R. Krautbauer, H. E. Gaub, Force spectroscopy with single bio-molecules. *Curr. Opin. Chem. Biol.* **4**, 524-530 (2000).

133. P. K. Hansma *et al.*, Tapping mode atomic force microscopy in liquids. *Applied Physics Letters* **64**, 1738-1740 (1994).

134. R. García, R. Pérez, Dynamic atomic force microscopy methods. *Surface Science Reports* **47**, 197-301 (2002).

135. Y. Gan, Atomic and subnanometer resolution in ambient conditions by atomic force microscopy. *Surface Science Reports* **64**, 99-121 (2009).

136. H. Seelert *et al.*, Proton-powered turbine of a plant motor. *Nature* **405**, 418-419 (2000).

137. D. Fotiadis *et al.*, Rhodopsin dimers in native disc membranes. *Nature* **421**, 127-128 (2003).

138. E. Henderson, P. G. Haydon, D. S. Sakaguchi, Actin Filament Dynamics in Living Glial Cells Imaged by Atomic Force Microscopy. *Science* **257**, 1944-1946 (1992).

139. C. Goldsbury, J. Kistler, U. Aebi, T. Arvinte, G. J. Cooper, Watching amyloid fibrils grow by time-lapse atomic force microscopy. *J Mol Biol* **285**, 33-39 (1999).

140. D. J. Müller, A. Engel, Voltage and pH-induced channel closure of porin OmpF visualized by atomic force microscopy11Edited by W. Baumeister. *Journal of Molecular Biology* **285**, 1347-1351 (1999).

141. D. Stoffler, K. N. Goldie, B. Feja, U. Aebi, Calcium-mediated structural changes of native nuclear pore complexes monitored by time-lapse atomic force microscopy11Edited by W. Baumeister. *Journal of Molecular Biology* **287**, 741-752 (1999).

142. A. L. B. Pyne *et al.*, Base-pair resolution analysis of the effect of supercoiling on DNA flexibility and major groove recognition by triplex-forming oligonucleotides. *Nature Communications* **12**, 1053 (2021).

143. M.-P. Mingeot-Leclercq, M. Deleu, R. Brasseur, Y. F. Dufrêne, Atomic force microscopy of supported lipid bilayers. *Nature Protocols* **3**, 1654-1659 (2008).

144. D. M. Czajkowsky, E. M. Hotze, Z. Shao, R. K. Tweten, Vertical collapse of a cytolysin prepore moves its transmembrane β-hairpins to the membrane. *The EMBO Journal* **23**, 3206-3215 (2004).

145. S. Scheuring, J. N. Sturgis, Chromatic Adaptation of Photosynthetic Membranes. *Science* **309**, 484-487 (2005).

146. A. Engel, D. J. Müller, Observing single biomolecules at work with the atomic force microscope. *Nat. Struct. Biol.* **7**, 715-718 (2000).

147. D. J. Müller, H.-J. Sass, S. A. Müller, G. Büldt, A. Engel, Surface structures of native bacteriorhodopsin depend on the molecular packing arrangement in the membrane11Edited by W. Baumeister. *Journal of Molecular Biology* **285**, 1903-1909 (1999).

148. T. Uchihashi, N. Kodera, T. Ando, Guide to video recording of structure dynamics and dynamic processes of proteins by high-speed atomic force microscopy. *Nature Protocols* **7**, 1193-1206 (2012).

149. T. Ando *et al.*, High-Speed Atomic Force Microscopy for Studying the Dynamic Behavior of Protein Molecules at Work. *Japanese Journal of Applied Physics* **45**, 1897 (2006).

150. T. Uchihashi, S. Scheuring, Applications of high-speed atomic force microscopy to real-time

visualization of dynamic biomolecular processes. *Biochimica et Biophysica Acta (BBA) - General Subjects* **1862**, 229-240 (2018).

151. T. Ando, T. Uchihashi, S. Scheuring, Filming Biomolecular Processes by High-Speed Atomic Force Microscopy. *Chemical Reviews* **114**, 3120-3188 (2014).

152. T. Ando, High-speed atomic force microscopy. *Curr. Opin. Chem. Biol.* **51**, 105-112 (2019).

153. J. P. Junker, F. Ziegler, M. Rief, Ligand-Dependent Equilibrium Fluctuations of Single Calmodulin Molecules. *Science* **323**, 633-637 (2009).

154. P. Hinterdorfer, W. Baumgartner, H. J. Gruber, K. Schilcher, H. Schindler, Detection and localization of individual antibody-antigen recognition events by atomic force microscopy. *Proceedings of the National Academy of Sciences* **93**, 3477-3481 (1996).

155. D. Alsteens *et al.*, Atomic force microscopy-based characterization and design of biointerfaces. *Nature Reviews Materials* **2**, 17008 (2017).

156. D. J. Müller *et al.*, Atomic Force Microscopy-Based Force Spectroscopy and Multiparametric Imaging of Biomolecular and Cellular Systems. *Chemical Reviews* **121**, 11701-11725 (2021).

157. M. Ludwig, W. Dettmann, H. E. Gaub, Atomic force microscope imaging contrast based on molecular recognition. *Biophysical Journal* **72**, 445-448 (1997).

158. O. H. Willemsen *et al.*, Simultaneous Height and Adhesion Imaging of Antibody-Antigen Interactions by Atomic Force Microscopy. *Biophysical Journal* **75**, 2220-2228 (1998).

159. M. Krieg *et al.*, Atomic force microscopy-based mechanobiology. *Nature Reviews Physics* **1**, 41-57 (2019).

160. E. A. Evans, D. A. Calderwood, Forces and Bond Dynamics in Cell Adhesion. *Science* **316**, 1148-1153 (2007).

161. E. Evans, K. Ritchie, Dynamic strength of molecular adhesion bonds. *Biophysical Journal* **72**, 1541-1555 (1997).

162. R. W. Friddle, A. Noy, J. J. De Yoreo, Interpreting the widespread nonlinear force spectra of intermolecular bonds. *Proceedings of the National Academy of Sciences* **109**, 13573-13578 (2012).

163. R. Merkel, P. Nassoy, A. Leung, K. Ritchie, E. Evans, Energy landscapes of receptor–ligand bonds explored with dynamic force spectroscopy. *Nature* **397**, 50-53 (1999).

164. G. I. Bell, Models for the Specific Adhesion of Cells to Cells. *Science* **200**, 618-627 (1978).

165. F. Claudia, K. W. Angelika, K. Ferdinand, E. G. Hermann, Dynamic single-molecule force spectroscopy: bond rupture analysis with variable spacer length. *Journal of Physics: Condensed Matter* **15**, S1709 (2003).

166. M. Koehler *et al.*, Glycan-mediated enhancement of reovirus receptor binding. *Nature Communications* **10**, 4460 (2019).

167. C. Rankl *et al.*, Multiple receptors involved in human rhinovirus attachment to live cells.

Proceedings of the National Academy of Sciences **105**, 17778-17783 (2008).

168. M. Delguste *et al.*, Multivalent binding of herpesvirus to living cells is tightly regulated during infection. *Science Advances* **4**, eaat1273 (2018).

169. E. Evans, P. Williams, in *Physics of bio-molecules and cells. Physique des biomolécules et des cellules,* F. Flyvbjerg, F. Jülicher, P. Ormos, F. David, Eds. (Springer Berlin Heidelberg, Berlin, Heidelberg, 2002), pp. 145-204.

170. O. K. Dudko, G. Hummer, A. Szabo, Theory, analysis, and interpretation of single-molecule force spectroscopy experiments. *Proceedings of the National Academy of Sciences* **105**, 15755-15760 (2008).

171. O. K. Dudko, G. Hummer, A. Szabo, Intrinsic Rates and Activation Free Energies from Single-Molecule Pulling Experiments. *Physical Review Letters* **96**, 108101 (2006).

172. M. Rief, F. Oesterhelt, B. Heymann, H. E. Gaub, Single Molecule Force Spectroscopy on Polysaccharides by Atomic Force Microscopy. *Science* **275**, 1295-1297 (1997).

173. G. E. Crooks, Entropy production fluctuation theorem and the nonequilibrium work relation for free energy differences. *Physical Review E* **60**, 2721-2726 (1999).

174. G. Hummer, A. Szabo, Free energy reconstruction from nonequilibrium single-molecule pulling experiments. *Proceedings of the National Academy of Sciences* **98**, 3658-3661 (2001).

175. C. Jarzynski, Nonequilibrium Equality for Free Energy Differences. *Physical Review Letters* **78**, 2690-2693 (1997).

176. D. Collin *et al.*, Verification of the Crooks fluctuation theorem and recovery of RNA folding free energies. *Nature* **437**, 231-234 (2005).

177. M. Pfreundschuh, D. Harder, Z. Ucurum, D. Fotiadis, D. J. Müller, Detecting Ligand-Binding Events and Free Energy Landscape while Imaging Membrane Receptors at Subnanometer Resolution. *Nano Letters* **17**, 3261-3269 (2017).

178. D. Alsteens *et al.*, Imaging G protein–coupled receptors while quantifying their ligand-binding free-energy landscape. *Nature Methods* **12**, 845-851 (2015).

179. D. Alsteens *et al.*, Nanomechanical mapping of first binding steps of a virus to animal cells. *Nature Nanotechnology* **12**, 177-183 (2017).

180. C. Rankl *et al.*, in *Atomic Force Microscopy in Biomedical Research: Methods and Protocols,* P. C. Braga, D. Ricci, Eds. (Humana Press, Totowa, NJ, 2011), pp. 197-210.

181. M. Koehler *et al.*, Molecular insights into receptor binding energetics and neutralization of SARS-CoV-2 variants. *Nature Communications* **12**, 6977 (2021).

182. J. Yang *et al.*, Molecular interaction and inhibition of SARS-CoV-2 binding to the ACE2 receptor. *Nature Communications* **11**, 4541 (2020).

183. M. Koehler *et al.*, Reovirus directly engages integrin to recruit clathrin for entry into host cells.

Nature Communications **12**, 2149 (2021).

184. H.-U. Krotil *et al.*, Pulsed force mode: a new method for the investigation of surface properties. *Surface and Interface Analysis* **27**, 336-340 (1999).

185. Y. F. Dufrêne, D. Martínez-Martín, I. Medalsy, D. Alsteens, D. J. Müller, Multiparametric imaging of biological systems by force-distance curve–based AFM. *Nature Methods* **10**, 847-854 (2013).

186. D. Alsteens, H. Trabelsi, P. Soumillion, Y. F. Dufrêne, Multiparametric atomic force microscopy imaging of single bacteriophages extruding from living bacteria. *Nature Communications* **4**, 2926 (2013).

187. M. Pfreundschuh, D. Martinez-Martin, E. Mulvihill, S. Wegmann, D. J. Muller, Multiparametric high-resolution imaging of native proteins by force-distance curve–based AFM. *Nature Protocols* **9**, 1113-1130 (2014).

188. A. C. Dumitru *et al.*, Submolecular probing of the complement C5a receptor–ligand binding reveals a cooperative two-site binding mechanism. *Communications Biology* **3**, 786 (2020).

189. C. Lo Giudice, H. Zhang, B. Wu, D. Alsteens, Mechanochemical Activation of Class-B G-Protein-Coupled Receptor upon Peptide–Ligand Binding. *Nano Letters* **20**, 5575-5582 (2020).

190. E. Dague *et al.*, Chemical Force Microscopy of Single Live Cells. *Nano Letters* **7**, 3026-3030 (2007).

191. V. Dupres *et al.*, The yeast Wsc1 cell surface sensor behaves like a nanospring in vivo. *Nature Chemical Biology* **5**, 857-862 (2009).

192. S. Guo *et al.*, Measuring protein isoelectric points by AFM-based force spectroscopy using trace amounts of sample. *Nature Nanotechnology* **11**, 817-823 (2016).

193. M. Pfreundschuh, U. Hensen, D. J. Müller, Quantitative Imaging of the Electrostatic Field and Potential Generated by a Transmembrane Protein Pore at Subnanometer Resolution. *Nano Letters* **13**, 5585-5593 (2013).

194. E. Mulvihill, M. Pfreundschuh, J. Thoma, N. Ritzmann, D. J. Müller, High-Resolution Imaging of Maltoporin LamB while Quantifying the Free-Energy Landscape and Asymmetry of Sugar Binding. *Nano Letters* **19**, 6442-6453 (2019).

195. M. Pfreundschuh *et al.*, Identifying and quantifying two ligand-binding sites while imaging native human membrane receptors by AFM. *Nature Communications* **6**, 8857 (2015).

196. M. Pfreundschuh, D. Alsteens, M. Hilbert, M. O. Steinmetz, D. J. Müller, Localizing Chemical Groups while Imaging Single Native Proteins by High-Resolution Atomic Force Microscopy. *Nano Letters* **14**, 2957-2964 (2014).

197. D. Kim, O. Sahin, Imaging and three-dimensional reconstruction of chemical groups inside a protein complex using atomic force microscopy. *Nature Nanotechnology* **10**, 264-269 (2015).

198. A. Raab *et al.*, Antibody recognition imaging by force microscopy. *Nature Biotechnology* **17**, 901-

905 (1999).

199. P. R. Laskowski *et al.*, High-Resolution Imaging and Multiparametric Characterization of Native Membranes by Combining Confocal Microscopy and an Atomic Force Microscopy-Based Toolbox. *ACS Nano* **11**, 8292-8301 (2017).

200. G. Zhao *et al.*, Insight into the Different Channel Proteins of Human Red Blood Cell Membranes Revealed by Combined dSTORM and AFM Techniques. *Analytical Chemistry* **93**, 14113-14120 (2021).

201. M. Delguste *et al.*, Single-Virus Force Spectroscopy Discriminates the Intrinsic Role of Two Viral Glycoproteins upon Cell Surface Attachment. *Nano Letters* **21**, 847-853 (2021).

202. D. Mohammed *et al.*, Altered Glycan Expression on Breast Cancer Cells Facilitates Infection by T3 Seroptype Oncolytic Reovirus. *Nano Letters* **21**, 9720-9728 (2021).

203. R. dos Santos Natividade *et al.*, Deciphering molecular mechanisms stabilizing the reovirus-binding complex. *Proceedings of the National Academy of Sciences* **120**, e2220741120 (2023).

204. K. M. Goeders, J. S. Colton, L. A. Bottomley, Microcantilevers: Sensing Chemical Interactions via Mechanical Motion. *Chemical Reviews* **108**, 522-542 (2008).

205. J. W. Ndieyira *et al.*, Nanomechanical detection of antibiotic–mucopeptide binding in a model for superbug drug resistance. *Nature Nanotechnology* **3**, 691-696 (2008).

206. M. P. Stewart, Y. Toyoda, A. A. Hyman, D. J. Müller, Tracking mechanics and volume of globular cells with atomic force microscopy using a constant-height clamp. *Nature Protocols* **7**, 143-154 (2012).

207. D. Martínez-Martín *et al.*, Inertial picobalance reveals fast mass fluctuations in mammalian cells. *Nature* **550**, 500-505 (2017).

208. Y. Pan *et al.*, The Process of Wrapping Virus Revealed by a Force Tracing Technique and Simulations. *Advanced Science* **4**, 1600489 (2017).

209. Y. Pan *et al.*, Ultrafast Tracking of a Single Live Virion During the Invagination of a Cell Membrane. *Small* **11**, 2782-2788 (2015).

210. Y. Pan *et al.*, Single glucose molecule transport process revealed by force tracing and molecular dynamics simulations. *Nanoscale Horizons* **3**, 517-524 (2018).

211. Y.-F. Wang *et al.*, Spatiotemporal Tracing of the Cellular Internalization Process of Rod-Shaped Nanostructures. *ACS Nano* **16**, 4059-4071 (2022).

212. X. Pang *et al.*, Spatiotemporal tracking of the transport of RNA nano-drugs: from transmembrane to intracellular delivery. *Nanoscale* **14**, 8919-8928 (2022).

213. A. F. Oberhauser, P. K. Hansma, M. Carrion-Vazquez, J. M. Fernandez, Stepwise unfolding of titin under force-clamp atomic force microscopy. *Proceedings of the National Academy of Sciences* **98**, 468-472 (2001).

214. J. M. Fernandez, H. Li, Force-Clamp Spectroscopy Monitors the Folding Trajectory of a Single

Protein. *Science* **303**, 1674-1678 (2004).

215. P. J. Bujalowski, A. F. Oberhauser, Tracking unfolding and refolding reactions of single proteins using atomic force microscopy methods. *Methods* **60**, 151-160 (2013).

216. A. Sarkar, R. B. Robertson, J. M. Fernandez, Simultaneous atomic force microscope and fluorescence measurements of protein unfolding using a calibrated evanescent wave. *Proceedings of the National Academy of Sciences* **101**, 12882-12886 (2004).

217. J. Brujić, R. I. Hermans Z, K. A. Walther, J. M. Fernandez, Single-molecule force spectroscopy reveals signatures of glassy dynamics in the energy landscape of ubiquitin. *Nature Physics* **2**, 282-286 (2006).

218. M. Schlierf, H. Li, J. M. Fernandez, The unfolding kinetics of ubiquitin captured with single-molecule force-clamp techniques. *Proceedings of the National Academy of Sciences* **101**, 7299-7304 (2004).

219. J. Schönfelder, R. Perez-Jimenez, V. Muñoz, A simple two-state protein unfolds mechanically via multiple heterogeneous pathways at single-molecule resolution. *Nature Communications* **7**, 11777 (2016).

220. A. E. M. Beedle *et al.*, Forcing the reversibility of a mechanochemical reaction. *Nature Communications* **9**, 3155 (2018).

221. P. Kosuri *et al.*, Protein Folding Drives Disulfide Formation. *Cell* **151**, 794-806 (2012).

222. P. R. Laskowski *et al.*, Monitoring the binding and insertion of a single transmembrane protein by an insertase. *Nature Communications* **12**, 7082 (2021).

Chapter 2:

Aims and strategies

Enveloped viruses, such as EBOV and SARS-CoV-2, share relatively similar entry mechanisms. First, these viruses land on the surface of host cells and concentrate by binding to various more specific attachment factors. This crucial step enables the virus to establish solid anchorage points, paving the way for subsequent entry stages. Secondly, the viruses bind to more specific receptors inducing a change of the viral glycoprotein conformation, revealing target sites for host cell proteases. This step results in the uncapping of the viral glycoproteins and the exposure of the fusion domain. Thirdly, the exposed fusion domain binds itself into the target cell membrane forming a stable bridge between the viral and cellular membrane. Finally, the fusion domain of the virus experiences an irreversible conformation change that brings viral and cellular membranes merging together, completing the process of membrane fusion (**Figure 2.1**).

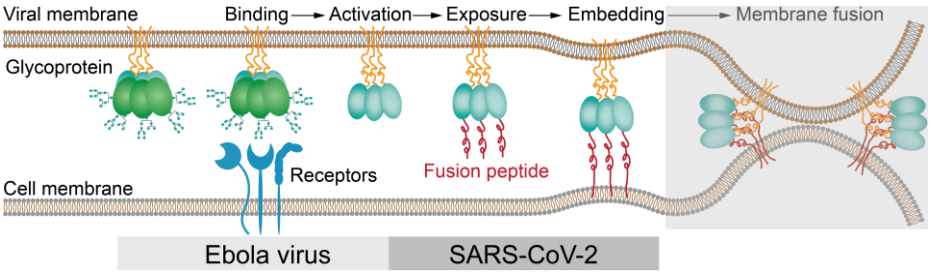

Figure 2: Aims and objectives of the thesis. The different steps involved in the entry of the enveloped virus were studied using different enveloped virus models. In this work, our primary focus lies on the early binding step that precedes membrane fusion. Specifically, we examined the interaction of EBOV with cell surface receptors and investigated the interaction between the fusion peptide (FP) and the cell membrane for SARS-CoV-2.

This thesis will be divided into two parts, which explore these processes in two enveloped viruses, the first focusing on EBOV and the second on SARS-CoV-2. The overarching goal of this study is to explore, on a single-virus level, the molecular mechanisms that underlie the attachment of EBOV and SARS-CoV-2 to host cell surfaces and how host enzymes may impact this process. To accomplish this overarching aim, we will proceed in three steps: the first step (objective i) focuses on methodological development, specifically further developing the AFM force spectroscopy to investigate early binding steps. In the second step, we will address objectives ii-iv, which relate to EBOV. Finally, in the third step, we will address objectives v-vii, which are related to SARS-CoV-2.

i. Develop AFM force spectroscopy to investigate the early binding steps of enveloped virus to cell surface receptors and in particular the height-clamp mode to probe the binding of fusion peptide to cellular membrane.
ii. Study the role of DC-SIGNR and TIM-1 as specific cell surface receptors for EBOV and extract their kinetic and thermodynamic parameters that describe those binding complexes.
iii. Examine the process by which host proteases activate the viral glycoproteins and what effects does it have on the binding of the virus to the cell surface receptors.
iv. How is Ebola binding established in a cellular context?
v. Examine the role of the N-terminal end of the fusion peptide (FP) of SARS-CoV-2 in its interaction with the cell membrane and determine FP's binding capacities concerning various membrane lipids
vi. Investigate the specific role of the disulfide bridge in facilitating the binding of the fusion peptide (FP) into lipid membranes.
vii. Determine the kinetics and thermodynamics governing the binding and insertion of the fusion peptide (FP) into lipid membranes.

To address our first objective of investigating the binding of the Ebola virus to its crucial receptors, we extended the application of atomic force microscopy-based single-molecule force spectroscopy (AFM-SFMS). We utilized AFM-SFMS in combination with host enzymes to investigate the interactions between the Ebola virus and its receptors. Additionally, we employed confocal microscopy and force-distance-based AFM to characterize the binding of the Ebola virus to receptors on living cells.

For the second objective, which involved studying the interaction between the SARS-CoV-2 fusion peptide (FP) and the lipid membrane, we developed AFM-SFMS in height-clamp (HC) mode. This innovative approach enabled us to directly observe the binding of FP to the membrane at the single-molecule level. We applied a single-molecule identification algorithm to analyze force-time data and extracted the thermodynamic parameters of the FP-membrane binding using the Dudko-Hummer-Szabo model. In addition to these techniques, we augmented our research by integrating biolayer interferometry and pseudo-viral infection assays with AFM-SMFS analysis.

The entry steps of enveloped viruses have attracted a great deal of attention, and numerous studies have reported structures describing the entry complexes of these viruses, providing snapshots of the binding partners. However, the molecular mechanisms and in particular their dynamics are largely unknown. A thorough deciphering of these first steps of enveloped virus entry is a crucial challenge in biology, and this work is part of that framework. A better understanding of the kinetics and thermodynamics of these steps is a key issue for the development of vaccines and antiviral agents against diseases caused by these viruses.

Chapter 3:

Stepwise Enzymatic-Dependent Mechanism of Ebola Virus Binding to Cell Surface Receptors Monitored by AFM

Qingrong Zhang[1], Jinsung Yang[1], Sueli Tillieux[1], Zhengyuan Guo[2], Rita dos Santos Natividade[1], Melanie Koehler[1], Simon Petitjean[1], Zongqiang Cui[2], and David Alsteens[1,3,*]

[1]Louvain Institute of Biomolecular Science and Technology, Université catholique de Louvain, Louvain-la-Neuve, Belgium

[2]State Key Laboratory of Virology, Wuhan Institute of Virology, Center for Biosafety Mega-Science, Chinese Academy of Sciences, Wuhan, China

[3]Walloon Excellence in Life sciences and Biotechnology (WELBIO), Wavre, Belgium

*Corresponding author

Author contributions

Q.Z. and D.A. conceived the project. **Q.Z** conducted all experiments. **Q.Z**, J.Y., M.K., R.N., and S.P. analyzed the AFM data. J.Y. and S.T. planned the biochemical experiments and analyzed data. G.Z. and Z.C. conceived and guided the virus-like particles synthesis and receptor expression. All authors wrote the manuscript.

Published in ***Nano Lett.*** 4, 1641–1648 (February 2, 2022)

https://doi.org/10.1021/acs.nanolett.1c04677

Keywords: Ebola virus, DC-SIGNR, TIM-1, attachment, cell surface receptor, atomic force microscopy, single-virus force spectroscopy

3.1 Abstract

Ebola virus (EBOV) is responsible for several outbreaks of hemorrhagic fever with high mortality, raising great public concern. Several cell surface receptors have been identified to mediate EBOV binding and internalization, including phosphatidylserine (PS) receptors (TIM-1) and C-type lectin receptors (DC-SIGNR). However, the role of TIM-1 during early cell surface binding remains elusive and in particular whether TIM-1 acts as a specific receptor for EBOV. Here, we used force–distance curve-based atomic force microscopy (FD-based AFM) to quantify the binding between TIM-1/DC-SIGNR and EBOV glycoprotein (GP) and observed that both receptors specifically bind to GP with high-affinity. Since TIM-1 can also directly interact with PS at the single-molecule level, we also confirmed that TIM-1 acts as dual-function receptors of EBOV. These results highlight the direct involvement of multiple high-affinity receptors in the first steps of binding to cell surfaces, thus offering new perspectives for the development of anti-EBOV therapeutic molecules.

3.2 Introduction

Initially discovered in 1976, Ebola virus disease is a severe and often fatal illness affecting humans and other primates (*1*). Unlike previous epidemics, the 2014–2016 epidemic spread in West Africa through several countries and is still circulating in several African countries, raising fears of the worst internationally. Among the Ebola various strains, the Zaire Ebolavirus (EBOV) is the most widespread (*2*). EBOV is a single-stranded RNA enveloped virus encoding for seven structural proteins (*3,4*) and possesses a striking filamentous structure. The viral envelope consists of phosphatidylserine (PS)-enriched lipid-bilayer (*5*) decorated with spikes consisting of the glycoprotein (GP) trimer (**Figure 3.1a**) (*6*). Since last year, a vaccine is available but not suitable for an outbreak response where immediate protection is required. However, currently the poor understanding of cellular receptor role is a major roadblock in the understanding of EBOV pathogenesis and the development of antiviral therapies, needed to treat the disease.

EBOV infects a wide range of host cells (*7*) and a variety of cell surface receptors have been identified or hypothesized to mediate EBOV binding and internalization into the endosomal compartment of cells, including PS receptors and C-type lectin receptors (*8–10*). PS receptors and in particular the T-cell Ig and mucin domain 1 (TIM-1) receptor has been shown to interact with the viral PS (*11,12*), mediating GP-independent virus uptake. However, evidence also suggests a direct interaction between TIM-1 and EBOV glycoprotein (EBOV-GP) (*13*), questioning the exact role of TIM-1 during virus binding and infection. Besides TIM-1, the C-type lectin dendritic cell-specific intercellular adhesion molecule-3-

grabbing nonintegrin receptor (DC-SIGNR) has been identified to specifically bind to EBOV-GP contributing to EBOV binding to host cell surface (*14,15*). After EBOV attachment to the cell surface, the viral particles are internalized into early endosomes, where GP is cleaved to GP_{cl} by cathepsin-B and cathepsin-L (Cat-B/L) in a low-pH-dependent manner (**Figure 3.1b**) (*16,17*). The GP_{cl} then interacts with the Niemann-Pick C1 receptor triggering membrane fusion (*18*). In addition, the GP can be cleaved by the tumor necrosis factor-α converting enzyme (TACE) at the membrane-proximal external region (**Figure 3.1b**) (*19,20*). Overall, the mechanism of molecular binding of EBOV to the cell surface is still unclear, in particular the role of TIM-1 in binding to the GP glycoprotein during attachment of virions to the cell surface.

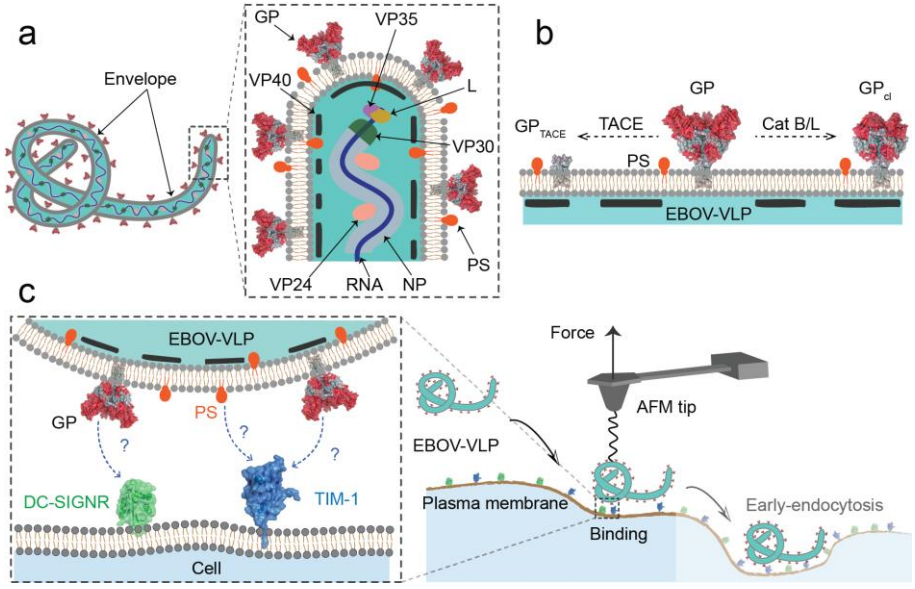

Figure 3.1: Schematic of EBOV and AFM probing of EBOV binding to living cells. (**a**) Schematic of EBOV, the nucleoprotein (NP) encases the viral RNA genome to form a protein–RNA complex. The viral RNA genome interacts with the virion-associated proteins VP24, transcriptional activator VP30, polymerase cofactor VP35, and polymerase L. This complex is surrounded by the matrix protein VP40, which is the main protein controlling virion morphology and budding. These inner components are packed in an envelope of lipid bilayer containing phosphatidylserine (PS). The trimers of glycoprotein (GP) spike are embedded in the viral envelope (*4*). (**b**) Schematic of protease cleavages of EBOV-GP. GP is cleaved at a membrane-proximal external region by the tumor necrosis factor-α converting enzyme (TACE). Endosomal cysteine proteases Cat B/L cleaves GP species to generate GP_{cl}. (**c**) Cartoon showing the probing of EBOV-VLP to cell surface receptors, in particular DC-SIGNR and TIM-1 (PDB IDs: DC-SIGNR, 1K9J; TIM-1, 5DZO; GP, 5JQ3).

To clarify the role of human host receptors during early binding events of EBOV to cell surfaces, we used force–distance (FD) curve-based atomic force microscopy (AFM) (**Figure 3.1c**) (*21*) and probed at the single virus-like particle (VLP) level, the interactions toward DC-SIGNR and TIM-1 receptors, both on purified receptors and on living cells. We first extracted the kinetics and thermodynamics parameters of the individual

interactions and further evaluated the binding capacity of EBOV-receptors on living cells. We evidenced that GP specifically interacts with both DC-SIGNR and TIM-1 with a high-affinity (~150–200 nM). Treatment with Cat-B/L and TACE also suggests that TIM-1 also interacts with PS, providing the first direct evidence that TIM-1 acts as a dual attachment receptor for EBOV. However, the interaction between TIM-1 and PS mainly occurs after enzymatic cleavage of GP, presumably within the endosome.

3.3 Results

EBOV specifically binds to both DC-SIGNR and TIM-1

To evaluate the role of PS receptors and C-type lectin receptors during EBOV early binding to cell surface, we evaluated the binding potential of EBOV to purified receptors using FD-curve based AFM. To this end, DC-SIGNR or TIM-1 were covalently grafted to gold surfaces coated with COOH- and OH-terminated alkanethiols through carbodiimide conjugation (**see 3.5 Methods**). The grafted surfaces were validated by AFM scratching, showing a deposited layer of ~1.5 nm and ~2.0 nm for DC-SIGNR and TIM-1, respectively (**Figure 3.2a, b**). EBOV-like particles (EBOV-VLPs) were produced by expressing the EBOV-GP and mCherry-labeled matrix protein VP40 as previously described (*22*). Confocal laser-scanning microscopy and AFM imaging were used to validate the production of EBOV-VLPs (**Figure 3.3a, b**).

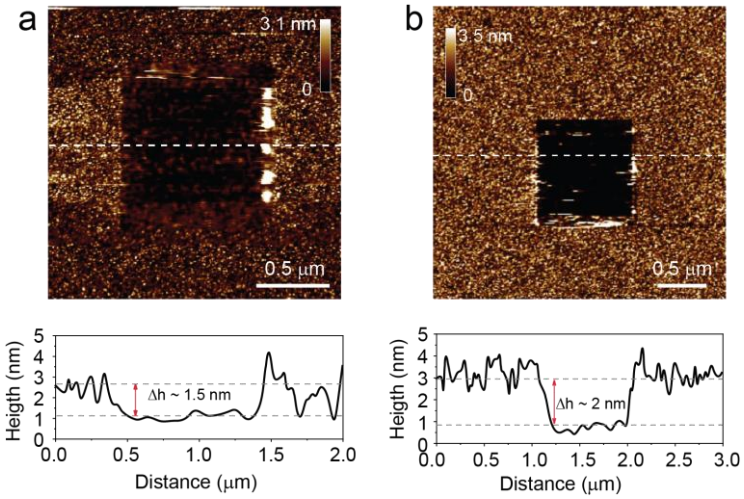

Figure 3.2: Characterization of the receptors-coated surface. AFM topography image of the DC-SIGNR-coated surface (**a**) and TIM-1 (**b**) after scanning of a 1 x 1 µm area in the center with a high applied force (~ 18 nN) to remove attached molecules (upper). The

surface thickness was shown along the white dashed line (under). The center area was ~ 1.5 nm or ~ 2 nm lower than the surrounding biomolecule-coated surface for DC-SIGNR or TIM-1, showing an approximation of their thickness.

Purified EBOV-VLPs were then covalently immobilized onto the AFM tips using a 24-unit long polyethylene glycol (PEG) spacer and the grafting procedure was validated by confocal laser-scanning microscopy (**Figure 3.5a** and **Figure 3.3c, d**).

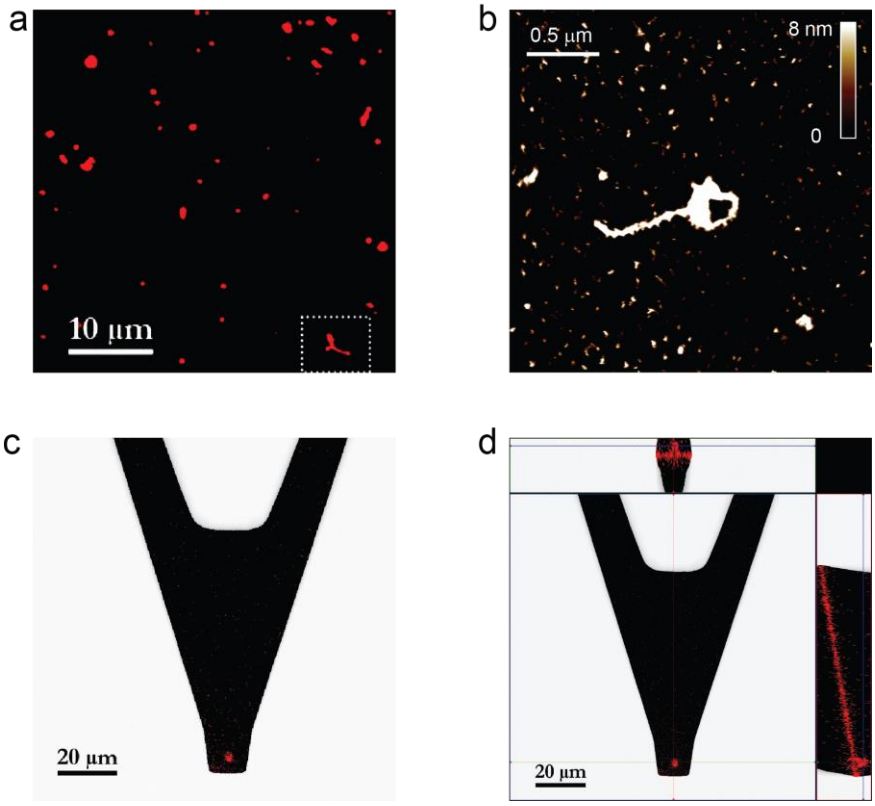

Figure 3.3: Validation of EBOV-VLPs and AFM tip functionalization. **a** Fluorescence image of EBOV-VLPs with the VP40 fused to mCherry. **b** AFM topography image of EBOV-VLPs coated on the clean glass surface and then dried in air. **c, d** Image of an AFM tip functionalized with EBOV-VLPs using laser-scanning confocal microscopy. The image shows the virion at the tip apex (**c**).

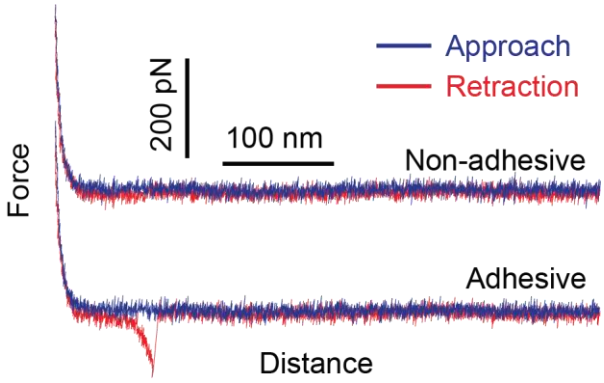

Figure 3.4: Representative FD curves recorded on the model surface showing a non-adhesive curve (upper curve) and an adhesive curve with a specific adhesion event (under curve) for TIM-1.

In order to evaluate the binding between EBOV-VLPs and both receptors, FD curves were recorded by repeatedly approaching and retracting the functionalized tip from the DC-SIGNR or TIM-1 decorated model surface with a surface delay of 200 ms (**Figure 3.5a, b** and **Figure 3.4**). Specific binding events were observed in 16.3 ± 1.6% and 33.5 ± 2.9% of retraction FD curves for DC-SIGNR and TIM-1, respectively (**Figure 3.5c**). To confirm the binding specificity, several independent controls were performed using (i) an coated OH-/COOH-terminated alkanethiol coated surfaces lacking the individual receptors, (ii) a tip functionalized with the PEG spacer but no EBOV-VLPs, and (iii) the injection of 10 nM free antibodies (Ab) (DC-SIGNR Ab or TIM-1 Ab). All three controls result in a significant drop of the binding probability (BP), confirming the specificity of the probed interaction between EBOV-VLPs and DC-SIGNR or TIM-1 (**Figure 3.5c**).

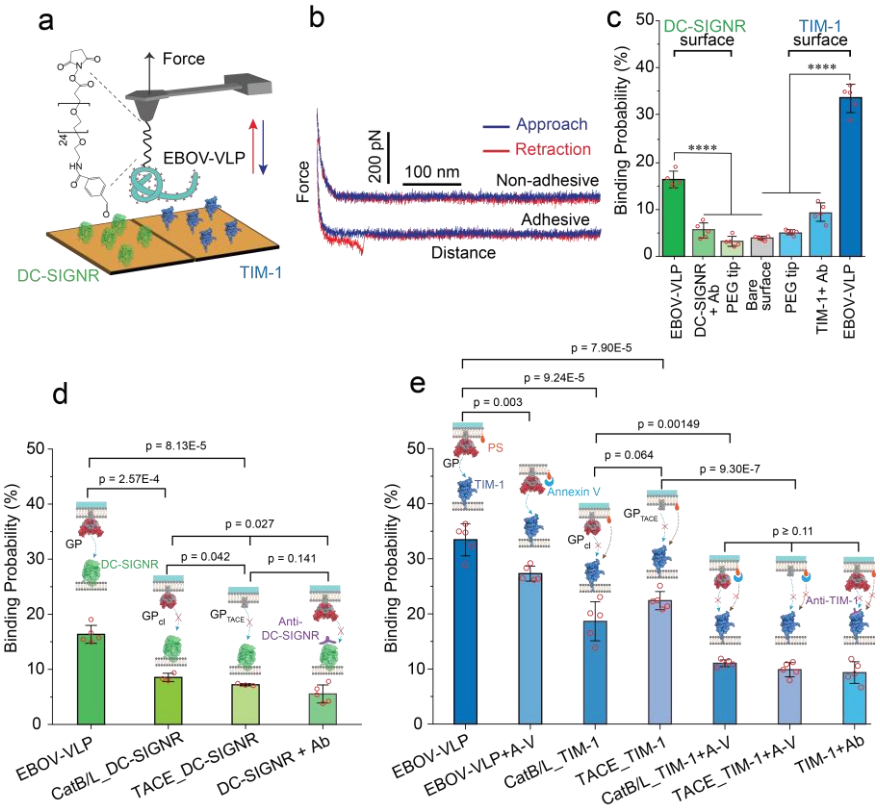

Figure 3.5: EBOV-VLPs specifically binds to purified receptors. (**a**) Schematic of the functionalized of the AFM tip with a PEG_{24} spacer that grafted to the free amino group of EBOV-VLP. (**b**) Representative FD curves recorded on the model surface showing nonadhesion and specific adhesion event. (**c**) Binding probabilities (BP) of specific adhesion events recorded between EBOV-VLP and different receptors and measured by AFM. Red circle indicates individual data points (extracted from independent individual maps), the box indicates the mean, and whiskers indicate the mean ± standard deviation (s.d.). (**d, e**) The BP of EBOV-VLP binding to DC-SIGNR (**d**) or TIM-1 (**e**) before or after treatment with TACE, CatB/L proteases, Annexin-V, and TIM-1 Ab. All experiments were independently reproduced at least three times ($n \geq 3$). **** $P < 0.0001$, P values were determined by a two-sample t test using Origin. Error bars indicate s.d. of mean.

TIM-1 binds both PS and EBOV-GP

In order to identify which EBOV ligands are involved in host receptor binding, we combined the use of native and protease-treated virions yielding different forms of cleaved EBOV-GP. Using FD-curve-based AFM, we compared the BP of the interaction between EBOV-VLP and DC-SIGNR before and after treatment with CatB/L or TACE proteases (**Figure 3.6**). We observed significant drops in the BP after each protease treatment (**Figure 3.5d**) from 16.3 ± 1.6% before treatment to 8.5 ± 0.7% and 7.2 ± 0.2% using CatB/L or TACE treatments, respectively (**Figure 3.5d**). The low BP observed after the protease treatment is also very close to the value obtained after blocking with DC-SIGNR Ab, suggesting that no other viral surface component is involved in the binding to DC-SIGNR.

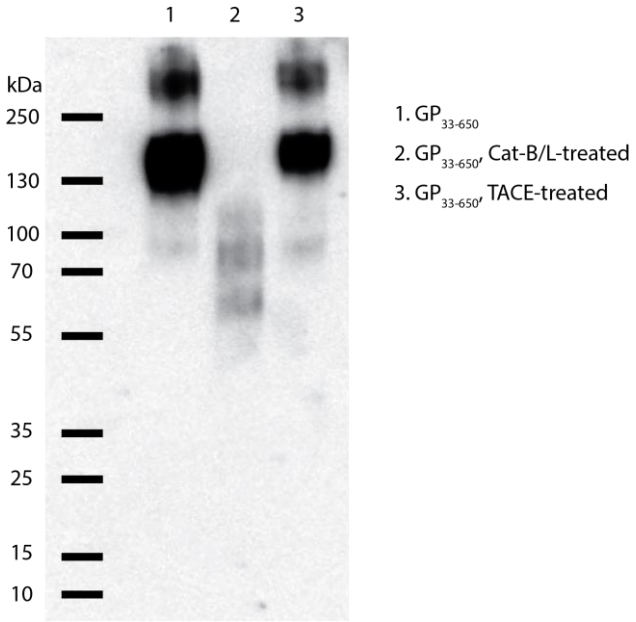

Figure 3.6: The validation of Cat-B/L and TACE protease activities. The sizes of GP, Cat-B/L treated GP, and TACE treated GP were verified by western blot. The western blot was performed with anti-GP antibody.

Similarly, we evaluated the role of EBOV-GP and PS as potential binding ligands for TIM-1. Using Annexin-V, known to specifically bind to PS, we only observed a small decrease of the BP (from 33.5 ± 2.9% to 27.3 ± 1.5%, *n* = 5), suggesting that PS is poorly accessible to TIM-1 on native EBOV-VLP. After treatment with CatB/L or TACE, the BP significantly decreased (from 33.5 ± 2.9% before treatment to 18.6 ± 3.5% and 22.4 ± 1.6% using CatB/L or TACE, respectively), confirming that EBOV-GP is directly involved in TIM-1 binding, as previously suggested (*13,23*) (**Figure 3.5e**). However, the BP remained largely above the value observed after blocking with TIM-1 Ab, confirming that PS and GP could act as a second-attachment ligand. To further validate this, we treated the EBOV-VLPs with each protease and further incubated them with Annexin-V. For both proteases, the coincubation with Annexin-V resulted in a further drop of the BP to the same level as that observed for the incubation with TIM-1 Ab (**Figure 3.5e**). Taken together, these experiments identify TIM-1 as a cellular receptor interacting with both EBOV-GP and PS, while DC-SIGNR exclusively interacts with EBOV-GP.

Extracting the binding free-energy landscape of EBOV to cell surface receptors

After having identified DC-SIGNR and TIM-1 as cellular receptors for EBOV, we sought to characterize their kinetic and thermodynamic properties (**Figure 3.7a, b**) via force-probing their interactions at various loading rates (**Figure 3.7c**). Experimentally, the EBOV-VLP functionalized tip is approached at a constant speed toward the functionalized surface and maintained in contact for 200 ms, thus allowing the establishment of the bond formation. Next, the tip is retracted at various speeds in the range of 0.1–20 μm s^{-1} (**Figure 3.7d**). From the individual force versus time curves (**Figure 3.7c**), the rupture force and corresponding loading rate (LR, slope of the curve just before the rupture occurs) were extracted and displayed as individual data points on the dynamic force spectroscopy (DFS) plots (**Figure 3.7e, f**). If an external force is applied on a reversible bond, the activation-energy barrier of the molecular bond is reduced toward dissociation and shortens its lifetime as described by Bell-Evans model (**Figure 3.7b**) (*24,25*). In the far-from-equilibrium regime, the model therefore predicts that the rupture force of the bonded molecule pairs is proportional to the logarithm of the LR, as we observe for both receptors (**Figure 7e, f**).

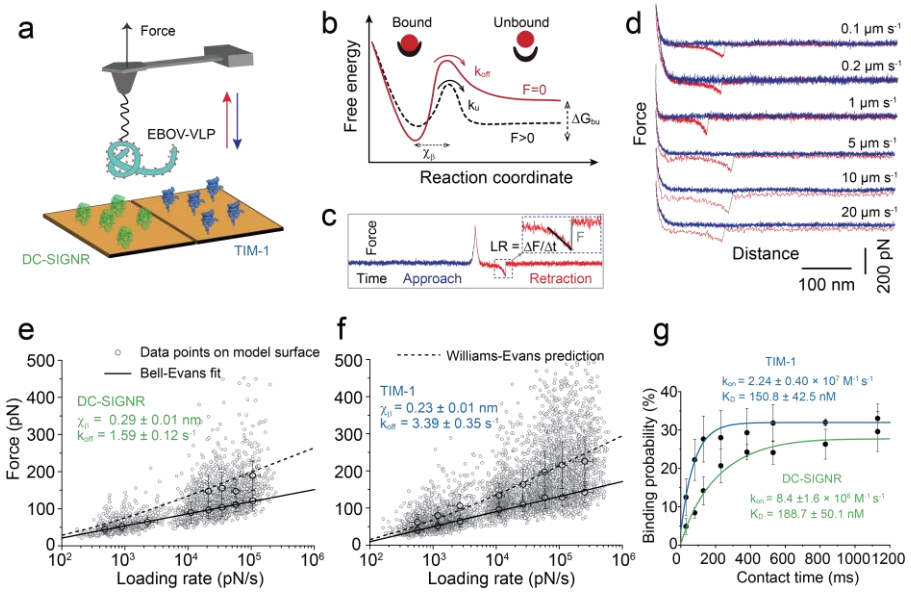

Figure 3.7: Probing EBOV-VLP binding to receptors on model surface. (**a**) Cartoon showing the probing of EBOV-VLPs to DC-SIGNR and TIM-1 receptors on the model surface and EBOV-VLPs on AFM tip. (**b**) Binding between a ligand and a receptor can be described as a two-state by the Bell-Evans model. The transition from the bound state to the unbound state is separated by an energy barrier located at distance χ_β. k_{off}, and k_u indicate the dissociation rate observe with no external force (F = 0) or an external force F > 0 applied onto the bond. (**c**) Force versus time curve where the slope of the curve extracted just before the unbinding event is determined to extract the loading rate (LR). (**d**) Representative force–distance curves recorded at various retraction speeds (from 0.1 to 20 µm s^{-1}) on model surface and showing specific adhesion events. (**e, f**) Dynamic force spectroscopy (DFS) plot indicating the distribution of the rupture forces at different LR ranges for interactions between EBOV-VLP and DC-SIGNR (n = 2242 data points) (**e**) or TIM-1 (n = 5220 data points) (**f**). The solid line represents the fit of the single-bond rupture events with the Bell-Evans fit, giving k_{off} and χ_β values. Dashed lines represent the prediction of the force for the rupture of two simultaneous uncorrelated interactions (using the Williams-Evans prediction). (**g**) The BP acquired at 1 µm s^{-1} is plotted as a function at the different contact times. A monoexponential growth curve (line) using the least-squares fit provides access to the k_{on} of the probed interactions. K_D (k_{off}/k_{on}) value shows that EBOV-VLP has a higher affinity for DC-SIGNR and TIM-1. All experiments were reproduced three times with independent tips and samples ($n \geq 3$) at least and the error bar shows s.d. of the mean value.

For both DC-SIGNR and TIM-1, the probed interaction forces are in the range of 25–500 pN in the comprised LR range from 10^2 to 10^6 pN s^{-1} (**Figures 3.8** and **9**). The analysis of narrow LR ranges revealed force distributions that follow a multiple Gaussian peak distribution, suggesting the establishment of multiple bonds. For each peak, the average force was extracted and displayed on the respective DFS plots (**Figure 3.7e, f**). As predicted by the Bell-Evans model, the points for the first peaks extracted from the histograms were following a linear trend onto the DFS plot (solid lines in **Figure 3.7e, f**), enabling to extract their kinetics parameters, i.e., the distance to the transition state (χ_β) and the kinetic off-rate (k_{off}). The binding of the EBOV-VLP to both receptors is described by a single energy barrier with χ_β = 0.29 ± 0.01 nm and k_{off} = 1.59 ± 0.12 s^{-1} for DC-SIGNR, and χ_β = 0.23 ± 0.01 nm and k_{off} = 3.39 ± 0.35 s^{-1} for TIM-1, in good agreement with previous work (*26*). The k_{off} is directly related to the bond lifetime τ (the time interval required for bond dissociation under equilibrium conditions, $\tau = 1/k_{off}$), which is commonly used to describe the intrinsic parameter of the bond mechanical stability. Our results give lifetimes of τ ≈ 630 ms and τ ≈ 300 ms for the bond established between EBOV-VLP and DC-SINGR or TIM-1, respectively. These results reveal a two-fold-higher stability for the binding to DC-SIGNR, probably explained by the EBOV tropism as DC-SIGNR is expressed in several early targets for EBOV infection, including dendritic cells, alveolar macrophages, and sinusoidal endothelial cells in the liver and lymph node (*14*).

Analysis of the rupture forces also revealed higher forces in the DFS plot (**Figure 3.7e, f**) and respective force histograms (**Figures 3.8** and **9**), which can be fitted with a second peak within the multiple Gaussian peak distribution. Further analysis using the predictive Williams-Evans model

(*27,28*), which determines whether these higher forces could originate from multiple uncorrelated bonds loaded in parallel between the EBOV-VLPs and the receptors, suggests no particular mechanical coupling between the individual bonds (**Figure 3.7e, f**, dashed curves).

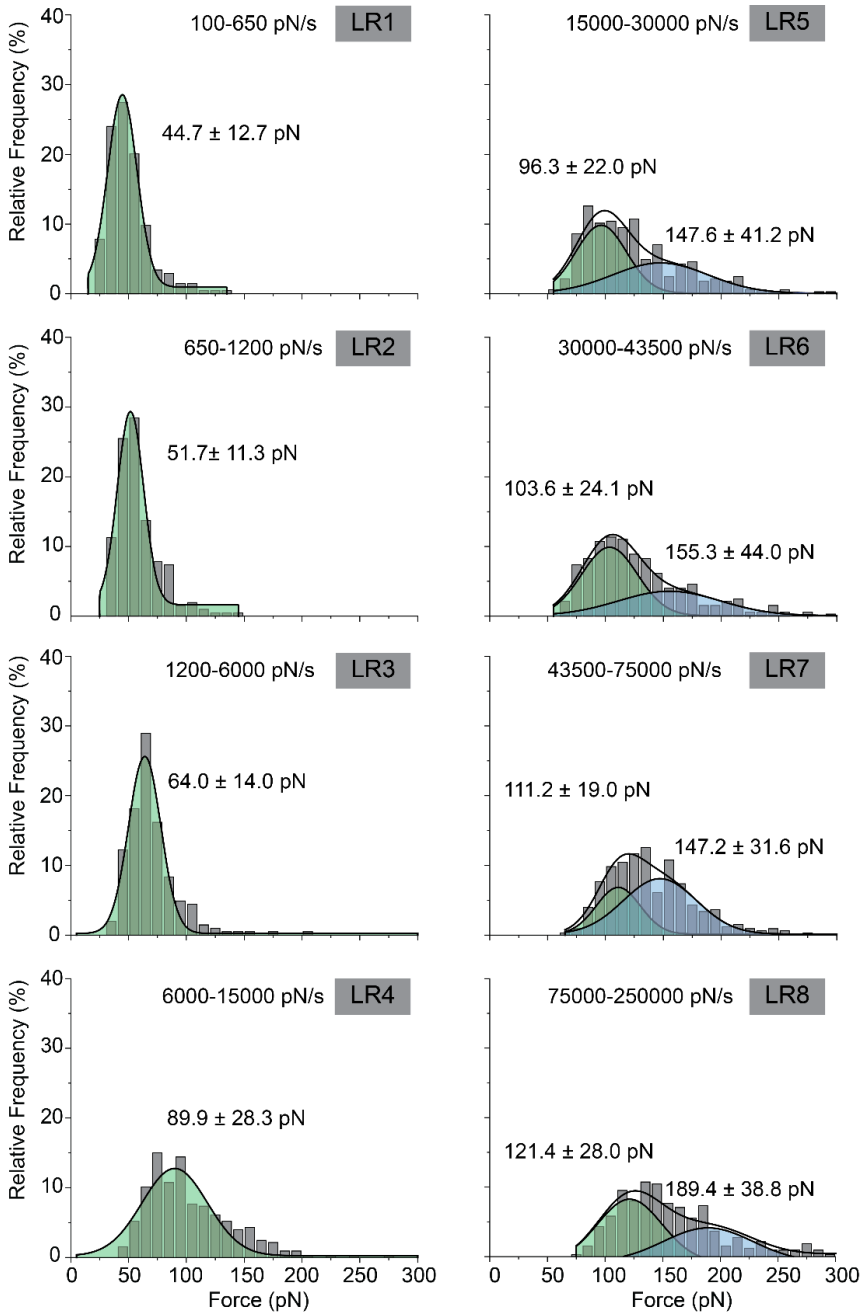

Figure 3.8: Extraction of average rupture force EBOV-VLP binding to DC-SIGNR. The LRs (from **Figure 3.7e**) are divided into narrow LR ranges #1-#8. The distribution of rupture forces located in small LR is plotted as histograms and fitted by multipeak Gaussian Fits.

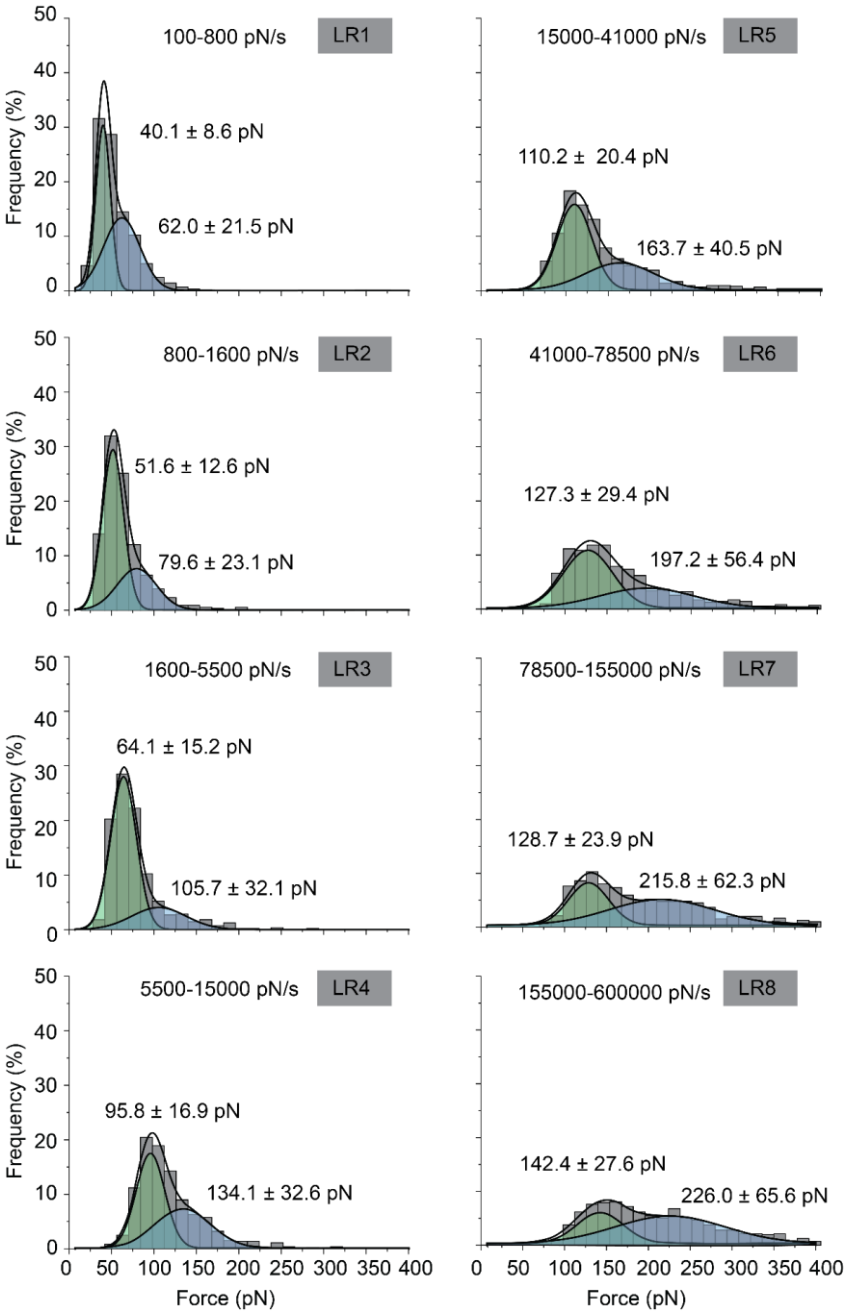

Figure 3.9: Extraction of average rupture force EBOV-VLP binding TIM-1**.** The LRs (from **Figure 3.7f**) are divided into narrow LR ranges #1-#8. The distribution of rupture forces located in small LR is plotted as histograms and fitted by multipeak Gaussian Fits.

Assuming that the receptor-bond complexes can be approximated by a pseudo-first-order kinetics, we also estimated the kinetic on-rate (k_{on}) from our single-molecule force spectroscopy experiments (*29*). This association rate is extracted from the BP measured at various contact times and depends on the effective concentration described as the number of binding partners (ligand + receptor) within an effective volume V_{eff} accessible under free-equilibrium interaction. V_{eff} can be approximated by a half-sphere with a radius including the linker, the viral GP and the receptors (**see 3.5 Methods**) (*29,30*). For both DC-SIGNR and TIM-1, we observed that the BP increased exponentially with contact time, and we extracted interaction times of ~200 and 80 ms, leading to k_{on} values of 8.4 ± 1.6 × 10^6 M^{-1} s^{-1} and 2.2 ± 0.4 × 10^7 M^{-1} s^{-1}, respectively (**Figure 3.7g**). Finally, the dissociation constant K_D is calculated as the ratio between k_{off} and k_{on}, yielding values around ~150–200 nM for both complexes, which is close to the ~26 nM affinity found previously for EBOV-GP–DC-SIGNR (*31*). These experiments demonstrate that EBOV-VLP can specifically bind to both DC-SIGNR and TIM-1 via high-affinity interactions *in vitro*.

TIM-1 acts as the first foothold for EBOV-GP binding

While our first experiments on purified proteins revealed that EBOV-VLPs can bind to TIM-1 through both GP and PS (after cleavage by the proteases), the extraction of the kinetics and thermodynamics revealed only one type of interaction. Therefore, we aimed to determine whether this interaction, recorded with native EBOV-VLPs, originated from binding to EBOV-GP. To this end, we functionalized the AFM tip with the purified EBOV-GP and probed the interaction to both DC-SIGNR and TIM-1 (**Figure 3.10** and **Table 1**).

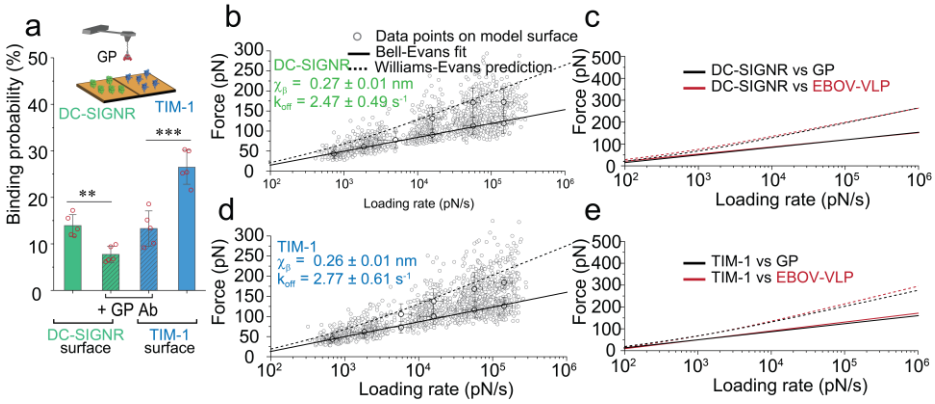

Figure 3.10: GP binding to receptors on model surface. **a** Box plot of the binding probability of GP in absence and presence of EBOV-GP antibodies (** and *** indicate p-values = 0.0015 and = 5.13E-4; n=5). P values were determined by a two-sample t-test using Origin. **b,d** DFS shows the interaction force between GP and DC-SIGNR or TIM-1 (n> 1200 data points). **c,e** Comparison of force required to rupture bonds between receptors and purified GP (black) or EBOV-VLP (red). All data are representative of n = 3 independent experiments.

As anticipated, for DC-SIGNR we obtained a very good agreement between the parameters extracted using the EBOV-VLPs compared to the one using the purified GP (**Figure 3.10b, c**). Stunningly, this is also the case for the complex GP-TIM-1, implying that the EBOV-VLPs would mainly interact with TIM-1 through its GP during the early binding events (**Figure 3.10d, e**). This also indicates that binding to PS may occur later during the subsequent step of the infection. Since GP, due to its size, can potentially sterically hinder PS binding, this step could only take place further downstream, once GP is cleaved by CatB/L, just before its internalization into the endosomes (*32*).

Table 1. Comparison of kinetic and thermodynamic parameters describing EBOV-VLP and GP interaction with receptors (DC-SIGNR and TIM-1).

Pairs of interaction	k_{off} (s^{-1})	χ_β (nm)
DC-SIGNR vs EBOV-VLP	1.59	0.29
DC-SIGNR vs GP	2.47	0.27
TIM-1 vs EBOV-VLP	3.39	0.23
TIM-1 vs GP	2.77	0.26

Exploring EBOV-VLPs binding to cellular receptors on living cells

After the extraction of the parameters describing the binding free-energy landscape of EBOV to its cellular receptors on purified receptors, we wanted to further validate that these binding events are also established in a cellular context. To this end, HEK-293T cells were first transiently transfected with DC-SIGNR-GFP. The expression of DC-SIGNR on HEK-293T cells was validated using in-cell-western assays (**Figure 3.12**). Next, HEK-293T and HEK-293T-DC-SIGNR-GFP were cocultured and imaged using AFM tips functionalized with EBOV-VLPs under physiologically relevant conditions (37 °C, 95% relative humidity and 5% CO_2) (**Figure 3.11a**, inset) (*33*). Guided by fluorescence, an area where control and transfected cells were adjacent was selected and imaged. This allowed us to directly assess the proportion of specific interactions to a particular receptor compared to other interactions that might be established with constitutively expressed receptors at the cell surface (**Figure 3.11a, b, d, e**). From the adhesion map (**Figure 3.11b**), a clear difference appears between the control and transfected cells. While control cells show only rare adhesion events (bright pixels, ~1.5%), the transfected cells show a much higher density of adhesion events (~9.3%), homogeneously distributed on the cell surface (**Figure 3.11a, b**).

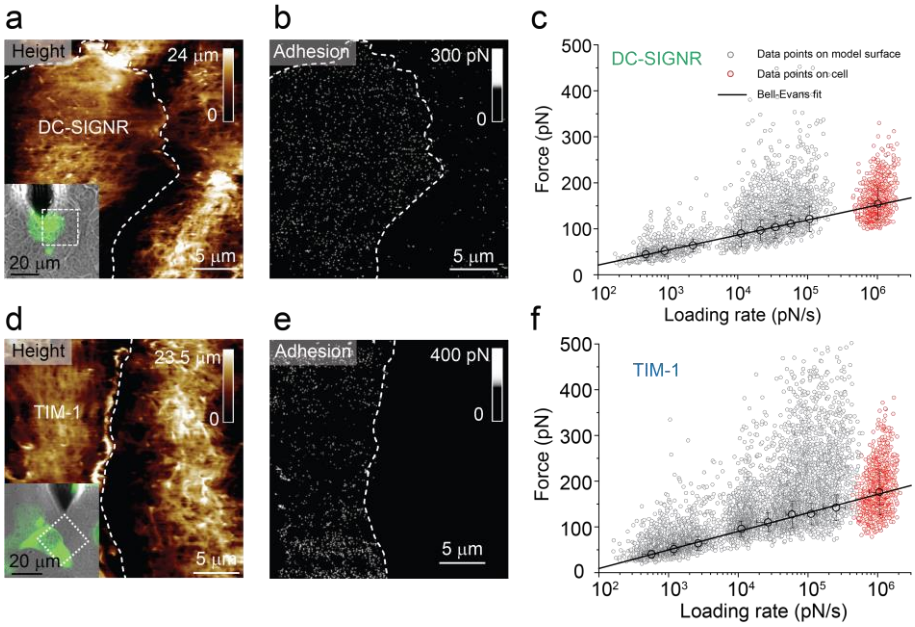

Figure 3.11: Exploring EBOV-VLPs binding to DC-SIGNR or TIM-1 on living cells. (**a**) AFM height image of two adjacent HEK 293T cells: DC-SIGNR (fluorescently tagged) cell and an unlabeled negative control cell. Inset: overlay of fluorescent and DIC images of both cells. (**b**) FD-based AFM adhesion map of cells recorded in the dashed square shown in (**a**) (inset). (**c**) DFS plots of data obtained using model surfaces (gray circles, from **Figure 3.7d**) and on living cells (red circles, *n* = 778 data points from three independent experiments). (**d**) AFM height image with fluorescence image in the inset showing the TIM-1 cell (green) and an unlabeled negative control cell. (**e**) Corresponding adhesion map recorded with EBOV-VLPs. EBOV-VLPs bind strongly to TIM-1 cells (green) in comparison to the unlabeled cell shown in (**d**) (inset). (**f**) DFS plots of TIM-1-EBOV-VLPs obtained using model surfaces (gray circles, from **Figure 3.7e**) and on living cells (red circles, *n* = 908 data points from three independent experiments).

Typical FD curves between EBOV-VLP and HEK-293T-DC-SIGNR-GFP cells showed specific adhesion events on the retraction curve (**Figure 3.13**) with rupture forces in the range of 100 to 300 pN across the applied LR range (**Figure 3.13b**). Naturally, due to the PEG spacer, the size of the attached EBOV-VLPs, and the elasticity of the cell surface and rupture distances can exceed 200 nm. Overlay of the data on the DFS plot obtained

for the purified DC-SIGNR reveals that the binding force for the single-bond matches very well with the value predicted from our above experiments (**Figure 3.11c**). Strikingly, despite the short contact time of ~1 ms with the cell surface, specific binding events with DC-SIGNR are established even in a complex cellular environment. Together, these results indicate that EBOV-VLP interacts with DC-SIGNR on cell surfaces using similar high-affinity interactions as measured on model surfaces.

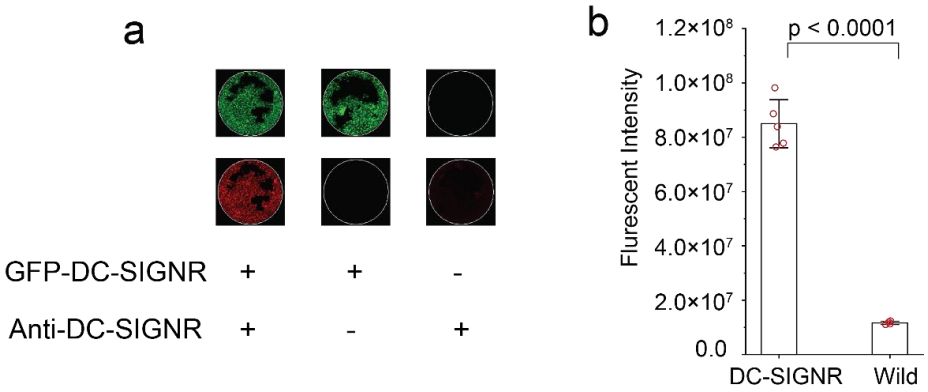

Figure 3.12: Analyzing the expression of DC-SIGNR on HEK 293T cells using the in-cell western. **a** Identical number of cells were seeded in 96 well microplates. green fluorescence signals from DC-SIGNR-GEP (upper) and red fluorescence signals (upper) from anti-DC-SIGNR antibody indicate the DC-SIGNR expressing on cell surface. **b** Quantification of the duplicate results in **a**. P values were determined by a two-sample t-test using Origin. The error bar shows s.d. of the mean value.

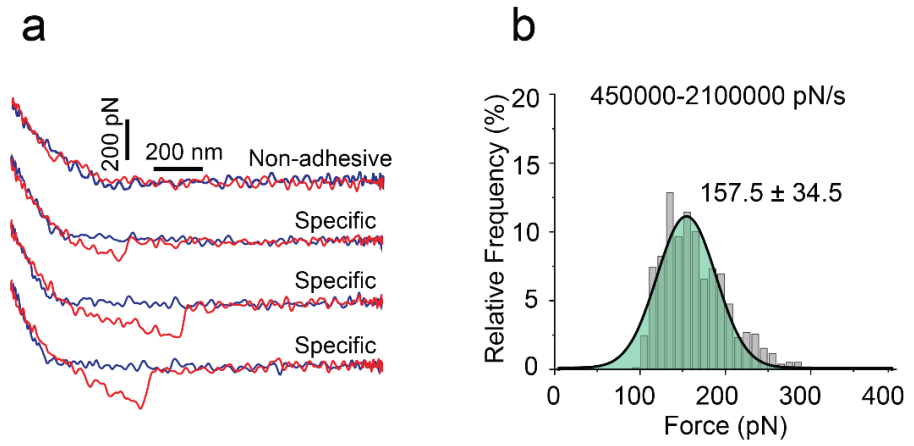

Figure 3.13: a Representative FD curves recorded on HEK293T-DC-SIGNR-GFP cell showing non-adhesion and specific adhesion events. **b** Force was extracted from the FT curves recorded from the HEK 293T-DC-SIGNR-GFP cell, plotted as a histogram, and then fitted with multipeak Gaussian fits. n= 778 from three independent experiments.

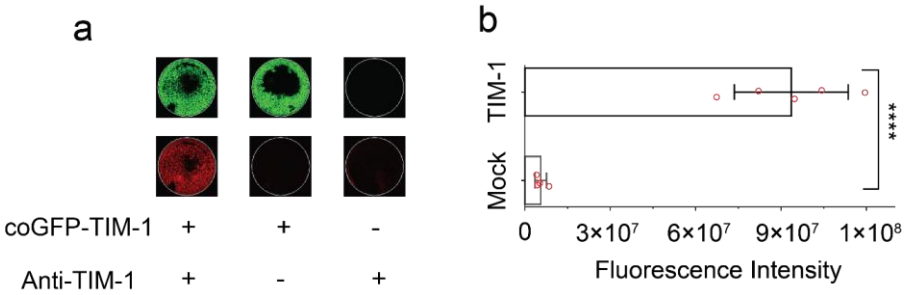

Figure 3.14: a Microplates were loaded with an identical number of cells per well. Using the in-cell western assay, signals from TIM-1-coGEP show as (green) and TIM-1 antibody (red) were obtained on HEK293T and transfected cells. **b** Quantification of the duplicate results in **a**. **** P< 0.0001, P values were determined by a two-sample t-test using Origin. Error bars indicate s.d. of mean.

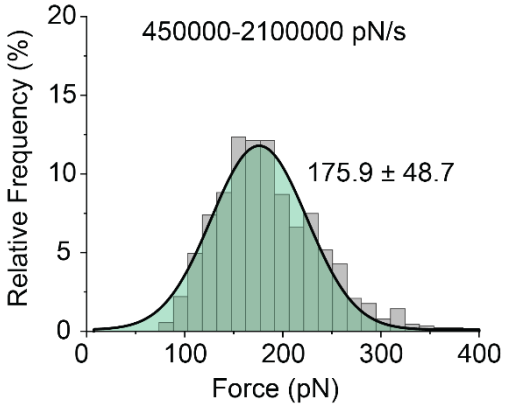

Figure 3.15: Force was extracted from the FT curves recorded from the HEK 293T-TIM-1-coGFP cell and plotted as a histogram, and then fitted with multipeak Gaussian fits. n= 908 from three independent experiments.

Similarly, we evaluated the binding of EBOV-VLPs to TIM-1 in the cellular context by transiently transfecting HEK-293T with TIM-1-GFP, and we evaluated its functional expression (**Figure 3.14a, b**). FD-based AFM using AFM tip derivatized with the EBOV-VLPs revealed that most adhesion events are localized on the transfected cells (**Figure 3.11d, e**). Analysis of the rupture force (**Figure 3.15**) and comparison with the data extracted on purified TIM-1 (**Figure 3.11f**) confirmed that EBOV binds to TIM-1 within a short contact time with the cell surface. The live cell data set clearly shows that EBOV has the ability to rapidly engage with the DC-SIGNR and the TIM-1 receptors immediately after landing on the cell surface, confirming that these two receptors play an important role in infection.

3.4 Discussion

EBOV entry requires the concerted action of multiple membrane receptors in the host, including two types of receptors, namely C-type lectin receptors and PS receptors (*34*). After binding to the cell surface, EBOV is internalized into the endosomes through the macropinocytosis pathway (*35*). Subsequently, the GP is cleaved to trigger the membrane fusion at the endosomes (*36,37*). Among PS receptors, the role of TIM-1 remains elusive and is controversially discussed in the literature. A recent study highlights a role for TIM-1 in PS binding during the cellular attachment, allowing it to better resist external mechanical perturbations (*26*), whereas another study suggests that TIM-1 serves as a receptor via a direct interaction with EBOV-GP (*13*).

Using single-virus force spectroscopy, we investigated EBOV binding to both DC-SIGNR and TIM-1 by quantifying the binding strength to each receptor in vitro on model surfaces and on living cells, mimicking physiologically relevant conditions. We demonstrated that both DC-SIGNR and TIM-1 are specific receptors for EBOV early binding to cellular surfaces. The kinetic and thermodynamic investigations pointed out that EBOV-GP specifically binds to DC-SIGNR/TIM-1 with remarkable high affinity (K_D in the nM range, **Figure 3.16**). Similar experiments conducted with the purified GP leads to the same conclusion, undoubtedly confirming a direct interaction.

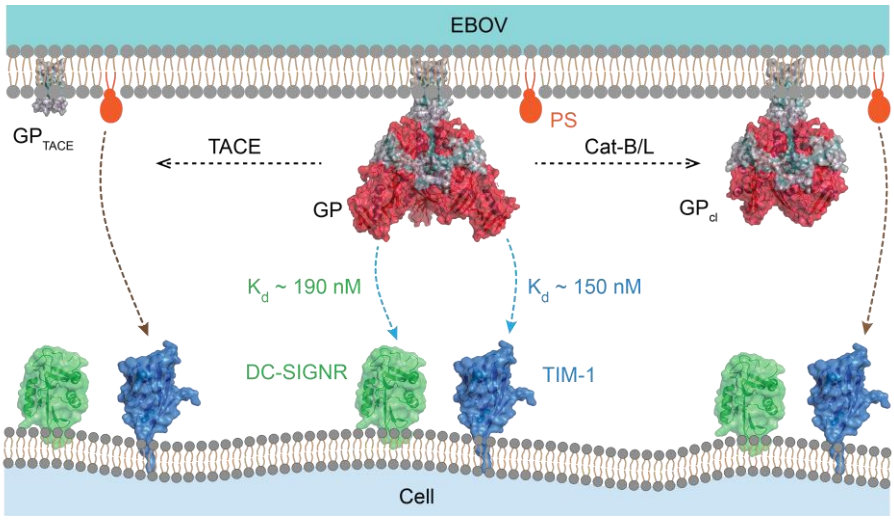

Figure 3.16: Multiple receptors mediate EBOV binding to host cells with high affinity. Models of EBOV binding to receptors: GP mediates EBOV high-affinity binding to DC-SIGNR and TIM-1. Binding to PS is sterically hindered during the early binding step.

For the first time, we studied at the single virion-level, how enzymes trigger change at the virion surface and how it influences binding properties to cell surface receptors. After EBOV attachment to the cell surface, the viral particles can be cleaved by Cat-B/L and/or TACE. We used AFM to understand how virus binding properties are modified upon enzymes processing. After GP cleavage in the membrane-proximal external region by TACE, we observed that EBOV-VLP still binds to TIM-1. This binding can be impeded by the injection of Annexin-V, suggesting that TIM-1 binding to PS is promoted after enzymatic cleavage. Binding of TIM-1 to PS is also observed after cleavage by Cat-B/L under low-pH conditions with a slightly lower frequency compared to TACE treatment (**Figure 3.5e**). Together, these results strikingly demonstrate that TIM-1 acts as a dual-receptor to both EBOV-GP and PS with the latter being favored after enzymatic cleavage within the endosomes (*17*).

Findings reported here elucidate the complex interplay between

EBOV and its cellular receptors prior to viral entry. Binding of EBOV-GP to TIM-1 and DC-SIGNR serves as the initial high-affinity binding just before the cellular entry. Then, under the action of Cat-B/L and TACE enzymes during endocytosis EBOV-GP is partially cleaved and the TIM-1 receptors present will be able to bind specifically to the PS, thus promoting the membrane fusion step (**Figure 3.16**). This two-step entry mechanism, orchestrated by a single cellular receptor, demonstrates the complexity and elegance of the EBOV infection mechanism. This important result points directly to the key role of the TIM-1 receptor making it an ideal candidate for the development of targeted antiviral molecules.

3.5 Mehods

HEK 293T cell lines and transfection.

HEK 293T cells were cultured in DMEM medium supplemented with 10% fetal bovine serum, penicillin (100 U mL^{-1}), and streptomycin (100 μg mL^{-1}) (Gibco). HEK 293T cells were maintained in a humidified incubator with 5% CO_2 at 37°C. pCMV-DC-SIGNR-GFP (Sino Biological) and pCDH-TIM-1-coGFP were transfected with Lipofectamine LTX (Invitrogen) according to the manufacturer's protocol. In brief, 200,000 cells were seeded in a cell culture plate (40 mm). The cells were transfected with either 2.5 μg pCMV-DC-SIGNR-GFP or pCDH-TIM-1-coGFP using 2.5 μL Plus reagent and 10 μL Lipofectamine LTX (Invitrogen), respectively. After 24-48 h of transfection, cells were used for AFM analysis.

Production and characterization of recombinant EBOV-VLPs.

Virus stocks were generated in HEK 293T cells as described previously (*22*). Briefly, 6 μg pcDNA3.1(+)-GP and 12 μg pcDNA3.1(+)-VP40-mCherry (wild-type gene of 1976 Zaire Ebola virus strain) were co-transfected into HEK 293T cells using Lipofectamine LTX in a T-75 flask. After 48-72 h of transfection, the supernatant containing the EBOV-VLPs was collected by removal of the cell debris in 1,000 g for 10 min. The supernatant was ultracentrifuged through a 20% sucrose buffer at 25,000 rpm in a Ti 70 rotor for 2.5 h at 4°C. The resulting pellet was resuspended in 200 μL of ice-cold phosphate-buffered saline (PBS, Thermo Fisher Scientific) and then dialyzed using MINI Dialysis Devices (10K MWCO, Thermo Fisher Scientific) at 4 °C without exposure to light overnight. The EBOV-VLPs (10 μL) was adsorbed onto the glass slide coated with Ploy-L-

Lysine (1%) for 20 min and dried at air. The image of the EBOV-VLPs was taken by AFM (Bruker). EBOV-VLPs (10 µL) was dropped onto the glass slide to verify the EBOV-VLPs with the fluorescence using a laser scanning confocal microscope (LSM-980, Zeiss).

Functionalization of AFM tips.

EBOV-VLPs were grafted onto AFM tips apex (MSCT and PFQNM-LC cantilevers, Bruker), using following protocol (*38*): the AFM tips were washed in chloroform (3 x 10 min), cleaned in a UV radiation and ozone (UV-O) cleaner (Jetlight). The tips were further incubated for 2 h in an argon-filled desiccator with 30 µL APTES and 10 µL triethylamine. To cure the APTES coating, the tips were maintained under argon for 2 days after removing APTES and triethylamine. To ensure a low density of the EBOV-VLP on the AFM tip, NHS-PEG_{24}-Ph-Aldehyde (Broadpharm) was grafted on the amino-functionalized tips. NHS-PEG_{24}-Ph-aldehyde (3.3 mg) was dissolved in chloroform (0.5 mL) and trimethylamine (30 µL). The cantilevers were immersed in the solution for 2 hours and washed 3 times with chloroform and dried with nitrogen. The cantilevers were immersed in the EBOV-VLPs solution (100 µL) that contains 2 µL fresh $NaCNBH_3$ (6 wt% vol^{-1} in 0.1 M NaOH(aq)) on ice for 1 h. Finally, 5 µl of 1 M ethanolamine solution was added into the EBOV-VLPs solution and incubated for 10 min to quench the reaction. The cantilevers were washed 5 times with PBS buffer. The cantilevers were not dried during the functionalization steps. The functionalized cantilevers were used on the day of functionalization. The cantilever showed no more than one viral particle at the apex of the AFM tips. GP (R&D Systems) was grafted onto AFM tips apex according to the same protocol as that used for EBOV-VLPs.

Preparation of DC-SIGNR/TIM-1 model surfaces.

Gold-coated surfaces were cleaned for 15 min using UV-O cleaner and subsequently immersed overnight in an ethanol solution containing 1% 1 mM 16-mercaptododecahexanoic acid and 99% 11-mercapto-1-undecanol. Surfaces were rinsed with ethanol, dried with N_2, and added to a milliQ water solution containing equal volumes of 20 mg mL^{-1} N-hydroxysuccinimide (NHS) and 50 mg mL^{-1} 1-ethyl-3-(3-dimethylaminopropyl)-carbodiimide (EDC) for 30 min. Surfaces were then rinsed with milliQ water and incubated for 1 h with 40 µL of DC-SIGNR or TIM-1 (10 µg mL^{-1} in PBS, R&D Systems). Finally, surfaces were washed 5 times with PBS and used in experiments on the day of the preparation. The surface showed a stable and homogenous thickness of ~1.5 nm and 2 nm for DC-SIGNR and TIM-1, respectively (**Figure 3.2**).

FD curved-based AFM on model surfaces.

FD curved-based AFM on model surfaces was conducted in PBS buffer using AFM (Nanoscope Multimode 8, Bruker) at room temperature. EBOV-VLPs functionalized MSCT-D cantilever were used to record force curves from 10 × 10 µm model surface areas in the force-volume (contact) mode (Nanoscope software v9.2). The spring constants of the cantilevers were calibrated using the thermal noise method (*39*).

To extract k_{off} and χ_β, the dynamic force spectroscopy (DFS) experiments were performed using set point of 500 pN, with a resolution of 32 × 32 pixels, and 1 µm s^{-1} approach velocity. The various retraction velocities (0.1, 0.2, 1, 5, 10 to 20 µm s^{-1}) were used to probe the rupture force over a wide range of LRs. The pulling velocity (v) and loading rate (LR) are defined as a function of k_{eff} (the effective spring constant of the system): $LR = \Delta F/\Delta t = k_{eff} v$, where $\Delta F/\Delta t$ is the applied force over time. To

ensure higher binding probability, the hold time was set to 200 ms. LRs and rupture forces were extracted using Nanoscope analysis (v2.0, Bruker). Origin software (OriginLab) was used to display the results as DFS plots to fit histograms of rupture force distributions for distinct LR ranges and to apply various force spectroscopy models to extract the number of bonds mediating interaction between substrate and ligand, k_{off}, and χ_{β}, as described (33, 39).

For kinetic k_{on} analysis, the BP was determined from rate of curves showing binding events at a certain hold time (the time the tip is on the surface delay). When other parameters were kept constant (approach/reverse velocity: 1 µm s^{-1}, ramp size: 500 nm, set point force: 500 pN, line frequency: 1 Hz, and pixels per line: 32), the BP was measured with different hold times (0, 50, 100, 200, 350, 500, 800, and 1100 ms). These data were fitted as described previously (29,30). In brief, assuming the binding events follows pseudo first order kinetics, the kinetic k_{on} is described by the following equation:

$$k_{on} = (c_{eff}\tau_i)^{-1} = (\frac{n}{V_{eff}}\tau_i)^{-1}$$

where c_{eff} is the effective concentration of free partners available for interaction at equilibrium and can be calculated from the number of binding partners (n) over the effective volume (V_{eff}) (a sphere with radius equal to the equilibrium length of the PEG linker and the size of the virus) accessible for free equilibrium interaction between the EBOV-VLP and receptors. The interaction time (τ_i) is extracted by fitting the BF over hold time (t) with the following equation:

$$BP = A\left(1 - \exp\left(\frac{-(t - t_0)}{\tau_i}\right)\right)$$

Where A is the maximum BP and t_0 is the lag time. K_D further was

calculated subsequently as k_{off}/k_{on}.

FD curve-based AFM and fluorescence microscopy on living cells.

A Bioscope Resolve (Bruker) coupled to an inverted optical microscope (Zeiss, 40x oil objective) was used to map a confluent layer of HEK 293T cells with PeakForce QNM mode (Nanoscope software v9.2). HEK 293T cells were retained under cell-culture conditions (with growth medium, 5% CO_2, and 37°C). HEK 293T cells were imaged by PFQNM-LC probes (Bruker, the sensitivity was calibrated by fixing the nominal spring constant of pre-calibrated cantilevers with "no-touch" calibration) at 25 × 25 μm areas containing 2-3 adjacent cells. AFM tip was oscillated in a sinusoidal manner, with an amplitude of 750 nm, a frequency of 0.25 kHz, and about the force setpoint of 500 pN. The sample was scanned with a frequency of 0.125 Hz and a resolution of 256 × 256 pixels, of which 65536 FD curves were obtained in each image. Image and FD curves were further processed and analyzed using Nanoscope analysis, Origin, ImageJ, Zen Blue 3.1 (Zeiss) software.

In-Cell Western Assay.

HEK 293T cells were plated in sterile black-walled 96 plates at an identical density. The cells were grown and transfected as indicated above. After 48 h of transfection, In-Cell Westerns (ICW) analysis was performed according to the manufacturer's protocol. In brief, all wells were carefully washed with PBS and fixed immediately by adding a final concentration of 3.7% formaldehyde at 4°C for 20 min. After fixation, the plates were washed with PBS (3 × 10 min) and then blocked using 1% BSA for 1 h. The plates were incubated with primary antibodies (1:50, R&D Systems) at 4°C using 2 h and then incubated with secondary antibodies (1:250, IRshort550 conjugates of mouse-anti-IgG for DC-SIGNR, Sigma, and Cy3

conjugates of goat-anti-IgG for TIM-1, Abcam) at 4°C using for 1 h. Plates were scanned and analyzed using Typhoon (ImageQuantTL software). Scan settings were with 50 μm resolution. For signal quantification, signals of fluorescence fused protein and antibody were analyzed from the average fluorescence intensity for the corresponding channel.

In vitro protease treatments and western blotting.

The EBOV-VLP functionalized AFM tips were treated with 4 μg ml^{-1} CatB and CatL (4 μg ml^{-1}, Sino Biological) at pH 4.5 in MES buffer (25 mM morpholineethanesulfonic acid, 5 mM DTT) or with TACE (4 μg ml^{-1}) at pH 9 in the Tris buffer (50 mM Tris) for 40 min at room temperature. Mock treatment was conducted without enzyme. For checking the enzymes are working, the purified GP was treated in identical conditions, and then resolved by SDS-polyacrylamide gel electrophoresis (4-20% polyacrylamide gel, Eurogentec) and subsequently transferred onto a Nitrocellulose membrane (Cytiva). The membrane was blocked with 0.5% BSA in TBS solution with 0.1% tween-20 for 1 h, and incubated with 0.5 μg ml^{-1} primary antibody of GP (R&D Systems) overnight at 4°C, and incubated with secondary antibody (1:1000, Agilent) for mouse source GP. Then, the membrane was imaged by Amersham Imager 600 (Cytiva).

ACKNOWLEDGEMENTS

This work was supported by the Université catholique de Louvain and the Fonds National de la Recherche Scientifique (FRS-FNRS). This project received funding from the European Research Council under the European Union's Horizon 2020 research and innovation program (grant agreement no. 758224) and from the FNRS-Welbio (Grant # CR-2019S-01). The funders had no role in study design, data collection and analysis,

decision to publish, or preparation of the manuscript. S.P., M.K. and D. A. are research fellow, postdoctoral researcher and research associate at the FNRS, respectively. Q.Z. and D.A. are grateful to China Scholarship Council.

3.6 Reference

1. Jacob, S. T.; Crozier, I.; Fischer, W. A.; Hewlett, A.; Kraft, C. S.; Vega, M.-A. de L.; Soka, M. J.; Wahl, V.; Griffiths, A.; Bollinger, L.; Kuhn, J. H. Ebola Virus Disease. *Nat. Rev. Dis. Primers* **2020**, *6* (1), 13.

2. Feldmann, H.; Geisbert, T. W. Ebola Haemorrhagic Fever. *The Lancet* **2011**, *377* (9768), 849–862.

3. Hoenen, T.; Groseth, A.; Feldmann, H. Therapeutic Strategies to Target the Ebola Virus Life Cycle. *Nat. Rev. Microbiol.* **2019**, *17* (10), 593–606.

4. Choi, J. H.; Croyle, M. A. Emerging Targets and Novel Approaches to Ebola Virus Prophylaxis and Treatment. *BioDrugs* **2013**, *27* (6), 565–583.

5. Adu-Gyamfi, E.; Johnson, K. A.; Fraser, M. E.; Scott, J. L.; Soni, S. P.; Jones, K. R.; Digman, M. A.; Gratton, E.; Tessier, C. R.; Stahelin, R. V. Host Cell Plasma Membrane Phosphatidylserine Regulates the Assembly and Budding of Ebola Virus. *J. Virol.* 2015, *89*, 9440–9453.

6. Lee, J. E.; Saphire, E. O. Ebolavirus Glycoprotein Structure and Mechanism of Entry. *Future Virol.* **2009**, *4* (6), 621–635.

7. Martines, R. B.; Ng, D. L.; Greer, P. W.; Rollin, P. E.; Zaki, S. R. Tissue and Cellular Tropism, Pathology and Pathogenesis of Ebola and Marburg Viruses. *J. Pathol.* **2015**, *235* (2), 153–174.

8. Bhattacharyya, S.; Hope, T. J. Cellular Factors Implicated in Filovirus Entry. *Adv. Virol.* **2013**, *2013*, 487585.

9. Takada, A. Filovirus Tropism: Cellular Molecules for Viral Entry. *Frontiers in Microbiology* **2012**, *3*, 34.

10. Moller-Tank, S.; Maury, W. Ebola Virus Entry: A Curious and Complex Series of Events. *PLoS Pathog.* **2015**, *11* (4), e1004731.

11. Moller-Tank Sven; Kondratowicz Andrew S.; Davey Robert A.; Rennert Paul D.; Maury Wendy. Role of the Phosphatidylserine Receptor TIM-1 in Enveloped-Virus Entry. *J. Virol.* **2013**, *87* (15), 8327–8341.

12. Jemielity, S.; Wang, J. J.; Chan, Y. K.; Ahmed, A. A.; Li, W.; Monahan, S.; Bu, X.; Farzan, M.; Freeman, G. J.; Umetsu, D. T.; DeKruyff, R. H.; Choe, H. TIM-Family Proteins Promote Infection of Multiple

Enveloped Viruses through Virion-Associated Phosphatidylserine. *PLoS Pathog.* **2013**, *9* (3), e1003232.

13. Kondratowicz, A. S.; Lennemann, N. J.; Sinn, P. L.; Davey, R. A.; Hunt, C. L.; Moller-Tank, S.; Meyerholz, D. K.; Rennert, P.; Mullins, R. F.; Brindley, M.; Sandersfeld, L. M.; Quinn, K.; Weller, M.; McCray, P. B.; Chiorini, J.; Maury, W. T-Cell Immunoglobulin and Mucin Domain 1 (TIM-1) Is a Receptor for Zaire Ebolavirus and Lake Victoria Marburgvirus. *Proc. Natl. Acad. Sci. U. S. A.* 2011, *108*, 8426–8431.

14. Simmons, G.; Reeves, J. D.; Grogan, C. C.; Vandenberghe, L. H.; Baribaud, F.; Whitbeck, J. C.; Burke, E.; Buchmeier, M. J.; Soilleux, E. J.; Riley, J. L.; Doms, R. W.; Bates, P.; Pöhlmann, S. DC-SIGN and DC-SIGNR Bind Ebola Glycoproteins and Enhance Infection of Macrophages and Endothelial Cells. *Virology* **2003**, *305* (1), 115–123.

15. Alvarez, C. P.; Lasala, F.; Carrillo, J.; Muñiz, O.; Corbí, A. L.; Delgado, R. C-Type Lectins DC-SIGN and L-SIGN Mediate Cellular Entry by Ebola Virus in Cis and in Trans. *J. Virol.* 2002, *76*, 6841–6844.

16. Schornberg, K.; Matsuyama, S.; Kabsch, K.; Delos, S.; Bouton, A.; White, J. Role of Endosomal Cathepsins in Entry Mediated by the Ebola Virus Glycoprotein. *J. Virol.* **2006**, *80* (8), 4174.

17. Chandran, K.; Sullivan, N. J.; Felbor, U.; Whelan, S. P.; Cunningham, J. M. Endosomal Proteolysis of the Ebola Virus Glycoprotein Is Necessary for Infection. *Science* **2005**, *308* (5728), 1643.

18. Côté, M.; Misasi, J.; Ren, T.; Bruchez, A.; Lee, K.; Filone, C. M.; Hensley, L.; Li, Q.; Ory, D.; Chandran, K.; Cunningham, J. Small Molecule Inhibitors Reveal Niemann–Pick C1 Is Essential for Ebola Virus Infection. *Nature* **2011**, *477* (7364), 344–348.

19. Dolnik, O.; Volchkova, V.; Garten, W.; Carbonnelle, C.; Becker, S.; Kahnt, J.; Ströher, U.; Klenk, H.-D.; Volchkov, V. Ectodomain Shedding of the Glycoprotein GP of Ebola Virus. *EMBO J.* **2004**, *23* (10), 2175–2184.

20. Cook, J. D.; Lee, J. E. The Secret Life of Viral Entry Glycoproteins: Moonlighting in Immune Evasion. *PLoS Pathog.* **2013**, *9* (5), e1003258.

21. Müller, D. J.; Dumitru, A. C.; Lo Giudice, C.; Gaub, H. E.; Hinterdorfer, P.; Hummer, G.; De Yoreo, J. J.; Dufrêne, Y. F.; Alsteens, D. Atomic Force Microscopy-Based Force Spectroscopy and Multiparametric Imaging of Biomolecular and Cellular Systems. *Chem. Rev.* **2021**, *121* (19), 11701–11725.

22. Zhang, Q.; Tian, F.; Wang, F.; Guo, Z.; Cai, M.; Xu, H.; Wang, H.; Yang, G.; Shi, X.; Shan, Y.; Cui, Z. Entry Dynamics of Single Ebola Virus Revealed by Force Tracing. *ACS Nano* **2020**, *14* (6), 7046–7054.

23. Yuan, S.; Cao, L.; Ling, H.; Dang, M.; Sun, Y.; Zhang, X.; Chen, Y.; Zhang, L.; Su, D.; Wang, X.; Rao, Z. TIM-1 Acts a Dual-Attachment Receptor for Ebolavirus by Interacting Directly with Viral GP and the PS on the Viral Envelope. *Protein & Cell* **2015**, *6* (11), 814–824.

24. Evans, E. A.; Calderwood, D. A. Forces and Bond Dynamics in Cell Adhesion. *Science*, 2007, *316*, 1148–1153.

25. Evans, E.; Ritchie, K. Dynamic Strength of Molecular Adhesion Bonds. *Biophys. J.* **1997**, *72* (4), 1541–1555.

26. Dragovich, M. A.; Fortoul, N.; Jagota, A.; Zhang, W.; Schutt, K.; Xu, Y.; Sanabria, M.; Moyer, D. M.; Moller-Tank, S.; Maury, W.; Zhang, X. F. Biomechanical Characterization of TIM Protein–Mediated Ebola Virus–Host Cell Adhesion. *Sci. Rep.* **2019**, *9* (1), 267.

27. Evans, E.; Williams, P. Dynamic Force Spectroscopy. Springer Berlin Heidelberg: Berlin, Heidelberg, **2002**, 145–204.

28. Williams, P. M. Analytical Descriptions of Dynamic Force Spectroscopy: Behaviour of Multiple Connections. Anal. Chim. Acta **2003**, *479* (1), 107–115.

29. Rankl, C.; Kienberger, F.; Wildling, L.; Wruss, J.; Gruber, H. J.; Blaas, D.; Hinterdorfer, P. Multiple Receptors Involved in Human Rhinovirus Attachment to Live Cells. *Proc. Natl. Acad. Sci. U. S. A.* **2008**, *105* (46), 17778.

30. Baumgartner, W.; Gruber, H. J.; Hinterdorfer, P.; Drenckhahn, D. Affinity of Trans-Interacting VE-Cadherin Determined by Atomic Force Microscopy. *Single Molecules* **2000**, *1* (2), 119–122.

31. Gramberg, T.; Soilleux, E.; Fisch, T.; Lalor, P. F.; Hofmann, H.; Wheeldon, S.; Cotterill, A.; Wegele, A.; Winkler, T.; Adams, D. H.; Pöhlmann, S. Interactions of LSECtin and DC-SIGN/DC-SIGNR with Viral Ligands: Differential PH Dependence, Internalization and Virion Binding. *Virology* **2008**, *373* (1), 189–201.

32. Kuroda, M.; Fujikura, D.; Nanbo, A.; Marzi, A.; Noyori, O.; Kajihara, M.; Maruyama, J.; Matsuno, K.; Miyamoto, H.; Yoshida, R.; Feldmann, H.; Takada, A. Interaction between TIM-1 and NPC1 Is Important for Cellular Entry of Ebola Virus. *J. Virol.* **2015**, *89* (12), 6481–6493.

33. Alsteens, D.; Newton, R.; Schubert, R.; Martinez-Martin, D.; Delguste, M.; Roska, B.; Müller, D. J. Nanomechanical Mapping of First Binding Steps of a Virus to Animal Cells. *Nat. Nanotechnol.* **2017**, *12* (2), 177–183.

34. Rasmussen, A. L. Host Factors in Ebola Infection. *Annu. Rev. Genom. Hum. Genet.* **2016**, *17* (1), 333–351.

35. Nanbo, A.; Imai, M.; Watanabe, S.; Noda, T.; Takahashi, K.; Neumann, G.; Halfmann, P.; Kawaoka, Y. Ebolavirus Is Internalized into Host Cells via Macropinocytosis in a Viral Glycoprotein-Dependent Manner. *PLoS Pathog.* **2010**, *6* (9), e1001121.

36. Wang, H.; Shi, Y.; Song, J.; Qi, J.; Lu, G.; Yan, J.; Gao, G. F. Ebola Viral Glycoprotein Bound to Its Endosomal Receptor Niemann-Pick C1. *Cell* **2016**, *164* (1), 258–268.

37. Carette, J. E.; Raaben, M.; Wong, A. C.; Herbert, A. S.; Obernosterer, G.; Mulherkar, N.; Kuehne, A. I.; Kranzusch, P. J.; Griffin, A. M.; Ruthel, G.; Cin, P. D.; Dye, J. M.; Whelan, S. P.; Chandran, K.; Brummelkamp, T. R. Ebola Virus Entry Requires the Cholesterol Transporter Niemann–Pick C1. *Nature* **2011**, *477* (7364), 340–343.

38. Wildling, L.; Unterauer, B.; Zhu, R.; Rupprecht, A.; Haselgrübler, T.; Rankl, C.; Ebner, A.; Vater, D.; Pollheimer, P.; Pohl, E. E.; Hinterdorfer, P.; Gruber, H. J. Linking of Sensor Molecules with Amino Groups to Amino-Functionalized AFM Tips. *Bioconjugate Chem.* **2011**, *22* (6), 1239–1248.

39. Newton, R.; Delguste, M.; Koehler, M.; Dumitru, A. C.; Laskowski, P. R.; Müller, D. J.; Alsteens, D. Combining Confocal and Atomic Force Microscopy to Quantify Single-Virus Binding to Mammalian Cell Surfaces. *Nature Protocols* **2017**, *12* (11), 2275–2292.

Chapter 4:

Probing SARS-CoV-2 Fusion Domain-Membrane Interaction via Single-Molecule AFM-based Force Spectroscopy

Qingrong Zhang[1], Gol Mohammad Dorrazehi[1], Ankita Ray[1], Kimberly Durlet and David Alsteens[1,2,*]

[1]Louvain Institute of Biomolecular Science and Technology, Université catholique de Louvain, Croix du sud 4-5, L7.07.07, 1348 Louvain-la-Neuve, Belgium 1348

[2]WELBIO department, WEL Research Institute, Avenue Pasteur, 6, Wavre, Belgium 1300

*Correspondence should be addressed to (D.A.): david.alsteens@uclouvain.be

Author contributions

D.A., **Q.Z.**, and G.M.D conceived the project. **Q.Z** conducted all experiments. A.R take part in analyzing BLI data. K. D product the pseudotyped SARS-CoV-2 virus. All authors wrote the manuscript.

Preparing to submit it for publication

Keywords: Fusion peptide, Binding, Cholesterol, Lipid vesicles, TMPRSS2, SARS-CoV-2 inhibition, Atomic force microscopy, Biolayer interferometry

4.1 Abstract

Membrane fusion between SARS-CoV-2 envelope and target cells is a critical step in infection. Understanding the molecular mechanisms behind this fusion process is crucial. In this study, we investigated the interaction between the fusion peptide (FP) of SARS-CoV-2 spike protein and the host membrane. We utilized biolayer interferometry and atomic force microscopy-based single-molecule force spectroscopy for kinetics and thermodynamics analysis. Our findings revealed that cholesterol plays a significant role in enhancing the binding affinity of both SARS-CoV-2 FP to the lipid membrane. Under physiologically relevant conditions, we demonstrated how the presence of cholesterol can facilitate the binding between TMPRSS2-cleaved S2 subunit and the membrane. Notably, we have observed that the presence of the disulfide bond within the FP augments the stability of the FP-membrane complex. This enhanced stability is likely attributed to the greater mechanical resilience inherent in the FP domain. Moreover, cholesterol depletion from the host membrane effectively inhibited SARS-CoV-2 infectivity, as demonstrated by the pseudovirus-based infection assay. Our results highlight the cooperative influence of membrane composition and peptide structure on the binding of SARS-CoV-2 FP to the host membrane. These findings have tremendous importance in the development of broadly effective vaccines and therapies against SARS-CoV-2.

4.2 Introduction

Coronavirus disease 2019 (COVID-19) is a global pandemic and a serious public health threat caused by a novel virus called severe acute respiratory syndrome coronavirus 2 (SARS-CoV-2). SARS-CoV-2 belongs to the coronavirus family and is an enveloped positive-stranded RNA virus (*1*). The surface of SARS-CoV-2 is decorated with the glycosylated homotrimer Spike (S) protein, which plays a crucial role in binding and fusion with the host cell membrane. The S protein is divided into two functional subunits, S1 and S2, through cleavage by the host protease furin in the Golgi apparatus during viral maturation (*2-4*). S1 is responsible for binding to the host cell receptor, angiotensin-converting enzyme 2 (ACE2), while S2 facilitates membrane fusion (*5-7*). Upon binding of the receptor-binding domain (RBD) present in the S1 subunit to ACE2, the S2' site in S2 subunit undergoes processing by the transmembrane protease serine 2 (TMPRSS2), leading to the shedding of S1 and exposure of the fusion peptide (FP) (8). Subsequently, the S2 subunit undergoes conformational changes, extending to facilitate FP binding to the host cell membrane. Finally, irreversible refolding of the S2 subunit brings the viral and host cellular membranes in close spatial proximity, facilitating the delivery of the viral genetic cargo (**Figure 4.1a**) (*9, 10*).

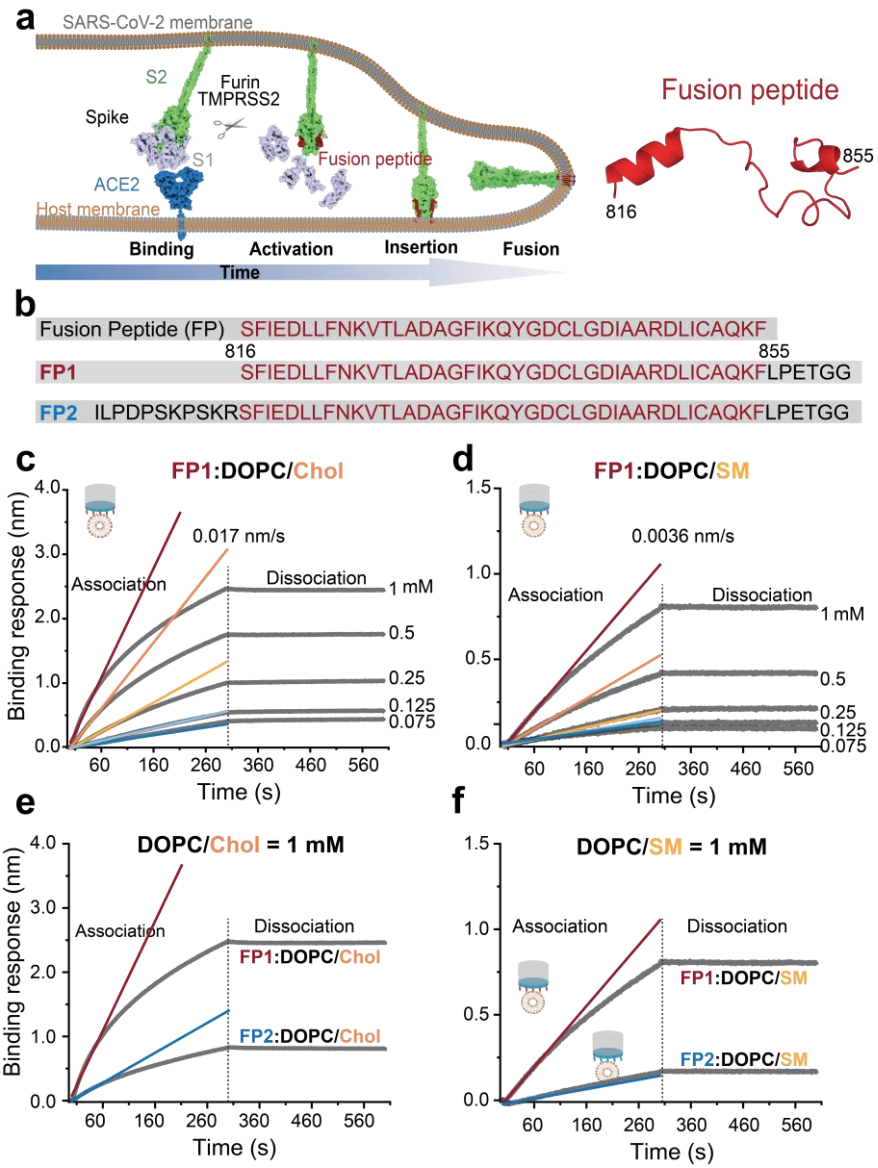

Figure 4.1: SARS-CoV-2 FP interaction with lipid vesicles. (**a**) Cartoon illustrating the interaction between SARS-CoV-2 and the host membrane. The S protein binds to the host cell surface via ACE2 receptor, and upon host protease activation, the S1 subunit detaches, exposing the FP. The SARS-CoV-2 FP then binds to the host membrane, followed by refolding of S2 into a post-fusion state, leading to the membrane fusion between viral and target cells. The representative structure of SARS-CoV-2 FP (PDB ID 6XR8) is shown from the prefusion conformation of the trimeric SARS-CoV-2 S protein (right). (**b**) The FP region

of SARS-CoV-2 spans amino-acid residues 816-855 of the S protein sequence. FP1 is tagged with LPETGG at the C-terminus, and FP2 is an extended sequence expanding by 11 amino acids at its N-terminus. (**c** and **d**) Measurement of the binding affinity between SARS-CoV-2 FP and the lipid vesicles consisting of DOPC and Chol (**c**) or DOPC and SM (**d**) using biolayer interferometry. Grey lines represent the raw data, while colored lines represent the binding rate of the association phase, which is the linear fit within the preliminary 60s of the association phases. (**e** and **f)** Measurement of the interaction between the FP1 or FP2 and the lipid vesicles using biolayer interferometry. 10 μM FP1 or FP2 were loaded onto AR2Gbiosensors and were then allowed to interact with the 1 mM Chol/DOPC vesicle **(e**) or SM/DOPC vesicle (**f**), respectively.

Due to the crucial role of the S1 subunit in receptor recognition, current SARS-CoV-2 vaccines and therapies primarily target the S1 domain of the S protein (*11-14*). However, an alternative approach is to focus on the S2 subunit, which is more genetically conserved across coronaviruses (*15-18*). The SARS-CoV-2 FP, consisting of 40 amino acids (residues 816-855 of the S protein sequence), contains a fully conserved internal disulfide bond (Cys840 and Cys851) (*19-21*). Targeting this domain and process of membrane fusion holds promise in addressing emerging SARS-CoV-2 variants and mitigating potential future coronavirus outbreaks. Therefore, gaining a comprehensive understanding of the molecular mechanisms underlying SARS-CoV-2 FP-induced membrane fusion is crucial for advancing our knowledge of coronavirus infection and facilitating the design of effective vaccines and therapies. Recent studies have demonstrated the broad efficacy of lipopeptides targeting the conserved membrane fusion process and monoclonal antibodies recognizing the conserved FP motif in combating coronavirus infection (*22-24*).

Membrane fusion is an energetically favorable process, but it faces high kinetic barriers due to repulsive hydration forces between bilayers

(*25*). Notably, the height of this fusion barrier varies substantially depending on the composition of the membranes (*18, 26*). In the case of SARS-CoV-2, the energy needed to overcome the barrier between the virus and the host cell membrane arises from an irreversible conformational transition in the S2 subunit. This transition converts S2 from a less stable pre-fusion state to a more stable post-fusion state (*9, 10*), and it relies on the binding stabilization of FP region to the membrane. The internal disulfide bond in the FP most presumably aids in stabilizing its structure during binding. Furthermore, there is increasing evidence that the lipid composition of viral and cellular membranes (*27, 28*), as well as the depletion of cholesterol (Chol), impact SARS-CoV-2 membrane fusion and infection (*29*). However, formal evidence regarding how the internal disulfide bond of the FP region and lipid composition contribute to FP binding to the host membrane is still lacking.

Atomic force microscopy-based single-molecule force spectroscopy (AFM-based SMFS) has recently emerged as a nanoscopic tool for monitoring membrane protein unfolding, folding, and insertion with piconewton-scale resolution and at the single-molecule level. By moving the AFM tip away from the sample with a certain height, the molecule of interest is stretched or escaped from a membrane. These molecules have a probability of refolding or reinserting themselves into the membrane. The force and time of refolding or insertion of the membrane protein are recorded by tracking the deflection of the AFM cantilever. This technique is very well suited to monitor the interaction of fusion peptides and membranes.

In this study, we shed light on the impact of the internal disulfide bond within the FP region and the lipid composition on the binding of SARS-

CoV-2 FP to the host membrane at the single-peptide level. Through the utilization of biolayer interferometry (BLI) assays, we assessed the influence of membrane composition on the interaction between SARS-CoV-2 FP and the membrane. Moreover, we directly observed the binding of FP to biomimetic lipid membrane at the single-peptide level using atomic force microscopy (AFM)-based single-molecule force spectroscopy (SMFS), enabling the extraction of kinetics and thermodynamics data pertaining to this process. Additionally, our results demonstrated that the presence of the internal disulfide bond within the FP region, as well as Chol content in the membrane composition, played crucial roles in FP binding. Notably, the depletion of Chol effectively inhibited SARS-CoV-2 infection, underscoring the significance of the binding process of FP region to the membrane as a potential target for broadly effective therapies against coronaviruses.

4.3 Results

Cholesterol enhances FP binding to membrane

The functional FP of SARS-CoV-2 is a 40 amino acids sequence starting at Ser816 that is formed from the mature N-terminus of the S2' site, after priming by TMPRSS2 (*8, 30*). To probe the dynamics of the SARS-CoV-2 FP binding to the plasma membrane, we designed two peptides with slight modifications, FP1 and FP2 based on the primary FP sequence. FP1 is the LPETGG-tagged FP of SARS-CoV-2, allowing the protein to be ligated by sortase A at the C terminus, and FP2 represents the uncleaved version of FP, with additional 11 amino acid residues on the N-terminal side (**Figure 4.1b**). To assess the influence of lipid composition on FP domain binding, lipidic vesicles composed of 30% sphingomyelin (SM) or cholesterol (Chol) and 70% 1,2-dioleoyl-sn-glycero-3-phosphocholine (DOPC) were used, mimicking the components of cell membranes (*31, 32*).

To assess the impact of Chol on the membrane-binding capacity of SARS-CoV-2 FP1, we conducted a biolayer interferometry (BLI) assay (*33*). The FPs were covalently attached to an amine reactive biosensor. Briefly, sensors bearing free carboxylic acid groups were activated by reaction with EDC (1-Ethyl-3-[3-dimethylaminopropyl] carbodiimide hydrochloride) and NHS (N-hydroxysulfosuccinimide) to generate highly reactive NHS esters. The esters rapidly react with the amine groups of FP1 or FP2, forming a highly stable amide bond. Subsequently, lipid vesicles containing 30% SM or Chol and 70% DOPC at concentrations of 0.075, 0.125, 0.25, 0.5, and 1 mM respectively were applied to associate and disassociate with the peptides. Our findings revealed a faster binding of FP1 with cholesterol-containing vesicles compared to sphingomyelin-

containing vesicles. Specifically, the binding velocity of FP1 to DOPC/Chol (70:30) vesicles (0.017 nm s^{-1}) was five times higher than to DOPC/SM (70:30) vesicles (0.0036 nm s^{-1}) during the association phase (**Figure 4.1c, d**). As control experiments, we also evaluated the membrane-binding response of SARS-CoV-2 FP2 to both Chol and SM vesicles. Interestingly, we observed a significantly lower membrane-binding response of FP2 compared to FP1 when exposed to vesicles at the same concentration (**Figure 4.1e, f**). These findings emphasize the significance of the N-terminus exposure at the S2' site during the membrane-binding of SARS-CoV-2 FP (*34*). Our overall results underscore Chol's crucial role in FP binding to the plasma membrane. It's worth noting that the grafting technique employed could potentially favor the N-terminus grafting due to its higher reactivity. To meticulously explore the N-terminus's involvement at S2', we proceeded to investigate this binding using AFM and an oriented coupling method.

Monitoring SARS-CoV-2 FP-binding at the single-molecule level

To account for potential influences arising from factors such as vesicle size, coupling of FP to the sensor and its accessibility for the vesicle, we performed an exhaustive analysis of these interactions at the single-molecule level by AFM, between oriented FP onto the tip and lipid bilayers. Supported lipid bilayers, with similar composition as the vesicles used for BLI experiments, were prepared to mimic the outer leaflet of cell membranes (*35*). To validate the lipid bilayers formation, AFM topography imaging was performed under physiological conditions which maintains their near native state of hydration. Height cross-section analysis revealed a height of approximately 4.74 ± 0.1 nm for both the DOPC/Chol and DOPC/SM systems (**Figure 4.2** and **Figure 4.4a**). The

integration of smaller cholesterol molecules or long-saturated acyl chain sphingomyelins (SMs) into the DOPC matrix resulted in a slightly increased bilayer thickness to approximately 4.84 ± 0.2 nm for DOPC/SM compared to DOPC/Chol. To reflect the physiologically relevant state of SARS-CoV-2 interaction with host cells, FPs were covalently attached in an oriented manner to the AFM cantilever tip using a flexible polyethylene glycol spacer (PEG_{24}) and the Sortase A enzyme (**Figure 4.3a**). This tethering approach ensures that the experimental setup accurately captures the movement of the exposed N terminus of the FP and faithfully represents the encounter between SARS-CoV-2 and host cells.

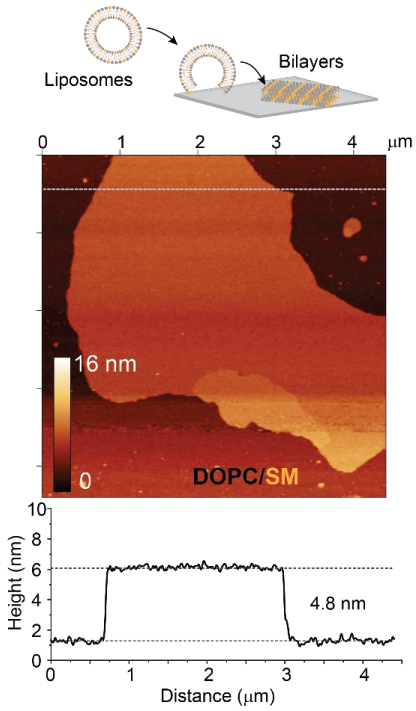

Figure 4.2: Cartoon showing the formation of SM/DOPC bilayers same as Chol/DOPC bilayers on mica substrate in **Figure 4.4a** (top). The height topography of SM/DOPC bilayers was obtained by AFM, and the height cross-section profile was extracted from the corresponding maps in the height image (bottom).

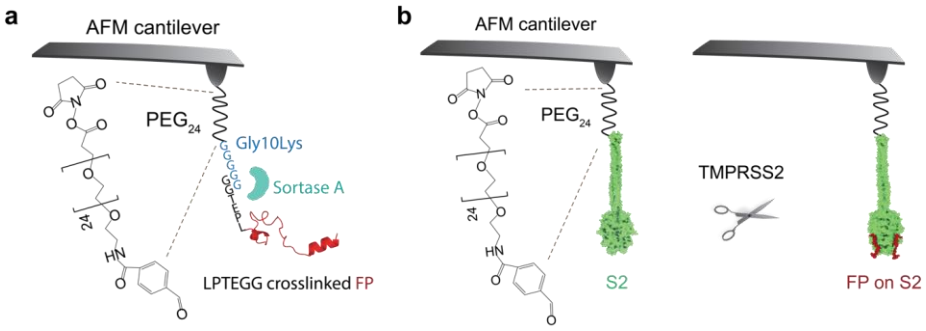

Figure 4.3: Principle of FP or S2-functionalized AFM tip. The AFM tip is functionalized with a PEG spacer fused to either $Gly_{10}Lys$ peptides or S2 subunits, which in turn react with the LPETGG-FP via the Sortase A enzyme **(a)** or treat by the TMPRSS2 **(b)**.

To investigate the binding dynamics of the FP, AFM-based SMFS was conducted in the height clamp mode (*36-38*). The functionalized AFM tip was carefully approached to a distance of 4-6 nm above the lipid bilayers, and the resulting force between the tip and the lipid bilayer was monitored for a specific duration (10 s). Analysis of the force-time curves for FP1 revealed distinct binding events, characterized by a jump to negative forces, observed in approximately 7% of the total cases (n = 180/2,519 for FP1-DOPC/Chol and n = 206/2,851 for FP1-DOPC/SM; **Figure 4.4b**). In contrast, for FP2, only a few binding events (<0.7% of total cases; 10/1,359 for FP2-DOPC/Chol and n = 6/3,528 for FP1-DOPC/SM) were detected. These findings suggest that the priming of the FP by TMPRSS2 significantly influences its binding properties to lipids, as evidenced by the lower binding events observed for FP2 compared to FP1.

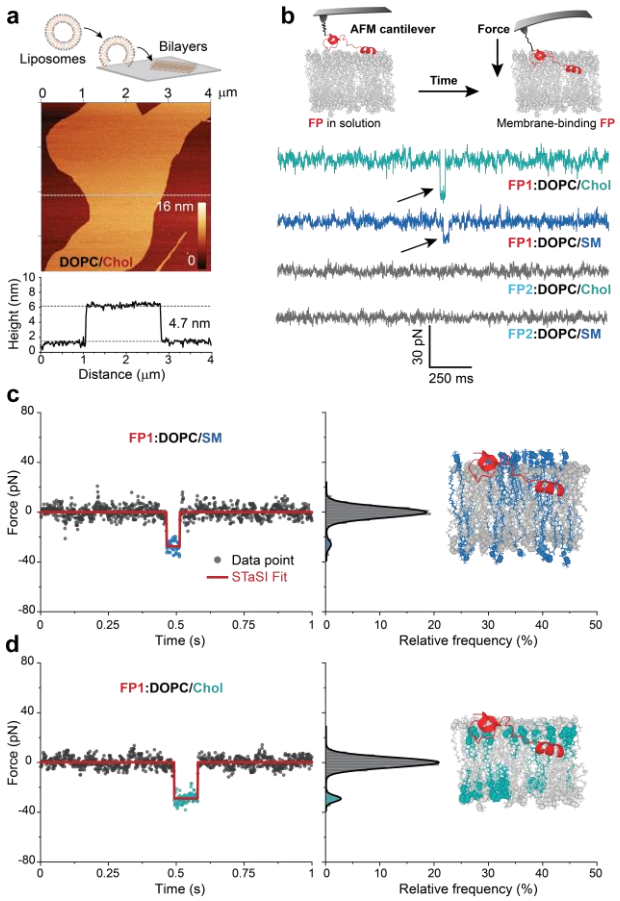

Figure 4.4: Monitoring SARS-CoV-2 FP insertion into lipid membrane using AFM-based SMFS. (**a**) Formation of lipid bilayers on solid support (top). Lipid vesicles were adsorbed onto freshly cleaved mica surface, forming lipid bilayers. AFM was used to obtain height topography of DOPC/Chol bilayers, and the height cross-section profile was extracted from the corresponding height image (bottom). (**b**) Schematic illustrating the binding of FP to the lipid bilayers monitored by AFM-based SMFS (top). Representative force-time (FT) curves showing the binding of FP1 into the lipid bilayers (indicated by black arrowhead). FP2 did not exhibit binding events on the lipid bilayers (bottom). (**c, d**) Representative FT curves of FP1 binding to the DOPC/SM membrane (**c**) or DOPC/Chol membrane (**d**). Two distinct states detected in the force-time curves were identified using the STaSI algorithm and depicted as histograms that are fitted using a multipeak Gaussian fit. Data points are color-coded based on the assignment by the STaSI model: gray represents the first and blue or cyan represents the second state.

The binding events within the collected FT trajectories were identified using a specialized algorithm called the generalized step transition and state identification (STaSI), specifically designed for analyzing discrete single-molecule data (*39*). In the FT curves, a rapid transition of the force was observed, indicating the binding of the fusion peptide (FP) from a free state to a bound state (**Figure 4.4c, d**). These events have a lifetime in the range of few hundred milliseconds. Interestingly, upon initial observation, the lifetime of the FP1 bound state appeared longer for the DOPC/Chol membrane compared to the DOPC/SM membrane. Despite the dependence of lifetime on lipid composition, the magnitude of force was found to be unaffected. This observation suggests that the presence of cholesterol (Chol) enhances the kinetics of SARS-CoV-2 FP binding to the lipid membrane (**Figure 4.4c, d**).

Extraction of the kinetics parameters

Subsequently, the lifetime and strength of the binding events between FP1 and lipid bilayers were determined for the two different lipid compositions (**Figure 4.5a**). The data were fitted using the Bell model (*36, 40*) for both lipid compositions (**Figure 4.5b, c**). This model allowed us to extract the average lifetime ($\tau(0)$) of the complex formed between FP and lipids, as well as estimate the width of the free-energy barrier (x_β) crossed by the transition from the free state to the bound state. These values provide insights into the kinetics of molecular complexes formed under thermal equilibrium conditions, without the application of any external force.

For FP1 binding on the DOPC/Chol membrane (**Figure 4.5b**), the obtained $\tau(0)$ and x_β values were 426.2 ± 76.5 ms and 0.29 ± 0.04 nm, respectively. These values were significantly higher compared to the

DOPC/SM membrane (**Figure 4.5c**), where τ(0) and x_β were 126.8 ± 18.9 ms and 0.18 ± 0.03 nm, respectively. These findings indicate that Chol helps in the formation of a more stable complex, probably facilitating the further binding of S2 to the lipid bilayer.

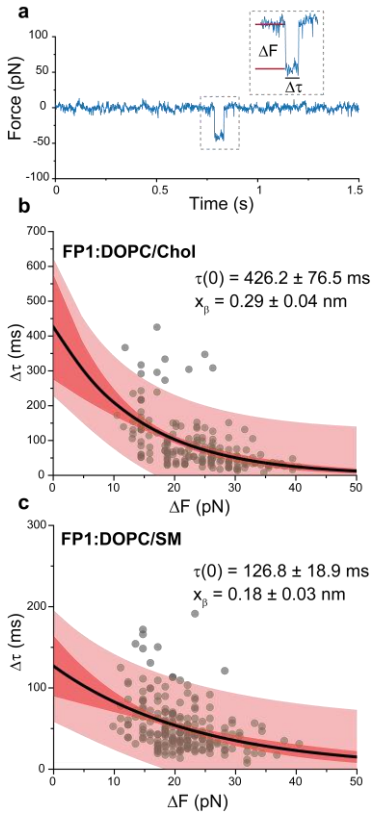

Figure 4.5: Towards the kinetics of SARS-CoV-2 FP binding to lipid membrane. (**a**) Data points are extracted from force versus time curves, resulting in force (ΔF) and lifetime (Δτ) data. (**b, c**) These data points are then plotted as a function of the lifetime in function of the force (n = 180 in **b** and n = 206 in **c**, where n represents the number of insertion events quantified). The Bell model was then employed to fit the data (black lines), providing average x_β and τ(0) values for the binding complexes. Error bars represent the mean ± standard deviation (s.d.), while darker shaded areas indicate 95% confidence intervals and lighter shaded areas represent 95% prediction intervals.

Validation of the FP binding at the S2 subunit level.

Upon binding of host receptors to the S1 subunit and subsequent processing of the S2-N terminus site by TMPRSS2, the FP of SARS-CoV-2 becomes exposed and binds to the host cell membrane, initiating the fusion process between the virus and the host cell (*18*). To confirm the cleavage of the S2 subunit to S2' by TMPRSS2, an enzyme cleavage experiment was conducted following a previously established protocol (*41*). The reaction was validated by a Western blot experiment (**Figure 4.6a**). The same strategy was followed to graft the S2' onto the AFM tip (**Figure 4.3b**). The S2 subunit was first grafted and then treated by the TMPRSS2.

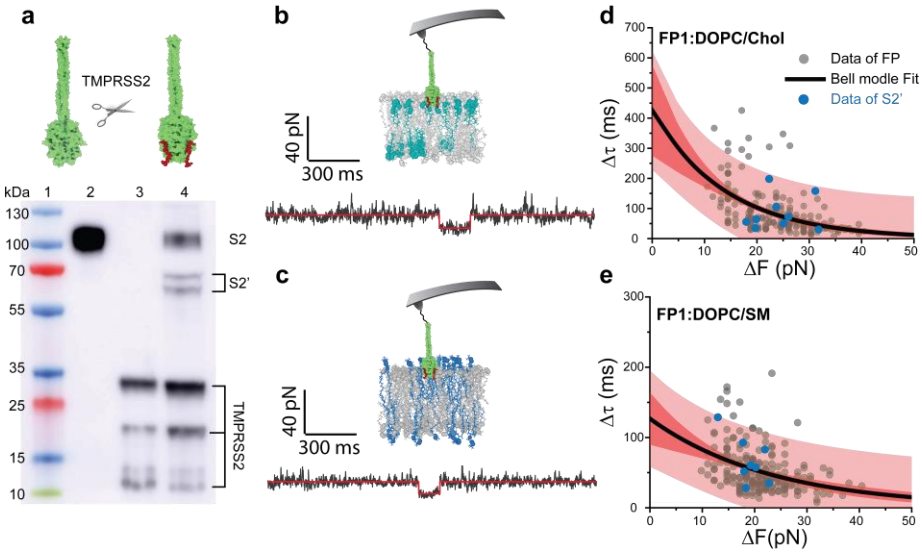

Figure 4.6: Probing the binding of SARS-CoV-2 FP at the S2 subunit level. (**a**) Western blot analysis of S2 subunit treated with TMPRSS2 under reducing conditions. The cleaved S2 subunit was detected using an antibody against the His-tag. Lane 1 represents the marker, Lane 2 represents S2, Lane 3 represents TMPRSS2, and Lane 4 represents S2 + TMPRSS2. (**b, c**) Representative force-time curves depicting the binding of S2' subunit to the lipid bilayers, either DOPC/Chol (b) or DOPC/SM (c) membranes. Raw data is plotted as a black line, and the binding states are identified using the STaSI algorithm (red line). (**d, e**) Plots

of force-dependent lifetime obtained for FP (gray circles, from Figure 4.3b and c) and for S2' subunit (blue circles, n = 9 in d and n = 8 data points in **e**).

The S2-functionalized cantilevers, further treated with TMPRSS2, were positioned above lipid bilayers using the same strategy as employed for the FP experiments described above. As previously observed for the FP, individual force-time curves clearly show specific binding of S2' domain to both the DOPC/Chol and DOPC/SM membranes (**Figure 4.6b, c**). Notably, the binding events were exclusively observed when using the S2'-functionalized tips treated with TMPRSS2 (9/374 events for S2'-DOPC/Chol and 8/355 of total cases for S2'-DOPC/SM), whereas no binding events were detected with the S2-functionalized tips alone (453 force traces for S2-DOPC/Chol and 262 for S2-DOPC/SM). These findings provide conclusive evidence that the TMPRSS2-processed S2 subunit binds its fusion peptide to the host membrane.

Furthermore, specific binding times and corresponding forces were extracted from the individual force-distance curves obtained using the S2'-functionalized AFM tips. Remarkably, these binding parameters were in excellent agreement with the previously acquired data for SARS-CoV-2 FP (**Figure 4.6d, e**). Overall, these results confirm that the exposed fusion peptide on the S2' subunit effectively binds to the host membrane, and highlight the facilitating role of Chol in the membrane component, enhancing the binding process.

The FP disulfide bridge facilitates more stable anchoring to the lipid membrane.

The SARS-CoV-2 FP has a conserved internal disulfide bond between Cys840 and Cys851, which appears to play an important role in full FP activity (*19-21, 42*). To better understand the role of this disulfide bridge in host membrane binding activity, we compared peptide binding in the absence or presence of this disulfide bridge (**Figure 4.7a**, **see Methods**). Notably, we observed specific interactions in around 17.5% of cases (n = 237/1361 for FP1-DOPC/Chol) under conditions favoring the presence of the disulfide bridge, whereas those of interactions were virtually abolished after treatment with Tris(2-carboxyethyl)phosphine hydrochloride (TCEP), a disulfide-reducing agent. Conversely, the specific strong interaction was not observed on the DOPC/SM membrane. These findings strongly indicate that the main interaction events were attributable to both the SARS-CoV-2 FP and the DOPC/Chol membrane.

As depicted in the force-time curves (**Figure 4.7b**), following the initial binding event, a subset of the curves displayed an additional step towards higher forces, suggesting the existence of a distinct secondary population or state. The STaSI algorithm effectively discerns these two populations. The collected data reveals that lifetimes range from 15 to 570 ms for forces spanning 25 to 130 pN (**Figure 4.7c**). This second state might indicate a shift in binding conformation towards enhanced stability or the binding of a second FP to the lipid membrane. Given the low occurrence of this second population within the curves (12/237 analyzed curves) and the absence of observable transitions between the two states, we hypothesized that this second population corresponds to the binding of a second FP within the lipid bilayer. To further analyze these two

populations, we analyzed the force distribution in function of the lifetimes extracted from the force-time curves. (**Figure 4.7c**). The lifetime distributions were binned across seven discrete force ranges (**Figure 4.8,** #1 to #7). Notably, the lifetime distributions in the four lower force regions (#1 to #4, F < 70 pN) exhibited a distinctive bimodal Gaussian distribution (**Figure 4.8**), with the frequency of the second peak significantly less than the first one. This double-peak distribution of lifetime in the binned force data strongly supports the occurrence of two-state events corresponding to two different affinities.

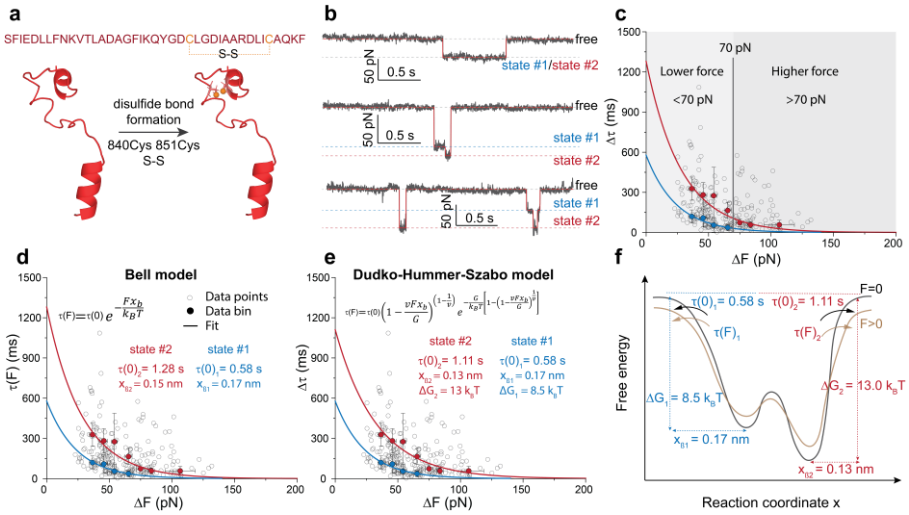

Figure 4.7: Internal disulfide bond promotes FP binding to the membrane. (**a**) The internal disulfide bond is formed in the FP between Cys840 and Cys851. (**b**) Force *vs* time curves with specific interaction events. Raw data (gray line) are processed using the STaSI algorithm (red line) to identify different states in the force trace. (**c**) The distribution of the lifetime is in the force region (range from 22-130 pN) reveals two different states. (**d, e**) Fitting the lifetime against force of the two states performed either using the Bell model (**d**) or the DHS model (**e**). (**f**) The free-energy landscape of the FP binding to the membrane under a constant force. The kinetics and thermodynamics analysis reveal a binding free-energy landscape with two states, which can be explain by the consecutive binding of two FP leading to a more stable bound state.

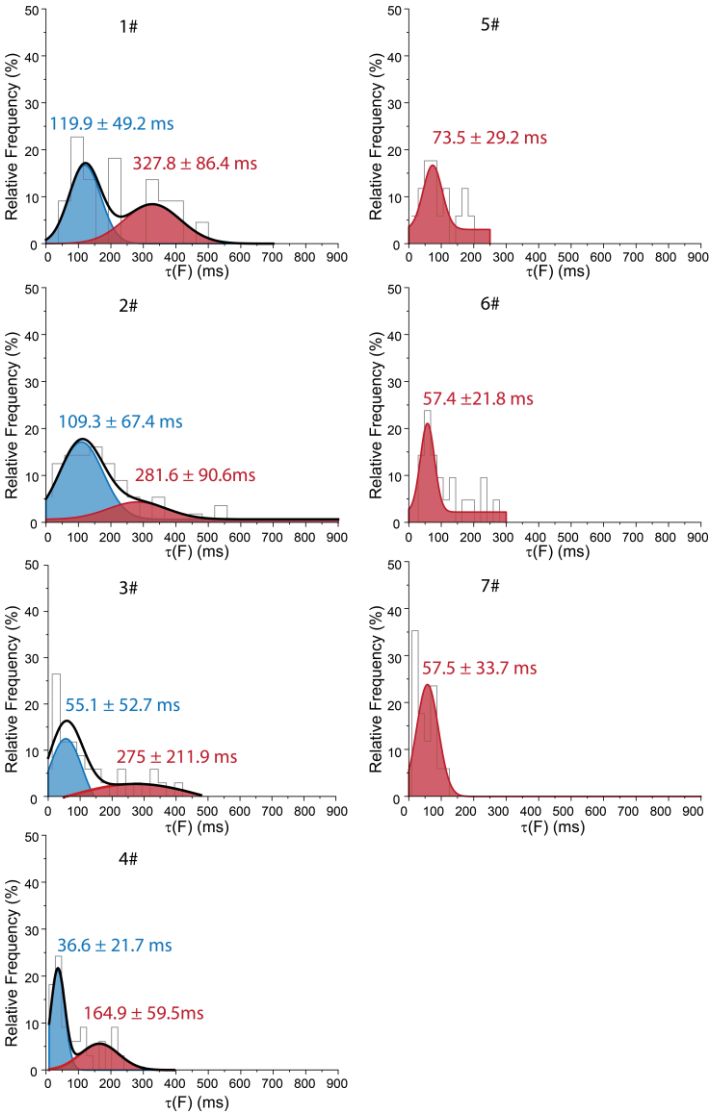

Figure 4.8: Extraction of an average lifetime for discrete forces. Small force ranges #1–#7 are binned and the distributions of the lifetime are plotted as histograms. This classification reveals two peaks with average values corresponding to single (blue) or double (red) simultaneously established FP-membrane interactions. This reveals two lifetime peaks with average values corresponding to single (blue) and double (red) simultaneously established FP-membrane interactions. The average values of the lifetime distributions are extracted and plotted on the lifetime against force, enabling their analysis using the Bell or DHS model (**Figure 4.5c, d** or **e**).

According to the Bell model (*40*), the lifetime of a bond exponentially decreases as the force increases. Applying this model, we determined the separation distance from the unbound to the bound state for the first population as $x_{\beta 1}$ = 0.17 nm and the lifetime ($\tau(0)_1$ = 0.58 s) (**Figure 4.7d**). Analysis of the second population revealed higher stability, characterized by a lower free-energy valley ($x_{\beta 2}$ = 0.15 nm) and a twofold higher lifetime ($\tau\ (0)_2$ = 1.28 s).

To better understand the thermodynamic differences between both binding states, we employed the Dudko-Hummer-Szabo (DHS) model to analyze the experimental data (*43*). This model allowed us to simultaneously determine the activation energy (ΔG) and kinetic parameters (x_β and $\tau(0)$) by examining the lifetime-force relationship (**Figure 4.7e**). We obtained values of $x_{\beta 1}$ = 0.17 nm and $\tau(0)_1$ = 0.58 s for the first population, and $x_{\beta 2}$ = 0.13 nm and $\tau(0)_2$ = 1.11 s for the second population. These results were in excellent agreement with the values obtained using the Bell model. Notably, the binding free-energy for the second population (ΔG_2 = 13 k_BT) is significantly higher than for the first population (ΔG_1 = 8.5 k_BT), indicating a stronger stabilization of FP, presumably due to the multivalent interaction.

This analysis reveals a sequential mechanism whereby an initial FP binds to the membrane, subsequently favoring the binding of a second FP that in tandem enhances the stability of the binding complex as a whole (**Figure 4.7f**). This multivalent complex demonstrates an extended lifetime and heightened binding free-energy. Significantly, the appearance of this second population was less frequent under conditions that compromise the integrity of the disulfide bridge, underlining the pivotal role of this bridge in the membrane binding process. We propose that the

disulfide bridge imparts enhanced mechanical stability to the FP-membrane complex, maintaining spatial proximity between the membrane and the peptide. This proximity fosters the subsequent attachment of new peptides, contributing to the stepwise binding process.

Cholesterol depletion inhibits SARS-CoV-2 infectivity on cells

At the single-molecule level, we observed a strong influence of cholesterol on the binding of SARS-CoV-2 FP. This led us to question whether the cholesterol level in the host cell membrane could impact SARS-CoV-2 infection. To investigate this, we conducted virus infection assays using pseudotyped viruses carrying S proteins. A549 cells expressing ACE2 and TMPRSS2 were incubated with propagation-incompetent G-deleted vesicular stomatitis virus (VSV) trans-complemented with the SARS-CoV-2 spike protein and encoding a GFP reporter protein (VSV-SARS-CoV-2). A549 cells were infected with the VSV-SARS-CoV-2. The infectivity was assessed by measuring the GFP fluorescence 24 hours post-infection. To assess the role of cholesterol, A549 cells were treated with varying concentrations of Methyl-β-cyclodextrin (MβCD), a commonly used agent for cholesterol removal from the plasma membrane (*44*). The results revealed a concentration-dependent inhibition of VSV-SARS-CoV-2 infection by MβCD (**Figure 4.9**), consistent with previous findings (*29*).

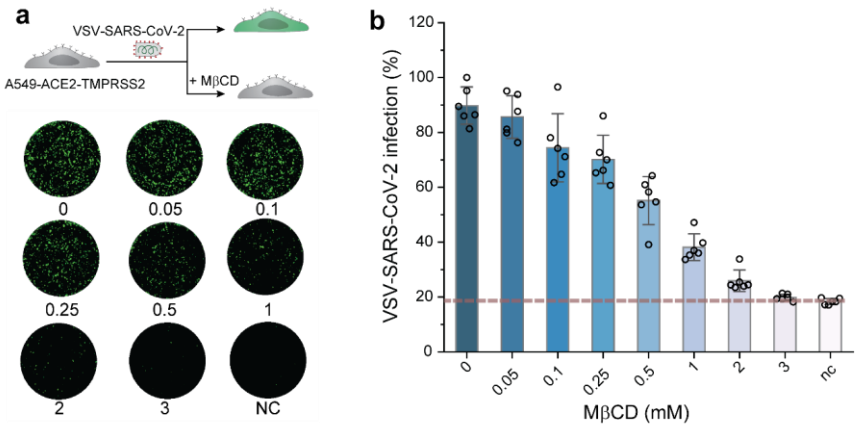

Figure 4.7: Chol depletion using MβCD inhibits SARS-CoV-2 pseudovirus entry into host cells. (**a**) Schematic representation of the SARS-CoV-2 pseudovirus infectivity assay using A549 cells expressing ACE2 and TMPRSS2 (top). Fluorescent images of infected A549/ACE2/TMPRSS2 cells in the presence of different concentrations of MβCD (0, 0.05, 0.1, 0.25, 0.5, 1, 2, 3 mM, and NC: negative control, without virus) (bottom). (**b**) Mean infectivity measured at various concentrations of MβCD. Each black dot represents infectivity from a well. The column indicates the mean value, and the whiskers indicate the standard deviation (s.d.) of the mean. Data are representative of three independent replicates.

4.4 Discussion

In this study, we elucidate how Chol facilitates the interaction between SARS-CoV-2 FP and the target cell's membrane. Through BLI, we determined that the affinity of SARS-CoV-2 FP for the DOPC/Chol membrane is tenfold greater compared to its affinity for the DOPC/SM membrane. This observation is reinforced by our AFM-based SMFS experiments, where we directly captured FP binding to the membrane at the single-peptide level. Our kinetic analysis highlights that FP binding to the DOPC/Chol membrane exhibits a prolonged lifetime compared to the DOPC/SM membrane control, indicating that Chol contributes to the stabilization of the bound complex. Importantly, we also established that conditions preserving the integrity of the disulfide bridge within FP enhance the mechanical stability of the binding, thereby facilitating the establishment of multiple interactions.

Membrane fusion is an important event in the entry of SARS-CoV-2, which is utilized to trigger release of genetic cargo into the host cell to achieve the purpose of the cellular infection. This vital and conserved step of the viral life cycle involves in several complicated factors, including the microenvironment of membrane fusion, the properties of FP, and the components of lipid membrane (*25, 26, 45*). Because the essential membrane fusion event of SARS-CoV-2 occurs either at the cell surface or within cellular endocytic compartments (*46*), recent studies have reported the SARS-CoV2 FP binding to the membrane in the presence of calcium ions (*47-49*). SARS-CoV-2 FP, as a membrane fusion apparatus, is highly conserved in the coronavirus family (*18*), which has been a pharmaceutical target against coronavirus infection (*22, 23*). The

membrane fusogenicity is enhanced when the N-terminal region of fusion peptide is exposed, thus having an important role in disease transmission (*7, 8, 34*). Consistent with these observations, our results showed that unexposed N-terminus of SARS-CoV-2 FP do not bind to supported lipid membranes. Our results demonstrated that priming of FP by the TMPRSS2 promotes the binding to the lipid membrane which is in good agreement with the recent observed cryo-EM structure (*50*).

Another dominant factor that determines membrane fusion could be the composition of the lipid membrane itself (*51*). Due to the significant energy barrier that must be overcome during membrane fusion, the composition of the membranes could potentially impact this process through various mechanisms. (*25*). Chol stands out among lipids as a critical factor influencing the membrane fusion of SARS-CoV-2 (*27-29*). It initially reduces the energetic demand for interactions between the lipid bilayers of both the virus and the cell due to its capability to stabilize hydrophobic interactions. Here, we demonstrate Chol's role in favoring the binding of the SARS-CoV-2 FP. Consequently, Chol could increase the binding energy between the viral protein and the membrane, effectively lowering the energy required for the S2 subunit's refolding in membrane fusion. Additionally, our findings reveal that the infection mediated by SARS-CoV-2 pseudotyped particles is impeded following Chol removal from the host membrane. Collectively, these findings suggest that Chol might have a crucial involvement in SARS-CoV-2 infection and could be a viable target for developing effective therapies against the virus. This aligns well with prior research demonstrating the antiviral effects of cholesterol-25-hydroxylase (*52, 53*) and statins (*54*) against SARS-CoV-2, observed both in vitro and *in vivo*.

In conclusion, this study illuminates the role of Chol in enhancing the binding of SARS-CoV-2 FP to the lipid membrane, with this process notably reliant on FP priming via TMPRSS2. The internal disulfide bond emerges as a key factor stabilizing the FP-membrane complex. Additionally, the Chol content within the host membrane significantly influences SARS-CoV-2 infection. Our findings not only provide a mechanistic understanding of how Chol crucially boosts SARS-CoV-2 infection but also offer insights for devising broadly effective therapies capable of addressing emerging variants and potential future coronavirus outbreaks.

4.5 Methods

Reagents and Fusion peptides.

Brain Sphingomyelin (SM; Avanti Polar Lipids); Cholesterol (Chol; Sigma); 1,2-dioleoyl-sn-glycero-3-phosphocholine (DOPC; Avanti Polar Lipids); DPBS (Fisher); Sortase A (BPS Bioscience, San Diego, CA, USA); NHS-PEG_{24}-Ph-aldehyde spacer (Broadpharm, San Diego, CA, USA); poly-Glycine linker (Genscript, NJ, USA). Unless states otherwise, all chemical reagents were purchased from Sigma (Missouri, USA).

The fusion peptides (FP1 and FP2) of SARS-CoV-2 with a purity of >95% were purchased commercially from GenScript. Two following peptides were investigated:

FP1: 816-SFIEDLLFNKVTLADAGFIKQYGDCLGDIAARDLICAQKF-855

FP2: 806-ILPDPSKPSKRSFIEDLLFNKVTLADAGFIKQYGDCLGDIAARDLICAQKF-855

They are with LPETGG-tag modification at the C-termini. The peptides were dissolved in DPBS and stored at −20 °C in 20 µl small stock aliquots.

Preparation of lipid vesicles.

DOPC, brain SM, and Chol were dissolved in chloroform to give a final lipid concentration of 5 mM. Aliquots of DOPC and SM or Chol solutions were mixed in DOPC/SM and DOPC/Chol in molar ratios (70/30) and poured into a glass vial. Then, the resultant solutions were dried under a nitrogen flow and kept for 20 min in a vacuum desiccator to ensure complete removal of chloroform. Multilamellar vesicles were obtained by hydration with the Buffer A (20 mM HEPES and 50 mM NaCl at pH 7.4) solution to give a final lipid concentration of 1 mM, as previously described (*31*). To obtain the lipid vesicles, the mixed solution was extruded through Whatman Nuclepore Hydrophilic Membrane with a 100

nm pore size using an Avanti Mini-Extruder (Avanti Polar Lipids, Alabama, USA).

Supported lipid bilayers for AFM-based SMFS experiments.

Supported lipid bilayers were prepared on circular mica surfaces for AFM-based SMFS experiments as described previously (*31*). In brief, the lipid vesicles were dropped on the freshly cleaved mica surfaces cemented onto Teflon discs with epoxy-based mounting glue. A metal puck was used as a supporting substrate for the Teflon discs and were magnetically mounted on the AFM stage. The deposited small lipids vesicles on the surface were incubated at 60 °C for 1h to obtain the lipid-supported bilayers. The samples were rinsed with Buffer B (20 mM HEPES, 50 mM NaCl, and 2 mM Ca_2Cl at pH 7.4) maintained at 60 °C and then slowly cooled to room temperature.

Functionalization of AFM tips and disulfide bond formation in peptide.

To functionalize peptides/proteins to AFM tips, FPs and S2 subunits were grafted onto AFM tips apex (AC40, Bruker), using the following protocol: the AFM tips were washed in chloroform (3 x 10 min), cleaned in a UV-ozone (UV-O) cleaner (Jelight, California, USA). The tips were further incubated for 2 h in an argon-filled desiccator with 30 µL APTES and 10 µL triethylamine. To cure the APTES coating, the tips were maintained under argon for 2 days. To graft the respective peptide or protein on the AFM tip, a heterobifunctional NHS-PEG_{24}-Ph-aldehyde was grafted on the amino-functionalized tips. NHS-PEG_{24}-Ph-aldehyde (3.3 mg) was dissolved in chloroform (0.5 mL) and trimethylamine (30 µL). The cantilevers were immersed in the solution for 2 hours and washed 3 times with chloroform and dried with nitrogen. The cantilevers were immersed in the 100 µL Gly_{10}Lys peptide (1 mM) or S2 subunit (300 nM) solution

with 2 µL fresh $NaCNBH_3$ at 4°C for 1 h. Then, 5 µl of 1 M ethanolamine solution (pH 8.0, 10 min, R.T) was added to the solution to quench the unreacted aldehyde groups and washed 5 times with DPBS buffer. The S2 subunit-functionalized AFM tips were directly used for binding assays. To obtain FPs-functionalized AFM tips, the $Gly_{10}Lys$ peptide-modified tips was then incubated with 50 µl of a 10 µM FPs and 50 µl of a 20 µM Sortase A solution for 4 h at 37 °C. FPs-tips were rinsed with HEPES buffer and stored at 4 °C and used in AFM experiments on the same day.

A efficient method for disulfide bond formation in peptide is described (*55*). The AFM tip of the functionalized FP1 was rinsed by HEPES buffer. This tip was reacted with 20% dimethyl sulfoxide (DMSO) at pH 6 in room temperature for 4h. This tip was then rinsed with HEPES buffer and stored in 4°C until used in AFM experiments.

AFM-based single-molecule force spectroscopy.

A Bioscope Resolve AFM (Bruker) with a 100 µm piezoelectric scanner was used to image the lipid bilayers with PeakForce QNM mode (Nanoscope software v9.2, Bruker, Santa Barbara, USA). Using the bare or non-functionalized cantilevers, the membrane patches were imaged at an imaging force in 250 pN, 100 nm ramp size, and 256×256 pixels and scan size of 10 × 10 µm. After finding membrane patches, the tips were moved closer to the membrane about 100 pN in the height clamp mode. The AFM tip was then retracted 4-6 nm away from the surface. Since the S2 protein is larger, the retracted height of the tip in this case is 8-10 nm. Next, the cantilever was kept at a constant height for 10 s while recording the cantilever deflection to collect force-time (FT) curves. After that time, the cantilever was retracted by 50 nm and the measurement were repeated. Cantilever spring constants were calibrated using the thermal tune

method and deflection sensitivity was measured by ramping on hard surfaces. All experiments were performed at room temperature and repeated at least five times.

Analysis of force–time curves and extraction of kinetic parameters.

After excluding curves without binding events by Nanoscope analysis 2.0, FT curves with the binding events were run to correct the baseline using an asymmetric least-squares baseline algorithm in Origin 2021 software. The specific binding events were identified using adapted the step transition and state identification (STaSI) (*39*) algorithm developed for discrete single-molecule data analysis for our data. The STaSI algorithm detects step transitions using Student's t-test and then groups segments by hierarchical clustering. The optimum number of states is suggested by weighing the complexity of the model and the goodness of fit (minimum description length) to find the simplest model with the least fitting error. We extensively tested the STaSI algorithm by generating traces with two states.

Estimation of kinetic and thermodynamic parameters of the binding events was performed by fitting the Bell (*36, 40*) (**Figure 4.5**) model with nonlinear curve fitting tool in Origin 2021. Data from force clamp experiments were fitted to the Bell model using the equation:

$$\tau\,(F) = \tau(0) * e^{-\frac{Fx_\beta}{k_B T}} \qquad (1)$$

where $\tau(F)$ is the complex of FP-membrane lifetime as a function of force, $\tau(0)$ is the bond lifetime in equilibrium, x_β is the width of the energy valley, k_B is the Boltzmann constant, and T the temperature.

To evaluate the free energy of activation energy (ΔG), Dudko-Hummer-Szabo (DHS) is described (*43*). The DHS formalism adds a

parameter to the BE model that enables a smooth interpolation between different potential shapes, which is the apparent free energy of activation ΔG. The DHS model was validated as a simple method to determine force-dependent lifetimes τ(F) at a constant force:

$$\tau(F) = \tau(0)\left(1 - \frac{\nu F x_\beta}{\Delta G}\right)^{\left(1-\frac{1}{\nu}\right)} e^{-\frac{\Delta G}{k_B T}\left[1-\left(1-\frac{\nu F x_\beta}{\Delta G}\right)^{\frac{1}{\nu}}\right]} \quad (2)$$

where τ(F) is the complex of FP-membrane lifetime as a function of force, τ(0) is the bond lifetime in equilibrium, x_β is the width of the energy valley, k_B is the Boltzmann constant, and T the temperature. The scaling factor specifies the nature of the underlying free-energy profile: ν = 1 corresponds to the BE expression (*43*).

Biolayer interferometry assay.

Kinetic analysis was performed on Amine Reactive Second-Generation (AR2G) biosensors (Sartorius) on an Octet BLI (BLI, Octet, Sartorius, Göttingen, Germany). First, the sensors were activated with EDC (1-Ethyl-3 [3-dimethylaminopropyl] carbodiimide hydrochloride) and NHS (N-hydroxysulfosuccinimide) to generate highly reactive NHS esters. FPs (10 μM) were immobilized on the activated sensor surface. After this covalent grafting step, the unreacted ester groups were quenched with 1 M ethanolamine solution, following which the resultant sensors were made to react with a serial dilution of lipid vesicles (0.075, 0.125, 0.25, 0.5, and 1 mM in PBS) for 300 s. Subsequently, the biosensors were allowed to dissociate in a kinetic buffer for 300 s. All measurements were conducted at RT and 1000 rpm shaker speed. The data were analyzed using the Octet Data Analysis 11.0 software (Octet) using a 1:1 isotherm model to calculate respective dissociation constants.

TMPRSS2 cleavage of S2 and western blotting.

To confirm the S2 subunit is cleaved by TMPRSS2, the 5 μl (1.5 μM in Tris buffer) purified S2 was incubated with 20 μl (5 μM) TMPRSS2 in 50 mM Tris buffer (0.2% Triton X-100, 50 mM NaCl, pH 7.2) overnight at 37°C, which was analyzed by Western blot. The cleaved S2 subunit was run in SDS-polyacrylamide gel electrophoresis and subsequently transferred onto a PVDF membrane (Bio RAD, California, USA). The membrane was blocked with 1% BSA in TBS solution with 0.1% Tween-20 for 1 h, incubated with 0.5 μg/ml of primary antibody with His-tag (Bio-connect) overnight at 4°C, and incubated with secondary antibody (anti-His). Then, the membrane was analyzed by Amersham Imager 600 (Cytiva). The S2-functionalized AFM tips were treated with TMPRSS2 under the same conditions with cleavage of S2 in vitro. Mock treatment was conducted without enzymes.

Pseudotyped SARS-CoV-2 production and Infection.

HEK 293T was grown in DMEM medium supplemented with 10% fetal bovine serum (FBS) with penicillin (100 U mL^{-1}) and streptomycin (100 μg mL^{-1}) (Gibco, Fisher Scientific, UK) in a humidified incubator with 5% CO_2 at 37 °C. 293T cell line was used to produce pseudotyped VSV-SARS-CoV-2. The subconfluent HEK 293T cells in a T75 flask were transfected with 15 μg of the pCAG_SARS_2Sdel18 (a generous gift from Stefan Pöhlmann) expression plasmid using Lipofectamine LTX (Invitrogen, MA, USA) according to the manufacturer's protocol. After 8 hours, cells were washed 3 times with DPBS and incubated with VSV-ΔG pseudovirus complemented in trans with the G glycoprotein and bearing a FLuc gene. Cell supernatants containing S protein-pseudotyped VSV were harvested 48 h later, clarified by low-speed centrifugation (900 × g for 10 min), and

characterized or stored at −80 °C for later analysis.

A459-ACE2-TMPRSS2 cells were grown in RPMI 1640 medium supplemented with 10% FBS with penicillin (100 U mL^{-1}) and streptomycin (100 μg mL^{-1}) (Gibco) in a humidified incubator with 5% CO_2 at 37°C. To check the pseudotyped SARS-CoV-2 infection in the absence of Chol, the A459-ACE2-TMPRSS2 cell was confluent in 96 well plates. A459-ACE2-TMPRSS2 cells were pre-treated with different concentrations of MβCD (used to deplete Chol at the cell surface membrane) for 1.5 h and then incubated with SARS-CoV-2 S protein-bearing pseudoviruses at 37°C in a humidified atmosphere of 5% CO_2 for 5h. Subsequently, the unbound pseudoviruses were removed by washing with DPBS, and cells were incubated in fresh DMEM medium with 10% FBS, penicillin, and streptomycin for 24h. The pseudotyped SARS-CoV-2 intensity activity was detected analyzed using Typhoon (ImageQuantTL software).

ACKNOWLEDGEMENTS

This work was supported by the Université catholique de Louvain and the Fonds National de la Recherche Scientifique (FRS-FNRS). This project received funding from the European Research Council under the European Union's Horizon 2020 research and innovation program (grant agreement no. 758224) and from the FNRS-Welbio (Grant # CR-2019S-01). The funders had no role in study design, data collection and analysis, decision to publish, or preparation of the manuscript. Q.Z. and D.A. are grateful to China Scholarship Council.

4.6 Reference

1. N. Zhu et al., A Novel Coronavirus from Patients with Pneumonia in China, 2019. *New England Journal of Medicine* 382, 727-733 (2020).

2. M. Hoffmann, H. Kleine-Weber, S. Pöhlmann, A Multibasic Cleavage Site in the Spike Protein of SARS-CoV-2 Is Essential for Infection of Human Lung Cells. *Molecular Cell* 78, 779-784.e775 (2020).

3. J. Shang et al., Cell entry mechanisms of SARS-CoV-2. *Proceedings of the National Academy of Sciences* 117, 11727-11734 (2020).

4. H. T. Nguyen et al., Spike Glycoprotein and Host Cell Determinants of SARS-CoV-2 Entry and Cytopathic Effects. *Journal of Virology* 95, e02304-02320 (2021).

5. A. C. Walls et al., Structure, Function, and Antigenicity of the SARS-CoV-2 Spike Glycoprotein. Cell 181, 281-292.e286 (2020).

6. D. Wrapp et al., Cryo-EM structure of the 2019-nCoV spike in the prefusion conformation. *Science* 367, 1260-1263 (2020).

7. C. B. Jackson, M. Farzan, B. Chen, H. Choe, Mechanisms of SARS-CoV-2 entry into cells. Nature Reviews Molecular Cell Biology 23, 3-20 (2022).

8. M. Hoffmann et al., SARS-CoV-2 Cell Entry Depends on ACE2 and TMPRSS2 and Is Blocked by a Clinically Proven Protease Inhibitor. *Cell* 181, 271-280.e278 (2020).

9. X. Fan, D. Cao, L. Kong, X. Zhang, Cryo-EM analysis of the post-fusion structure of the SARS-CoV spike glycoprotein. *Nature Communications* 11, 3618 (2020).

10. L. Tai et al., Nanometer-resolution in situ structure of the SARS-CoV-2 postfusion spike protein. *Proceedings of the National Academy of Sciences* 118, e2112703118 (2021).

11. T. N. Starr et al., SARS-CoV-2 RBD antibodies that maximize breadth and resistance to escape. *Nature* 597, 97-102 (2021).

12. D. Pinto et al., Cross-neutralization of SARS-CoV-2 by a human monoclonal SARS-CoV antibody. *Nature* 583, 290-295 (2020).

13. R. Raman, K. J. Patel, K. Ranjan, COVID-19: Unmasking Emerging SARS-CoV-2 Variants, Vaccines and Therapeutic Strategies. Biomolecules 11, 993 (2021).

14. A. Z. Wec et al., Broad neutralization of SARS-related viruses by human monoclonal antibodies. *Science* 369, 731-736 (2020).

15. G. Song et al., Cross-reactive serum and memory B-cell responses to spike protein in SARS-CoV-2 and endemic coronavirus infection. Nature Communications 12, 2938 (2021).

16. M. M. Sauer et al., Structural basis for broad coronavirus neutralization. *Nature Structural & Molecular Biology* 28, 478-486 (2021).

17. L. Piccoli et al., Mapping Neutralizing and Immunodominant Sites on the SARS-CoV-2 Spike Receptor-Binding Domain by Structure-Guided High-Resolution Serology. *Cell* 183, 1024-1042.e1021 (2020).

18. T. Tang, M. Bidon, J. A. Jaimes, G. R. Whittaker, S. Daniel, Coronavirus membrane fusion mechanism offers a potential target for antiviral development. *Antiviral Research* 178, 104792 (2020).

19. H. Shen, Z. Wu, Effect of Disulfide Bridge on the Binding of SARS-CoV-2 Fusion Peptide to Cell Membrane: A Coarse-Grained Study. *ACS Omega* 7, 36762-36775 (2022).

20. S. L. Schaefer, H. Jung, G. Hummer, Binding of SARS-CoV-2 Fusion Peptide to Host Endosome and Plasma Membrane. *The Journal of Physical Chemistry B* 125, 7732-7741 (2021).

21. D. Birtles, J. Lee, Identifying Distinct Structural Features of the SARS-CoV-2 Spike Protein Fusion Domain Essential for Membrane Interaction. *Biochemistry* 60, 2978-2986 (2021).

22. J. S. Low et al., ACE2-binding exposes the SARS-CoV-2 fusion peptide to broadly neutralizing coronavirus antibodies. *Science* 377, 735-742 (2022).

23. R. D. de Vries et al., Intranasal fusion inhibitory lipopeptide prevents direct-contact SARS-CoV-2 transmission in ferrets. *Science* 371, 1379-1382 (2021).

24. C. Dacon et al., Broadly neutralizing antibodies target the coronavirus fusion peptide. *Science* 377, 728-735 (2022).

25. S. C. Harrison, Viral membrane fusion. *Virology* 479-480, 498-507 (2015).

26. S. C. Harrison, Viral membrane fusion. Nature Structural & Molecular Biology 15, 690-698 (2008).

27. D. W. Sanders et al., SARS-CoV-2 requires cholesterol for viral entry and pathological syncytia formation. *eLife* 10, e65962 (2021).

28. G. P. Pattnaik, S. Bhattacharjya, H. Chakraborty, Enhanced Cholesterol-Dependent Hemifusion by Internal Fusion Peptide 1 of SARS Coronavirus-2 Compared to Its N-Terminal Counterpart. *Biochemistry* 60, 559-562 (2021).

29. X. Li et al., Dependence of SARS-CoV-2 infection on cholesterol-rich lipid raft and endosomal acidification. *Computational and Structural Biotechnology Journal* 19, 1933-1943 (2021).

30. Y. Cai et al., Distinct conformational states of SARS-CoV-2 spike protein. *Science* 369, 1586-1592 (2020).

31. A. C. Dumitru et al., High-resolution mapping and recognition of lipid domains using AFM with toxin-derivatized probes. *Chemical Communications* 54, 6903-6906 (2018).

32. H.-T. Cheng, Megha, E. London, Preparation and Properties of Asymmetric Vesicles That Mimic Cell Membranes. *Journal of Biological Chemistry* 284, 6079-6092 (2009).

33. P. Guardado-Calvo et al., A glycerophospholipid-specific pocket in the RVFV class II fusion protein drives target membrane insertion. *Science* 358, 663-667 (2017).

34. S. Yu et al., SARS-CoV-2 spike engagement of ACE2 primes S2′ site cleavage and fusion initiation. *Proceedings of the National Academy of Sciences* 119, e2111199119 (2022).

35. N. Kahya, D. Scherfeld, K. Bacia, B. Poolman, P. Schwille, Probing Lipid Mobility of Raft-exhibiting Model Membranes by Fluorescence Correlation Spectroscopy. J*ournal of Biological Chemistry* 278, 28109-28115 (2003).

36. P. R. Laskowski et al., Monitoring the binding and insertion of a single transmembrane protein by an insertase. *Nature Communications* 12, 7082 (2021).

37. P. J. Bujalowski, A. F. Oberhauser, Tracking unfolding and refolding reactions of single proteins using atomic force microscopy methods. *Methods* 60, 151-160 (2013).

38. M. P. Stewart, Y. Toyoda, A. A. Hyman, D. J. Müller, Tracking mechanics and volume of globular cells with atomic force microscopy using a constant-height clamp. *Nature Protocols* 7, 143-154 (2012).

39. B. Shuang et al., Fast Step Transition and State Identification (STaSI) for Discrete Single-Molecule Data Analysis. *The Journal of Physical Chemistry Letters* 5, 3157-3161 (2014).

40. G. I. Bell, Models for the Specific Adhesion of Cells to Cells. Science 200, 618-627 (1978).

41. Q. Zhang et al., Stepwise Enzymatic-Dependent Mechanism of Ebola Virus Binding to Cell Surface Receptors Monitored by AFM. *Nano Letters* 22, 1641-1648 (2022).

42. D. Birtles, A. E. Oh, J. Lee, Exploring the pH dependence of the SARS-CoV-2 complete fusion domain and the role of its unique structural features. *Protein Sci.* 31, e4390 (2022).

43. O. K. Dudko, G. Hummer, A. Szabo, Theory, analysis, and interpretation of single-molecule force spectroscopy experiments. *Proceedings of the National Academy of Sciences* 105, 15755-15760 (2008).

44. M. Brameshuber et al., Imaging of Mobile Long-lived Nanoplatforms in the Live Cell Plasma Membrane. *Journal of Biological Chemistry* 285, 41765-41771 (2010).

45. L. G. M. Basso, A. E. Zeraik, A. P. Felizatti, A. J. Costa-Filho, Membranotropic and biological activities of the membrane fusion peptides from SARS-CoV spike glycoprotein: The importance of the complete internal fusion peptide domain. *Biochim. Biophys. Acta* 1863, 183697 (2021).

46. J. Koch et al., TMPRSS2 expression dictates the entry route used by SARS-CoV-2 to infect host cells. *The EMBO Journal* 40, e107821 (2021).

47. A. L. Lai, J. H. Freed, SARS-CoV-2 Fusion Peptide has a Greater Membrane Perturbating Effect than SARS-CoV with Highly Specific Dependence on Ca2+. *Journal of Molecular Biology* 433, 166946 (2021).

48. G. Khelashvili, A. Plante, M. Doktorova, H. Weinstein, Ca2+-dependent mechanism of membrane insertion and destabilization by the SARS-CoV-2 fusion peptide. *Biophysical Journal* 120, 1105-1119 (2021).

49. R. K. Koppisetti, Y. G. Fulcher, S. R. Van Doren, Fusion Peptide of SARS-CoV-2 Spike Rearranges into a Wedge Inserted in Bilayered Micelles. Journal of the American Chemical Society 143, 13205-

13211 (2021).

50. W. Shi et al., Cryo-EM structure of SARS-CoV-2 postfusion spike in membrane. *Nature*, (2023).

51. G. Meher, H. Chakraborty, Membrane Composition Modulates Fusion by Altering Membrane Properties and Fusion Peptide Structure. *The Journal of Membrane Biology* 252, 261-272 (2019).

52. R. Zang et al., Cholesterol 25-hydroxylase suppresses SARS-CoV-2 replication by blocking membrane fusion. *Proceedings of the National Academy of Sciences* 117, 32105-32113 (2020).

53. S. Wang et al., Cholesterol 25-Hydroxylase inhibits SARS-CoV-2 and other coronaviruses by depleting membrane cholesterol. *The EMBO Journal* 39, e106057 (2020).

54. N. M. Schmidt, P. A. C. Wing, J. A. McKeating, M. K. Maini, Cholesterol-modifying drugs in COVID-19. *Oxford Open Immunology* 1, (2020).

55. J. P. Tam, C. R. Wu, W. Liu, J. W. Zhang, Disulfide bond formation in peptides by dimethyl sulfoxide. Scope and applications. *Journal of the American Chemical Society* 113, 6657-6662 (1991).

Chapter 5:

General discussion

The stepwise entry of enveloped viruses involves their binding to receptors, the activation of viral glycoproteins, the exposure of the fusion domain, bridging between the viral and cellular membranes at the fusion domain, and finally, the initiation of membrane fusion. This stepwise entry mechanism is relatively conserved among all enveloped viruses. It is also the most fundamental and central process in the infection pathway, representing the primary target for the development of vaccines and antiviral agents. Therefore, gaining a deep understanding of the intricate process of enveloped viral entry is crucial for unraveling the biology of viral infections and advancing the development of vaccines and antiviral agents.

In this thesis, I initially explore the molecular mechanisms underlying the interaction between EBOV and cell surface receptors, as well as the actions of host enzymes, all at the single-virus level. Subsequently, I delve into the binding and incorporation of the fusion peptide (FP) of SARS-CoV-2 into the lipid membrane. As a result, this discussion section is structured into three distinct segments.

The first part focuses on the molecular mechanisms associated with the binding of enveloped viruses to cell surface receptors, taking into consideration the outcomes of the EBOV receptor binding experiments. This section also examines the influence of host enzymes on this interaction.

Moving to the second part, I elaborate on the fusion domain interaction of enveloped viruses with the host membrane. This analysis is supported by an interpretation of the binding behavior of the fusion peptide (FP) from SARS-CoV-2 to the lipid membrane.

Moreover, within this context, I address certain technical aspects of AFM-based SMFS that contribute to the work's methodology. Furthermore, I discuss the potential for extending these findings to future research endeavors centered around related topics.

5.1 Virus-receptor interactions in the entry of enveloped viruses

The entry of the enveloped viruses into host cells is initiated by their attachment to the surface of the host cell. This complex process determines the cellular tropism and specificity of the virus and depends on several sequential events to establish stable binding between the virus and the host cell. Both viral glycoproteins and lipids play a key role in the binding of the virus to the host cell. Interactions between viral glycoproteins and cellular receptors are common in all viral binding, both in non-enveloped and enveloped viruses. In contrast, interactions between viral lipids and cellular receptors are entirely specific to the entry of enveloped viruses. Based on ensemble assays that analyze the behavior of viral particles, the interaction mechanisms between enveloped viruses and cellular receptors are well described. However, the quantitative details of the interactions between viral glycoproteins and cellular receptors are still poorly understood at the level of single viruses. In particular, studying the interactions between viral lipids and cellular receptors, an aspect that currently receives little attention in enveloped virus invasion, will expand our understanding of infections.

To facilitate understanding of the interaction of viral glycoproteins or lipids with cellular receptors, we studied the binding of EBOV to cell surface receptors (**details in Chapter 3**). We first identified DC-SIGNR and TIM-1, named C-type lectin, dendritic cell-specific intercellular adhesion molecule-3-grabbing nonintegrin receptor, and T-cell Ig and mucin domain 1, as specific receptors for EBOV. Highlights of this work at the level of a single virus include: i) demonstrating that DC-SIGNR binds

to the EBOV glycoprotein (GP), ii) confirming that TIM-1 has affinity for both EBOV GP and phosphatidylserine (PS) and serves as a dual-function receptor; iii) extracting the kinetic and thermodynamic parameters of these interactions, and iv) assessing the binding of EBOV to receptors on living cells. Intriguingly, we also found that the binding of EBOV to cell surface receptors depends on a stepwise activation mechanism of host proteinases, whereby the host proteinase promotes the binding of TIM-1 to PS by cleavage GP.

Enveloped viruses use elegant strategies to bind to one or more receptors. Our results confirm that the attachment factors of EBOV are its GP or PS on the envelope, which binds to DC-SIGNR or TIM-1 on the surface of the host cell. These results are consistent with previous reports that DC-SIGNR acts as an attachment factor for EBOV to enter the host cells (*1*) and TIM-1 serves as a receptor for EBOV on mucosal epithelial surfaces (*2*). Crystal structures of carbohydrate-recognizing domains of DC-SIGNR have confirmed that this receptor selectively recognizes oligosaccharides with high mannose content (*3*). Recently, EBOV GP was reported to be highly glycosylated with mannose (*4*). Considering the binding between GP and DC-SIGNR, a possible alternative explanation is that DC-SIGNR binds directly to glycans on GP, more specifically, to mannose. Indeed, DC-SIGNR is widely used as an attachment factor in enveloped viruses (*5, 6*). More importantly, the potential discovery that the viral envelope PS serves as an attachment factor could significantly advance virological research and the development of antiviral therapies, as PS is widely used in enveloped viruses such as HIV (*7*), dengue virus (*8*), influenza virus (*9*), and SARS-CoV-2 (*10*). The binding between TIM-1 and EBOV PS plays a crucial role in answering the question of how TIM-

related proteins interact with EBOV-PS and provides valuable insights into the infection mechanism of various enveloped viruses through their PS (*11*).

On the other hand, the infection of enveloped viruses is strictly governed by the thermodynamics and kinetics of the interactions between viruses and receptors. Unfortunately, thermodynamics and kinetics are often overshadowed by complicated molecular and biochemical processes. In this thesis, a major goal is to characterize the thermodynamic potentials and kinetics of EBOV as it interacts with host cell receptors at the single-virus level. Using AFM-based SVFS, we directly quantified the kinetics and thermodynamics of EBOV binding to DC-SGIN or TIM-1 in vitro and on living cells. It was suggested that a high binding affinity between EBOV and DC-SIGNR or TIM-1 correlates with a wide range of susceptibility to different cells, tissues, and organs in humans (*12*).

Surprisingly, AFM-based SVFS revealed that TIM-1 acts as a dual-function receptor of EBOV, as it can also directly interact with PS and GP on the envelope. The results may clarify why TIM-1 is a functional receptor for EBOV entry but just DC-SIGNR as an attachment factor. Furthermore, our research findings strikingly demonstrate that TIM-1 prefers binding with EBOV-PS after the GP cleavage by host proteases. This implies that enzymatic activation of EBOV-GP may be a prerequisite for its entry into host cells. Coincidentally, a variety of enveloped viruses exploit the host protease to regulate their cell entry and infection (*13*). Targeting of host protease could lead to a useful strategy for treating infections with some enveloped viruses.

In general, the observation of these detailed mechanisms of EBOV

interaction with receptors opens the avenues to understanding that enveloped viruses employ different host factors to attach to the host cell surface. The discovery of PS as a viral attachment factor will be extended to other enveloped viruses that may be broad targets of this category of viruses. In addition, EBOV uses various host proteases to modify itself to facilitate entry into host cells, providing valuable insights into how enveloped viruses manipulate host functions to cause infection. However, as the real EBOV must be conducted in a biosafety level 4 laboratory, the generalizability of this work is limited to virus-like particles.

5.2 Fusion domain binding to host membrane: insights for enveloped viruses

After attaching to the surface of the host cell, the virus must release its genome into the cell to continue its replication and transcription. This process is initiated in enveloped viruses by the successful fusion of the virus and host cell membranes. Membrane fusion requires the overcoming of a high thermodynamic barrier in the merging of two plasma membranes. Enveloped viruses overcome the energetic barrier by storing kinetic energy in fusion proteins that release energy through a conformational transition, allowing direct fusion between the two bilayers. The fusion protein adopts an intermediate conformation during the conformational transition, exposing a fusion peptide (FP) to bind to the cell membrane and bridge the viral and cellular membranes. The interaction between FP and the host membrane is the foundation for the fusion of the viral membrane. Understanding this interaction will provide new insights into the mechanisms of enveloped viral entry and raise hopes for better control of infections through new vaccines and inhibitors.

In the second investigation within this thesis (**details in chapter 4**), we assessed how SARS-CoV-2 FP interacts with a lipid membrane. Using a BLI experiment, we first demonstrated that the ability of SARS-CoV-2 FP to bind to lipid membranes was substantially enriched when an exposed N-terminus was present than when it was not. The results of AFM-based SMFS on the height clamp mode are consistent with the results of BLI, where the absence compared to the presence of an exposed N-terminus did not bind to the membrane. These data indicate that the exposed N-terminus plays a critical role in the binding of SARS-CoV-2 FP to the host

membrane. The SARS-CoV-2 fusion peptide sequence begins with an S2/S2′ cleavage site (R815) buried in S2 protein domains that are required for membrane fusion and are highly conserved in all genera of the coronavirus subfamily, including SARS-CoV, SARS-CoV-2, and MERS-CoV (*14, 15*). Previous studies have described that conformational changes in S by receptor binding lead to cleavage of the S2/S2′ site by TMPRSS2 or endosomal cathepsins to trigger exposure of the fusion peptide region and then promote membrane fusion (*16, 17*). Our findings complement this idea that the enhanced binding of FP to the host membrane is due to the exposed N-terminus.

Then, we observed that the exposed SARS-CoV-2 FP binds with high affinity (10-fold) to the cholesterol-containing lipid membrane, by contrast to the sphingomyelin membrane. More importantly, the binding of FP to the cholesterol membrane has a long lifetime at the single molecule level, suggesting that this interaction is highly stable. These observations showed that cholesterol increases the binding of FP to the host membrane. Membrane composition affects the membrane fusion of enveloped viruses by altering the organization and dynamics of both the host membrane and viral fusion peptides (*18, 19*). The results of viral membrane fusion in the model have thoroughly demonstrated the involvement of cholesterol in the membrane fusion of enveloped viruses (*20, 21*). Our findings shed new light on how cholesterol promotes membrane fusion of enveloped viruses by enhancing FP binding to the membrane. According to one theory, the effect of cholesterol can be transmitted in two ways: through its influence on general membrane properties or through the specific interaction of cholesterol with peptides (*19*). Our data indicate that the latter way is preferable, as cholesterol

increases the binding affinity of FP to the lipid membrane. Surprisingly, the infection assay of pseudo-typed viruses of SARS-CoV-2 shows that the infectivity is inhibited after the removal of cholesterol from the host membrane, suggesting that cholesterol is important for the infection of enveloped viruses. Identification of correlations between viral infection and cholesterol in membrane composition, i.e., increase in binding of fusion peptides to the membrane. Additionally, this could also explain why infection of many enveloped viruses depends on the cholesterol-rich region of the host cell (*22, 23*) and why cholesterol-modifying drugs can prevent SARS-CoV-2 infection (*24, 25*).

In addition to the direct effects of lipid composition, the structure of viral fusion peptides is an important element in membrane fusion because it determines the interaction of the peptides with the membrane and triggers a conformational change in the fusion protein that provides the energy required for viral membrane fusion. The full length of FP in SARS-CoV-2 contains 40 amino acid residues consisting of an internal disulfide bridge and three α-helices connected *via* a flexible linker (*26, 27*). In agreement with previous reports (*28, 29*), our results show that the internal disulfide bridge between Cys840 and Cys851 significantly enhances the interaction between FP and the lipid membrane. This may be due to that the disulfide bond stabilizes the helices of FP at the C-terminus, which are crucial for the binding of SARS-CoV-2 FP to cell membranes. Crucially, we have directly captured the binding of SARS-CoV-2 FP to the membrane at the single-molecule level and restructured the free energy landscape of these processes. Quantitative analysis of the kinetics and thermodynamics of fusion peptide interactions with a membrane can directly elucidate its functions. However, current research

is primarily based on molecular dynamics simulations or systematic experiments (*30*), and quantitative analysis of the kinetics and thermodynamics are not as well understood at the single-molecule level. Our research fills this gap, and this approach could allow us to efficiently analyze the free energy of peptides or proteins that bind to and insert into the membrane.

Moreover, a central question in the insertion of peptides into a membrane is whether the formation of a stable structure of the peptide occurs before or after its insertion into a membrane (*31*). Our findings suggest that a stable structure of SARS-CoV-2 FP is required for binding to the membrane, because its internal disulfide bridge, an important component of stable α-helices, promotes binding to the lipid membrane. This could be an extremely useful guide for the insertion and folding of membrane proteins, as their transmembrane domains often contain one or more α-helices (*32*). Further experimental studies with a range of transmembrane peptides in membrane proteins could lead to a definitive conclusion on the mechanisms of binding and folding of membrane proteins.

5.3 AFM-based SMFS technical viewpoint on the context of enveloped viruses

The entry of enveloped viruses is based on specific interactions between viruses and host cells. These interactions materialize as molecular forces (including hydrogen bonding, electrostatics, and hydrophobicity) at the level of individual molecules. They constitute the underlying physicochemical foundation for the molecular recognition that takes place between viruses and cells. Deciphering these interactions is a challenge that requires not only the development of creative tools but also the application of conceptual and mathematical frameworks that can analyze the thermodynamic and statistical principles of physics. State-of-the-art AFM technology enables the measurement and manipulation of the molecular interactions involved in the entry of enveloped viruses and provides the opportunity to study the different parameters of the early viral infection process with exceptional resolution at the single-molecule level. However, there are several challenges in applying the AFM-based single-molecule force spectroscopy (AFM-SMFS) to the entry of enveloped viruses. In the following, we discuss the experimental and theoretical framework for using AFM-SMFS to study and monitor interactions during the entry of the enveloped virus into cells.

To maintain the integrity of the membrane of enveloped viruses, experiment conditions must be carefully controlled during the purification process, including temperature, pH, and ions concentration of the buffer. In particular, the use of detergents is prohibited during purification, because they may damage the integral membrane of enveloped viruses by dissolving the membrane. The purified virus

particles should be stored at -80°C until use, and freezing should not be repeated.

One major challenge in applying AFM applied to enveloped viruses is the functionalization of the AFM tips with the virus particles, which is a key effect in ensuring individual interaction. Since this is a multi-step reaction with a PEG spacer as a tether to cross-link the virus particles to AFM tips. Each step should be carefully executed to ensure successful functionalization. To obtain the best results in the force curves and topography images, we should choose the AFM tip with a suitable spring constant and high resolution. As described in the results section, PFQNM-LC (live cells) and MSCT (model surface) are used in the binding of EBOV to receptors, while AC-40 is used to study the binding and embedding of FP to the lipid membranes.

Second, to estimate the interaction of a single enveloped virus with the receptors, the amount of virus particles at the AFM tip apex is regulated by adjusting the ratio of the virus to PEG spacer concentration. This depends also on the size of the AFM tip and the experimental requirements (*33*). Occasionally, we have to change the ratio based on the actual studies. If the accessibility of the interaction is limited by the orientation of the proteins or peptides, the oriented functionalization should be generated with a special tag. Examples include the immobilization of proteins with histidine tag using tetradentate chelation of Ni^{2+} ions, the 'click' reaction of alkyne-azide cycloaddition, and the formation of an amide bond with sortase A between the carboxyl group of the LPXTG motif and the amino group of glycine.

Additionally, when protease is involved in the functionalization of AFM tips, the activation of the enzyme should be ensured to achieve the

best reaction efficiency. For instance, sortase A and TMPRSS2 are used in the study of SARS-CoV-2 FP, while cathepsin-B, cathepsin-L, and tumor necrosis factor-converting enzymes are used in EBOV.

During AFM experiments, relevant physiological conditions should be maintained (pH, electrolyte, and temperature) and ensure that the sample remains unaltered over the timeframe of the experiments. While a lipid membrane may be stable for up to a week, the process of membrane degradation begins with its formation; therefore, it is recommended that the lipid membrane is imaged within three days. Within the context of a living cell, it becomes imperative to detect the presence of expressed receptors on the cell surface before initiating an AFM experiment, which can be done for example by combining AFM and confocal experiments. To keep cells alive, they must be maintained under physiological conditions—specifically, at 37°C, with 5% CO_2, and an approximate humidity level of 95%. This meticulous environmental control is necessary since the status of living cells is influenced by an array of both physical and chemical variables.

Interpreting virus-host cell interactions plays a fundamental part in nearly all virus infections, especially in the binding behavior of virions at the single-molecule or particle level. While the application of AFM-based SMFS in this field is still in its infancy, it already provided valuable results. Currently, there are several issues to consider when interpreting the experimental results of AFM-based SMFS. First, the data collected must be used to determine whether these interactions are specific or non-specific; normally, the interaction between a virus and its receptor is specific. Although a flexible elastic PEG linker that attaches the virus to the AFM tips helps to exclude certain non-specific adhesion over short

distances (*34, 35*), it is not sufficient to eliminate all background signals. To solve this problem, numerous control experiments should be performed to check for specific interactions, such as blocking experiments with free antibodies and enzyme cleavage. Second, a significant capability of AFM-based SMFS is to distinguish the monovalent or multivalent interactions of different viruses with their receptors and to discover the precise molecular mechanisms behind these differences. Indeed, as described in **Chapter 3**, the multivalent and high-affinity interactions can determine whether the virus is successfully able to infect the host cell. Third, SMFS was performed using two distinct AFM modes: FV on model surfaces and PFT on the living cells. The fundamental difference between these two modes, as discussed in **Chapter 1.2** and illustrated in **Chapter 3**, is the rate at which the cantilever approaches and retracts cycles, i.e. the loading rate is different. This explains why rupture events occur further from equilibrium on living cells when the virus binds to receptors, compared to the model surface. Furthermore, the diverse contact times between the tip and the surface prevent a straightforward comparison of binding probabilities between these two modes.

Finally, SMFS is used to extract kinetic and thermodynamic parameters that define the entry of enveloped viruses, which is necessary to perform quantitative analyses of their infection. In this work, we used the Bell-Evans model to fit the DFS data and the Bell or DHS model to fit the height clamp data, as described in **Chapter 3** and **Chapter 4**, respectively. A comparison of the DFS data obtained from an external force application with the lifetime data collected under height-clamp observes several differences. In the absence of the external force

application, the height clamp represents the equilibrium state or the near-equilibrium state of molecular interactions. Notably, the thermodynamics can be directly extracted from the force-lifetime data using DHS model. However, this only applies to circumstances involving the binding, folding, or insertion of proteins and peptides into membranes. The kinetic analysis of the DFS data using the Bell-Evans model remains valid for the broader virus-receptor interactions. Additionally, the extraction of the on-rate of kinetics is also another important aspect for binding of virus-receptor, as described in **Chapter 3**. The evaluation of on-rate depends on the size of AFM tips, the length of the PEG linker, and the size of the protein or virus, which determine the efficient volume and concentration of ligand-receptors interactions.

Overall, our protocol opens the door to a better understanding of the entry of various enveloped viruses. We anticipate that this protocol can be used to study how other enveloped viruses interact with their host cells and that this knowledge will contribute to the development of vaccines and treatments for diseases caused by enveloped viruses.

While AFM-based single-virus and single-molecule force spectroscopy methods offer numerous advantages for investigating the interactions of viral glycoproteins, they also come with inherent limitations. First and foremost, one challenge is the difficulty in precisely controlling the density of chemical reagents applied to the surface of AFM tips. Consequently, it's possible that more than one molecule or virus may be present at the apex of the AFM tips. As mentioned earlier, despite various strategies employed to mitigate this issue, AFM-based single-molecule experiments may still encounter occasional complications due to this limitation.

Another crucial consideration when studying single-molecule interactions is the density of receptors on the model or cellular surface. This density is often constrained by the methods used for surface preparation in model systems or the exogenous expression on cellular surfaces. To enhance the credibility and reproducibility of single-molecule experiments, it becomes imperative to conduct repeated experiments and explore alternative assays.

Furthermore, it's important to note that AFM alone cannot identify specific molecules or their functional signaling events within cells. To address this limitation, researchers commonly employ complementary techniques and strategies alongside AFM, such as fluorescence microscopy and molecular and cellular methods.

Additionally, the adoption of single-molecule measurements using AFM is limited due to the specialized equipment required and the higher technical expertise involved, which can act as barriers to wider acceptance within the molecular bioscience community. Nevertheless, we remain optimistic that as researchers work to overcome these limitations, this technique will make significant contributions to our understanding of biological mechanisms and the development of stable therapeutics based on biophysics in the future.

5.4 Reference

1. C. P. Alvarez *et al.*, C-type lectins DC-SIGN and L-SIGN mediate cellular entry by Ebola virus in cis and in trans. *J Virol* **76**, 6841-6844 (2002).

2. A. S. Kondratowicz *et al.*, T-cell immunoglobulin and mucin domain 1 (TIM-1) is a receptor for Zaire Ebolavirus and Lake Victoria Marburgvirus. *Proc Natl Acad Sci U S A* **108**, 8426-8431 (2011).

3. H. Feinberg, D. A. Mitchell, K. Drickamer, W. I. Weis, Structural Basis for Selective Recognition of

Oligosaccharides by DC-SIGN and DC-SIGNR. *Science* **294**, 2163-2166 (2001).

4. W. Peng *et al.*, Glycan shield of the ebolavirus envelope glycoprotein GP. *Communications Biology* **5**, 785 (2022).

5. A. Takada *et al.*, Human macrophage C-type lectin specific for galactose and N-acetylgalactosamine promotes filovirus entry. *J Virol* **78**, 2943-2947 (2004).

6. M. Thépaut *et al.*, DC/L-SIGN recognition of spike glycoprotein promotes SARS-CoV-2 trans-infection and can be inhibited by a glycomimetic antagonist. *PLOS Pathogens* **17**, e1009576 (2021).

7. M. K. Callahan *et al.*, Phosphatidylserine on HIV Envelope Is a Cofactor for Infection of Monocytic Cells1. *The Journal of Immunology* **170**, 4840-4845 (2003).

8. L. Meertens *et al.*, The TIM and TAM Families of Phosphatidylserine Receptors Mediate Dengue Virus Entry. *Cell Host & Microbe* **12**, 544-557 (2012).

9. P. T. Ivanova *et al.*, Lipid Composition of the Viral Envelope of Three Strains of Influenza Virus—Not All Viruses Are Created Equal. *ACS Infectious Diseases* **1**, 435-442 (2015).

10. S. Wang *et al.*, AXL is a candidate receptor for SARS-CoV-2 that promotes infection of pulmonary and bronchial epithelial cells. *Cell Research* **31**, 126-140 (2021).

11. S. Jemielity *et al.*, TIM-family Proteins Promote Infection of Multiple Enveloped Viruses through Virion-associated Phosphatidylserine. *PLOS Pathogens* **9**, e1003232 (2013).

12. L. Baseler, D. S. Chertow, K. M. Johnson, H. Feldmann, D. M. Morens, The Pathogenesis of Ebola Virus Disease. *Annual Review of Pathology: Mechanisms of Disease* **12**, 387-418 (2017).

13. G. Izaguirre, The Proteolytic Regulation of Virus Cell Entry by Furin and Other Proprotein Convertases. *Viruses* **11**, 837 (2019).

14. K. W. Ng *et al.*, Preexisting and de novo humoral immunity to SARS-CoV-2 in humans. *Science* **370**, 1339-1343 (2020).

15. E. Shrock *et al.*, Viral epitope profiling of COVID-19 patients reveals cross-reactivity and correlates of severity. *Science* **370**, eabd4250 (2020).

16. M. Hoffmann *et al.*, SARS-CoV-2 Cell Entry Depends on ACE2 and TMPRSS2 and Is Blocked by a Clinically Proven Protease Inhibitor. *Cell* **181**, 271-280.e278 (2020).

17. M. A. Tortorici *et al.*, Ultrapotent human antibodies protect against SARS-CoV-2 challenge via multiple mechanisms. *Science* **370**, 950-957 (2020).

18. G. P. Pattnaik, H. Chakraborty, Cholesterol alters the inhibitory efficiency of peptide-based membrane fusion inhibitor. *Biochim. Biophys. Acta* **1861**, 183056 (2019).

19. G. Meher, H. Chakraborty, Membrane Composition Modulates Fusion by Altering Membrane Properties and Fusion Peptide Structure. *The Journal of Membrane Biology* **252**, 261-272 (2019).

20. G. Meher, S. Sinha, G. P. Pattnaik, S. Ghosh Dastidar, H. Chakraborty, Cholesterol Modulates Membrane Properties and the Interaction of gp41 Fusion Peptide To Promote Membrane Fusion. *The*

Journal of Physical Chemistry B **123**, 7113-7122 (2019).

21. K. N. Liu, S. G. Boxer, Target Membrane Cholesterol Modulates Single Influenza Virus Membrane Fusion Efficiency but Not Rate. *Biophysical Journal* **118**, 2426-2433 (2020).

22. I. Ripa, S. Andreu, J. A. López-Guerrero, R. Bello-Morales, Membrane Rafts: Portals for Viral Entry. *Frontiers in Microbiology* **12**, (2021).

23. R. Kulkarni, E. A. C. Wiemer, W. Chang, Role of Lipid Rafts in Pathogen-Host Interaction - A Mini Review. *Front. Immunol.* **12**, (2022).

24. R. Zang *et al.*, Cholesterol 25-hydroxylase suppresses SARS-CoV-2 replication by blocking membrane fusion. *Proceedings of the National Academy of Sciences* **117**, 32105-32113 (2020).

25. N. M. Schmidt, P. A. C. Wing, J. A. McKeating, M. K. Maini, Cholesterol-modifying drugs in COVID-19. *Oxford Open Immunology* **1**, (2020).

26. Y. Cai *et al.*, Distinct conformational states of SARS-CoV-2 spike protein. *Science* **369**, 1586-1592 (2020).

27. G. Khelashvili, A. Plante, M. Doktorova, H. Weinstein, Ca2+-dependent mechanism of membrane insertion and destabilization by the SARS-CoV-2 fusion peptide. *Biophysical Journal* **120**, 1105-1119 (2021).

28. H. Shen, Z. Wu, Effect of Disulfide Bridge on the Binding of SARS-CoV-2 Fusion Peptide to Cell Membrane: A Coarse-Grained Study. *ACS Omega* **7**, 36762-36775 (2022).

29. S. L. Schaefer, H. Jung, G. Hummer, Binding of SARS-CoV-2 Fusion Peptide to Host Endosome and Plasma Membrane. *The Journal of Physical Chemistry B* **125**, 7732-7741 (2021).

30. G. Enkavi, M. Javanainen, W. Kulig, T. Róg, I. Vattulainen, Multiscale Simulations of Biological Membranes: The Challenge To Understand Biological Phenomena in a Living Substance. *Chemical Reviews* **119**, 5607-5774 (2019).

31. S. H. White, W. C. Wimley, Membrane protein folding and stability: physical principles. *Annu Rev Biophys Biomol Struct* **28**, 319-365 (1999).

32. L. Smalinskaitė, R. S. Hegde, The Biogenesis of Multipass Membrane Proteins. *Cold Spring Harb. Perspect. Biol.* **15**, (2023).

33. R. Newton *et al.*, Combining confocal and atomic force microscopy to quantify single-virus binding to mammalian cell surfaces. *Nature Protocols* **12**, 2275-2292 (2017).

34. Z. Tong, A. Mikheikin, A. Krasnoslobodtsev, Z. Lv, Y. L. Lyubchenko, Novel polymer linkers for single molecule AFM force spectroscopy. *Methods* **60**, 161-168 (2013).

35. L. Wildling *et al.*, Linking of Sensor Molecules with Amino Groups to Amino-Functionalized AFM Tips. *Bioconjugate Chemistry* **22**, 1239-1248 (2011).

Chapter 6:

Conclusions and outlook

The first goal of this thesis was to use AFM at the single-virus level to probe the interactions between EBOV and cell surface receptors and the involvement of host protease in the activation of viral glycoprotein (**Chapter 3**). We effectively identified TIM-1 and DC-SIGNR as attachment receptors of EBOV by quantitatively studying of these interactions when EBOV binds to them. We then extracted the kinetics and thermodynamics of the interactions and discovered that the two receptors bind EBOV to the cell surface with high affinity. Next, we verified the binding ability of EBOV to these two receptors directly on living cells. Furthermore, we also examined the effect of host proteases (cathepsin-B, cathepsin-L, and tumor necrosis factor-α converting enzyme) on the activation of the viral glycoprotein, which allows a more effective binding to facilitate successful viral entry. Remarkably, TIM-1 binds to either EBOV-GP or PS, thus acting as a dual-receptor for EBVO, with the latter being favored when GP is activated by enzymatic cleavage.

Another aim of the thesis was to study the binding of a fusion peptide (FP) of SARS-CoV-2 (**Chapter 4**). AFM was developed as a tool of force sensing (AFM-based SMFS in height-clamp mode), which was used to monitor the binding of SARS-CoV-2 FP. Using biolayer interferometry experiments and AFM-based SMFS in height-clamp mode, we demonstrated that cholesterol enhanced the binding of FP to the membrane compared to the sphingomyelin in lipid components. The enhancement was validated at the S2 subunit level, which contain the FP

fragment. Strikingly, we discovered that an internal disulfide bond in FP dramatically increased this binding to the membrane, which may be due to the fact that the disulfide bond strengthens the mechanical stability of the FP. Additionally, we also discovered that removing the cholesterol in the the target cell membrane can effectively inhibit the infection of pseudotyped SARS-CoV-2.

Overall, in this thesis, we have provided a comprehensive analysis of the various detailed processes that take place during the entry of enveloped viruses. From the attachment of EBOV to the host cell surface to the binding of the SARS-CoV-2 fusion peptide, these processes of enveloped viral entry are critical for their infection. The main focus of my thesis was to provide a detailed interpretation of these steps that can support the development of vaccines and antiviral agents against diseases caused by these viruses and to build a framework for understanding the infection of enveloped viruses. Of particular note is the fact that our research highlights the importance of the FP binding to the membrane, (**Chapter 4**). Surprisingly, this crucial discovery had previously been overlooked. We anticipate that these findings will help to better understand the interaction between FP and the host membrane, which could provide new hope for the therapy of enveloped viruses infection. In addition, the many theories and methods we have covered in this thesis will hopefully be applicable to other aspects of biology, such as virus-receptor binding, protein-protein interaction, and membrane protein insertion.

While AFM is a powerful tool for studying the intricate dynamic mechanisms of envelope virus invasion, it cannot be used to study every stage of the infection pathway due to its inherent limitations. Because

AFM is a surface analysis technology, it does not provide access to events occurring within cells. However, the majority of activities in the life cycle of enveloped viruses take place inside the cell. Therefore, new experimental techniques are needed that can be combined with AFM to study the mechanisms of viral infection in a subcellular environment and at high resolution to reveal the underlying mechanisms of viral infection. In one revealing example, fluidic force microscopy was used in conjunction with a fast-scanning confocal microscope to study the internalization of reoviruses. Binding of reoviruses to integrin promotes the recruitment of clathrin to induce uptake of reoviruses into host cells (*1*). In addition, super-resolution fluorescence microscopes are considered the most important complementary tools to follow internalization, transport, fusion, genome transport, assembly, and egress throughout the viral life cycle. These techniques include structured illumination microscopy (SIM), stimulated emission-depletion microscopy (STED), photoactivation localization microscopy (PALM), and stochastic optical reconstruction microscopy (STORM). This family has been extended to include higher resolution, even with sub-nanometer accuracy, thanks to the recently developed MINFLUX nanoscopy and DNA-PAINT technology. These techniques make it possible to map the spatial position of the molecules of interest and to follow the molecular trajectories of specific particles and extract quantitative information with unprecedented resolution (*2, 3*), which can be related to the biophysical parameters detected by AFM. Furthermore, coupling these techniques with deep learning algorithms based on artificial intelligence will provide researchers with powerful tools to gain valuable new insights into enveloping virus infection. Finally, molecular dynamics simulations are increasingly being used to complement such experiments to better

understand atomic-level mechanisms, such as membrane fusion of the enveloped virus.

Reference

1. M. Koehler *et al.*, Reovirus directly engages integrin to recruit clathrin for entry into host cells. *Nature Communications* **12**, 2149 (2021).

2. M. Lelek *et al.*, Single-molecule localization microscopy. *Nature Reviews Methods Primers* **1**, 39 (2021).

3. M. Arista-Romero, S. Pujals, L. Albertazzi, Towards a Quantitative Single Particle Characterization by Super Resolution Microscopy: From Virus Structures to Antivirals Design. *Frontiers in Bioengineering and Biotechnology* **9**, (2021).

Appendix

Molecular interaction and inhibition of SARS CoV-2 binding to the ACE2 receptor

Jinsung Yang[1,4], Simon J. L. Petitjean[1,4], Melanie Koehler[1], **Qingrong Zhang**[1], Andra C. Dumitru[1], Wenzhang Chen[2], Sylvie Derclaye[1], Stéphane P. Vincent [2], Patrice Soumillion[1] & David Alsteens[1,3]

Nature Communications (2020)

https://www.nature.com/articles/s41467-020-18319-6

I contributed to this work by performing molecular dynamic simulations and structure predictions.

nature COMMUNICATIONS

ARTICLE

https://doi.org/10.1038/s41467-020-18319-6 OPEN

Molecular interaction and inhibition of SARS-CoV-2 binding to the ACE2 receptor

Jinsung Yang[1,4], Simon J. L. Petitjean[1,4], Melanie Koehler[1], Qingrong Zhang[1], Andra C. Dumitru[1], Wenzhang Chen[2], Sylvie Derclaye[1], Stéphane P. Vincent[2], Patrice Soumillion[1] & David Alsteens[1,3]✉

Study of the interactions established between the viral glycoproteins and their host receptors is of critical importance for a better understanding of virus entry into cells. The novel coronavirus SARS-CoV-2 entry into host cells is mediated by its spike glycoprotein (S-glycoprotein), and the angiotensin-converting enzyme 2 (ACE2) has been identified as a cellular receptor. Here, we use atomic force microscopy to investigate the mechanisms by which the S-glycoprotein binds to the ACE2 receptor. We demonstrate, both on model surfaces and on living cells, that the receptor binding domain (RBD) serves as the binding interface within the S-glycoprotein with the ACE2 receptor and extract the kinetic and thermodynamic properties of this binding pocket. Altogether, these results provide a picture of the established interaction on living cells. Finally, we test several binding inhibitor peptides targeting the virus early attachment stages, offering new perspectives in the treatment of the SARS-CoV-2 infection.

[1] Louvain Institute of Biomolecular Science and Technology, Université Catholique de Louvain, Louvain-la-Neuve, Belgium. [2] Département de Chimie, Laboratoire de Chimie Bio-Organique, University of Namur, Namur, Belgium. [3] Walloon Excellence in Life sciences and Biotechnology (WELBIO), 1300 Wavre, Belgium. [4] These authors contributed equally: Jinsung Yang, Simon J. L. Petitjean. ✉email: david.alsteens@uclouvain.be

In December 2019, a novel coronavirus (CoV) was determined to be responsible for an outbreak of potentially fatal atypical pneumonia, ultimately defined as coronavirus disease-19 (COVID-19), in Wuhan, China. This novel CoV, termed severe acute respiratory syndrome (SARS)-CoV-2, was found to share similarities with the SARS-CoV that was responsible for the SARS pandemic that occurred in 2002. The resulting outbreak of COVID-19 has emerged as a severe pandemic. The genome of SARS-CoV-2 shares about 80% identity with that of SARS-CoV and is about 96% identical to the bat coronavirus BatCoV RaTG13 (ref. [1]).

CoV entry into host cells is mediated by its transmembrane spike (S) glycoprotein that forms homotrimers protruding from the viral surface[2] (Fig. 1a). The S glycoprotein comprises two functional subunits responsible either for binding to the host cell receptor (S1 subunit including the receptor-binding domain (RBD)) or for fusion of the viral and cellular membranes (S2 subunit). Recent studies claimed that the angiotensin-converting enzyme 2 (ACE2), previously identified as the cellular receptor for SARS-CoV, also acts as a receptor of the new coronavirus (SARS-CoV-2)[3] (Fig. 1b). In the case of SARS-CoV, the S glycoprotein on the virion surface mediates receptor recognition (Fig. 1c) and membrane fusion[4,5]. Recently, the high-resolution cryo-electron microscopy structure obtained on the full-length human ACE2 in the presence of the RBD of the S glycoprotein of SARS-CoV-2 suggests simultaneous binding of two S-glycoprotein trimers to an ACE2 dimer[3]. The S2 subunit is further cleaved by host proteases located immediately upstream of the fusion peptide[6], leading to the activation of the glycoprotein that undergoes extensive irreversible conformational changes facilitating the membrane fusion process. Altogether, the information obtained so far highlights the fact that CoV entry into susceptible cells is a complex process that requires the concerted action of receptor binding and proteolytic activation of the S glycoprotein at the host cell surface to finally promote virus–cell membrane fusion. However, so far, direct evidence about the dynamics of the binding of the S1- to the ACE2 receptor at the single-molecule level is missing.

Here, we analyze the biophysical properties of the SARS-CoV-2 S-glycoprotein binding, on model surfaces and on living cells, to ACE2 receptors using force–distance (FD) curve-based atomic force microscopy (FD-curve-based AFM) (Fig. 1c). We extract the kinetics and thermodynamics of the interactions established in vitro, and compare the binding properties of both the S1 subunit and RBD. Next, we test short ACE2-derived peptides targeting the viral S glycoprotein as potent binding inhibitor peptides and observe a significant reduction in the binding properties.

Results

S1 subunit specifically binds to purified ACE2 receptors. As SARS-CoV-2 binding to ACE2 receptors is thought to play a key role in the first binding step at the cellular membrane[3], we first

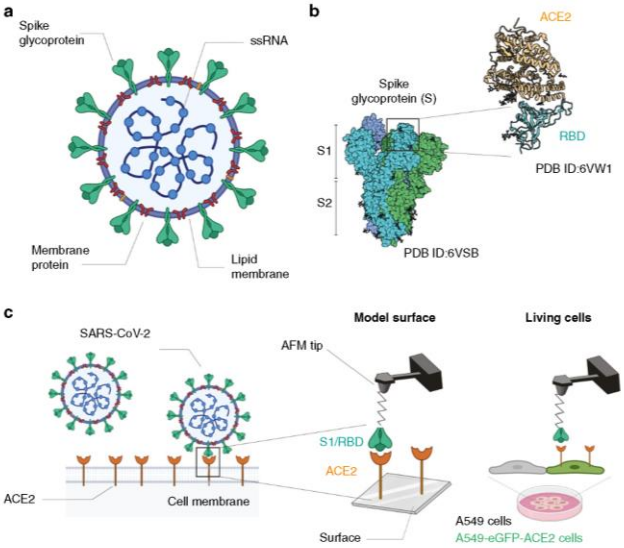

Fig. 1 Probing SARS-CoV-2 binding to the ACE2 host receptor. a Schematic of a SARS-CoV-2 particle, an enveloped ssRNA virus expressing at its surface the spike glycoprotein (S) that mediates the binding to host cells. **b** Structural studies have previously obtained a complex between the receptor-binding domain (RBD, a subunit of the S glycoprotein) and the angiotensin-converting enzyme 2 (ACE2) receptor. **c** Schematic of probing SARS-CoV-2 binding using atomic force microscopy (AFM). The initial attachment of SARS-CoV-2 to cells involves specific binding between the viral S glycoprotein and the cellular receptor, ACE2. The interactions are monitored by AFM on model surfaces, where the ACE2 receptor is attached to a surface and the S1 subunit or the RBD onto the AFM tip, and on A549 living cells expressing or not fluorescently labeled ACE2.

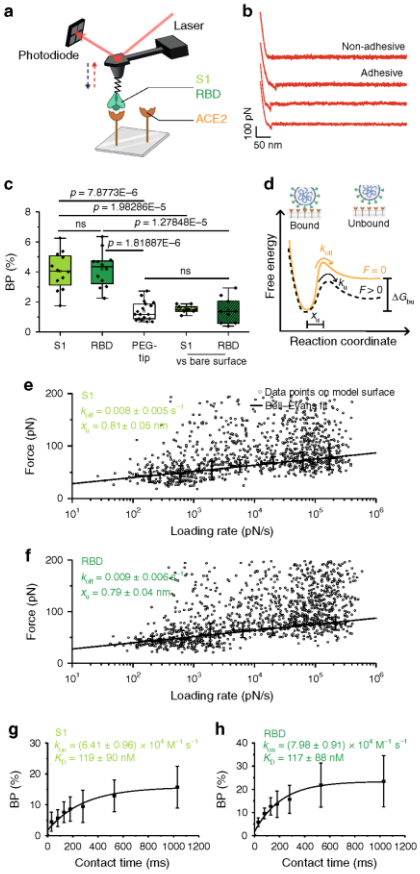

Fig. 2 Probing S-glycoprotein binding to the ACE2 host receptor on model surface. a Binding of S-glycoprotein subunit (S1 or RBD) is probed on an ACE2-coated surface. **b** Retraction part of four force–distance curves showing either nonadhesive or specific adhesive curves. **c** Box plot of specific binding probabilities (BP) measured by AFM between the functionalized tip (S1, RBD, or PEG) and the grafted surface (ACE2 or OH-/COOH-terminated alkanethiol (bare surface)). One data point belongs to the BP from one map acquired at 1 µm/s retraction speed. The square in the box indicates mean, the colored box indicates the 25th and 75th percentiles, and the whiskers indicate the highest and the lowest values of the results. The line in the box indicates median. $N = 12$ (S1, RBD), 18 (PEG), and 9 (S1, RBD vs. bare surface) maps examined over 4 (S1, RBD), 6 (PEG), and 3 (S1, RBD vs. bare surface) independent experiments. **d** Bell–Evans model describing a virus-receptor bond as a two-state model. The bound state is separated from the unbound state by a single energy barrier located at distance x_u. k_{off} and k_{on} represent the dissociation and association rate, respectively. **e**, **f** Dynamic force spectroscopy (DFS) plot showing the distribution of the rupture forces as a function of their loading rate (LR) measured either between the S1 subunit and the ACE2 receptor ($N = 1052$ data points) (**e**) or between the RBD and the ACE2 receptor ($N = 1490$ data points) (**f**). The error bar indicates s.d. of the mean value for a single interaction (0–200 pN). The solid line represents the fit of the data with the Bell–Evans fit. Experiments were reproduced at least four times with independent tips and samples. **g**, **h** The BP is plotted as a function of the contact time for S1 subunit and RBD on ACE2 model surfaces, and data points were fitted using a least-squares fit of a monoexponential growth. One data point belongs to the BP from one map acquired at 1 µm/s retraction speed for the different contact times. Experiments were reproduced three times with independent tips and samples. *P* values were determined by two-sample *t* test in Origin. The error bar indicates s.d. of the mean value. Source data are provided as a Source Data file.

used FD-curve-based AFM to evaluate at the single-molecule level the binding strength of the interaction established between the glycosylated S1 subunit and ACE2 receptors on model surfaces (Fig. 2a). To mimic cell-surface receptors in vitro, ACE2 receptors were covalently immobilized onto gold surfaces coated with OH- and COOH-terminated alkanethiols using carbodiimide conjugation (see Methods). These model surfaces were imaged by AFM, and the thickness of the grafted layer was validated by a scratching experiment, revealing a deposited layer of 6.1 ± 0.4 nm (mean ± S.D., $N = 3$) (see Methods and Supplementary Fig. 1). To study the interaction between the S1 subunit and the immobilized ACE2 receptors, we covalently grafted either the purified full S1 subunit or RBD only to the free end of a long polyethylene glycol $(PEG)_{24}$ spacer attached to the AFM tip[7–9]. To investigate the properties of the binding complex, force–distance (FD) curves were recorded by repeatedly approaching and withdrawing the S1 subunit or RBD- functionalized tip from the ACE2 model surface (Fig. 2a, b). Specific adhesion events were observed on 4–5% of the retraction FD curves at rupture distances >15 nm, which corresponds to the extension of the PEG linker (Fig. 2c and Supplementary Fig. 2), and is in line with studies carried out for other virus–cell-surface receptor systems[8,10–12]. To confirm the specificity of these interactions, we conducted additional independent control experiments using (i) an AFM tip only functionalized with the PEG linker or (ii) toward OH-/COOH-terminated alkanethiol surfaces missing the receptor. The binding frequency observed during those control experiments is significantly lower, thereby confirming the specificity of the S1 subunit/RBD–ACE2 complexes under our experimental conditions (Fig. 2c).

Exploring the dynamics of S1 subunit–ACE2 interaction. Single-molecule force-probing techniques, such as FD-based AFM, measure the strength of a bond under an externally applied force, enabling to get insights into the binding free-energy landscape. According to the Bell–Evans model[13,14], an external force stressing a bond reduces the activation-energy barrier toward dissociation and, hence, reduces the lifetime of the ligand-receptor pair[15] (Fig. 2d). The model also predicts that far-from-equilibrium, the binding strength of the ligand-receptor bond is proportional to the logarithm of the loading rate (LR), which describes the force applied on the bond over time. To investigate the kinetics of the probed complex, FD curves were recorded at various retraction rates and contact times (Fig. 2e–h). Dynamic force spectroscopy (DFS) plots were obtained for both S1 subunit (Fig. 2e) and RBD (Fig. 2f) binding toward immobilized ACE2 receptors. In each case, the unbinding force increases linearly with the logarithm of the LR, as observed earlier for other

virus-receptor bonds[8,10,11,16,17]. To determine whether single- or multiple-bond rupture between S1/RBD and ACE2 is taking place, bond strengths (every single gray data point in Fig. 2e, f) were analyzed through distinct discrete ranges of LRs, plotted as force histograms and further fitted with multipeak Gaussian distribution, as established previously[11,16] (Supplementary Figs. 3 and 4). Using this distribution, we are able to determine the most probable unbinding force of each force peak (maximum of rupture force distribution; black dots plotted over mean LR of this range in Fig. 2e, f), and can determine if single or multiple interactions were taking place. The presence of multiple parallel unbinding events is first observed in the distribution of rupture forces with the presence of multiple Gaussian fits. The histograms show that most probably only single interactions were taking place; thus, the Bell–Evans model[15] was used to fit the data enabling to interpret the binding complex as a simple two-state model, in which the bound state is separated from the unbound state by a single energy barrier (Fig. 2d). From the slope of the fit, we estimated the length scale of the energy barrier (x_u). We obtained very close values, $x_u = 0.81 \pm 0.05$ nm and 0.79 ± 0.04 nm for both the S1 subunit and RBD, showing that we are probing similar bonds (Fig. 2e, f). The kinetic off-rate (k_{off}) or dissociation rate is obtained from the intercept of the fit (at LR = 0) yielding k_{off} values of $0.008 \pm 0.005\ s^{-1}$ and $0.009 \pm 0.006\ s^{-1}$ for S1 subunit and RBD, respectively. These values are in good agreement with reported values obtained by surface plasmon resonance for the S glycoprotein ($k_{off} = 0.003\ s^{-1}$)[18] and the RBD subunit ($k_{off} = 0.008\ s^{-1}$) binding to ACE2 receptors[19].

Assuming that the receptor-bond complex can be approximated by a pseudo-first-order kinetics, we also estimated the kinetic on-rate (k_{on}) from our single-molecule force spectroscopy experiments[11] (Fig. 2g, h). This association rate is extracted from the binding probability (BP) measured at various contact times, and depends on the effective concentration described as the number of binding partners (ligand + receptor) within an effective volume V_{eff} accessible under free-equilibrium interaction. V_{eff} can be approximated by a half-sphere with a radius including the linker, the viral glycoprotein (S1 subunit or RBD) and the ACE2 receptor. For both the S1 subunit and RBD, we observed that the binding frequency increased exponentially with contact time, and we extracted an interaction time of ~0.250 ms, leading to a k_{on} of $6.4 \times 10^4\ M^{-1}\ s^{-1}$ and $8.0 \times 10^4\ M^{-1}\ s^{-1}$, respectively. Finally, the dissociation constant K_D is calculated as the ratio between the k_{off} and the k_{on}, yielding values around ~120 nM for both complexes. This value corresponds to a high-affinity interaction, confirming the specificity of the complexes established by SARS-CoV-2 with the ACE2 cell-surface receptor, which in turn results in a long lifetime of the virus attachment to the cell surface. Other interaction studies between SARS-CoV (80% sequence homology to SARS-CoV-2) and ACE2 reported specific, high-affinity association values also in the nM range[20]. For comparison, a variety of examples for low- as well as high-affinity interactions between other virus-receptor pairs are summarized in Dimitrov et al.[21] and include influenza A—SA (mM) or HIV-1—CD4 (nM) interactions. For single-molecule interactions, the bond lifetime τ can be directly related to the inverse kinetic off-rate ($\tau = k_{off}^{-1}$), resulting here in a τ of 125 ms for the S1 subunit and 111 ms for the RBD, respectively. Of course, at the virion level, the overall bond lifetime will increase with the multivalence of the interaction. By definition, high-affinity interaction has a long lifetime as the dissociation constant K_D is defined as the ratio between k_{off} and k_{on}. For high-affinity interactions, the K_D is in the nM range, leading to $k_{off} \ll k_{on}$ and therefore maintaining the interaction in its bond state for very long times, making the development of anti-binding molecules targeting this interaction more difficult. Finally, we also used optical biolayer interferometry (BLI) to confirm the kinetic parameters characterizing this interaction, and obtained very close affinities in the same nM range as AFM experiments (Supplementary Fig. 5). Taken together, our in vitro experiments confirm that SARS-CoV-2 binding to the ACE2 receptors is mediated by the RBD–ACE2 interface as our experimental conditions did not highlight any significant difference between S1 subunit and RBD binding.

Validation of the interaction on living cells. Next, we wanted to investigate whether the interaction probed on isolated receptors is also established in physiologically relevant condition. To this end, we performed binding assays on living A549 cells (human adenocarcinoma alveolar basal epithelial cells). While this cell line is widely used as a type II pulmonary epithelial cell model, it has been shown recently that those cells are incompatible with SARS-CoV-2 infection[22]. Interestingly, ACE2 expression positively correlated with the differentiation state of epithelia. Although undifferentiated cells (cultured at low confluency) only express little ACE2, overexpression of ACE2 in undifferentiated A549 cells facilitated virus entry[23]. We transiently transfected ACE2–eGFP in A549 cells (A549–ACE2) and probed S1-subunit binding to those cells as well as to A549 cells (serving as internal control) (Fig. 3a and Supplementary Fig. 6). Confocal images showed ACE2–eGFP receptors homogeneously distributed in small domains at the surface of A549 cells (Fig. 3b). Guided by fluorescence (Fig. 3c), we chose areas in which both cell types, i.e., transfected (A549–ACE2, green fluorescence) and nontransfected (A549, no fluorescence) cells, were in proximity to one another. Having both A549 cell types in one image area served as a direct control to evaluate whether interactions measured by the functionalized tip were indeed due to specific binding to fluorescent ACE2–eGFP receptors, and to evaluate the extent of other types of interactions (Fig. 3c–e). In such area, we simultaneously recorded a height image (Fig. 3d) and the corresponding adhesion map (Fig. 3e), which were reconstructed from FD curves recorded for each topographic pixel. The retraction part of FD curves showed specific adhesion events mainly on A549–ACE2 cells, with a significantly higher BP (Fig. 3f), as exemplified with the presented adhesion map that shows 20.1% of adhesive pixels on the A549–ACE2 cell versus 13.5% on the control cells (Fig. 3e and Supplementary Fig. 7). Specific binding forces (and corresponding LR) were extracted from force vs. time curves recorded on A549–ACE2 cells (Fig. 3g) and overlaid on the DFS plot obtained on purified ACE2 receptors (Fig. 3h). To explore a wide range of LR, we probed the interaction at various frequencies and amplitudes (see Methods). We observed a very good alignment between the data obtained on purified receptors and on living cells confirming the physiological relevance of our results obtained on model surfaces.

S1 subunit binding to the cell involves other receptors. Our FD-based AFM experiments performed on living cells put in evidence that the S1 subunit interacts even on control cells with a frequency ≈10% although the expression level of ACE2 should be very low as the cells are not differentiated. Nevertheless, some evidence pointed out that human CoV S glycoproteins possess sialic acid (SA)-binding sites and in particular to 9-O-acetyl-sialogycans[24], and that integrins could also be a receptor for the SARS-CoV-2 (ref. [25]), which possesses a RGD motif close to the ACE2-binding site. To evaluate whether these other receptors could be involved during the early binding steps to the cell surface, we performed additional experiments by injecting 9-O-acetyl-sialogycans to block interaction with cell-surface SA, or added cyclo-RGD (cRGD) to compete with the interactions with

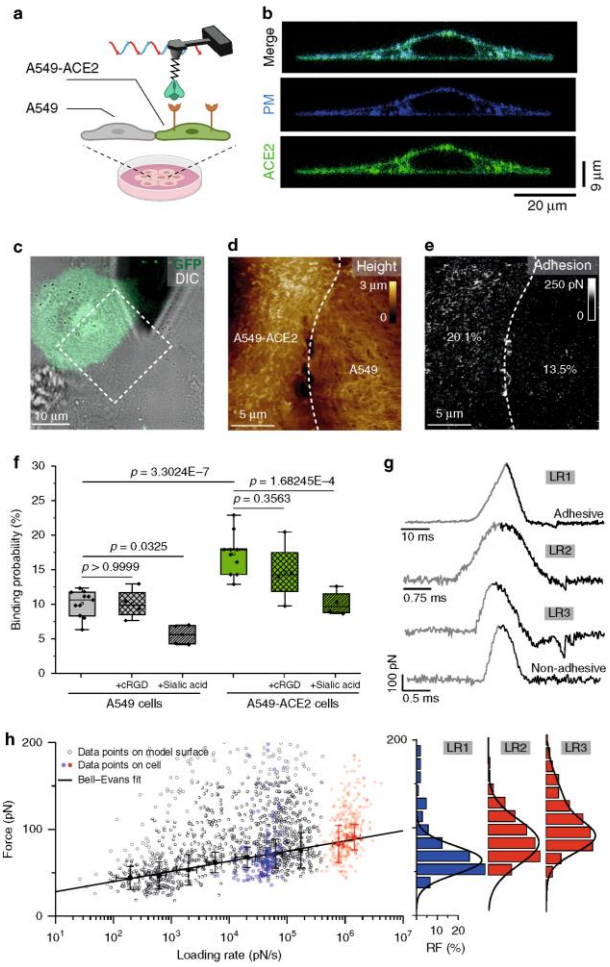

integrins. After SA injection, the binding frequency was reduced on A549 cells down to ~7% and to ~10% on ACE2-transfected cells (Fig. 3f and Supplementary Fig. 8). For integrins, injection of cRGD only reduces the binding frequency of ~1–2% on both cell types, which is in good agreement with the fact that integrins are mostly expressed on the bottom of the cell[26]. Altogether, these data obtained on cells by AFM represent to date the best evidence that S1–ACE2 complex is established in physiologically relevant conditions and underlines the complex situation with multiple cell-surface receptors accounting for the whole interaction.

Inhibition of S1-subunit binding using ACE2-derived peptides. Human recombinant soluble ACE2 (hrsACE2) is currently being considered for treatment of COVID-19 (refs. [27,28]). However, ACE2 is involved in many key cellular processes, such as blood-pressure regulation and other cardiovascular functions. Therefore, hrsACE2 treatment could lead to dysregulation of those vital processes and subsequently cause deleterious side effects for treated patients. To avoid any interference of the ACE2 homeostasis, we wanted to test whether small ACE2-derived peptides can also interfere with SARS-CoV-2 binding, by blocking binding

Fig. 3 Probing S-glycoprotein binding to the ACE2 host receptor on living cells. a Binding of S-glycoprotein subunit 1 (S1) is probed on A549 and A549–ACE2 cells. **b** Confocal microscopy (z stack) of A549–ACE2–eGFP (green) cell transduced with plasma membrane BFP (blue). **c** Overlay of eGFP and DIC images of a mixed culture of A549 and A549–ACE2–eGFP cells. **d**, **e** Force–distance (FD)-based AFM topography image (**d**) and the corresponding adhesion map (**e**) in the specified area in (**c**). The frequency of adhesion events is indicated. **f** Box plot of the binding probability between S1 and A549 cells (gray) or A549–ACE2 cells (green) without and after injection of cyclic RGD (cRGD, checked boxes) or sialic acid (SA, dashed boxes), respectively. The square in the box indicates mean, the colored box indicates the 25th and 75th percentiles, and the whiskers indicate the highest and the lowest values of the results. The line in the box indicates median. **g** Force versus time curves showing either a nonadhesive curve (bottom) or specific adhesive curves acquired at different LRs (LR1–LR3). **h** DFS plot showing the distribution or the rupture forces measured either between the S1 subunit and the ACE2 on model surfaces (black dots, extracted from Fig. 2e), and between the S1 subunit and ACE2-overexpressing A549 cells acquired at three different LRs (blue and red dots) ($N = 403$). Blue dots belong to a data set acquired in fast-force volume mode, with a retraction velocity of 20 $\mu m\,s^{-1}$ (LR1). Red dots belong to data sets acquired in peak force tapping mode with 0.125 kHz peak force frequency and 375-nm amplitude (LR2) or at 0.25 kHz and 750 nm (LR3), respectively. The error bar indicates s.d. of the mean value. Histograms of force distribution on A549–ACE2 cells for LR1–LR3 are shown on the side. For experiments without injection of cRGD or SA, data are representative of at least $N = 11$ cells from $N = 6$ independent experiments. The data for blocking experiments with cRGD or SA were acquired for at least $N = 4$ cells from $N = 2$ independent experiments. *P* values were determined by two-sample *t* test in Origin. Source data are provided as a Source Data file.

sites on the S glycoprotein. To this end, we synthetized four different peptides (sequences provided in Supplementary Fig. 9), which have been selected to mimic the regions of ACE2 that interact with the S1 subunit as determined by the crystal structure[29], and we tested their binding inhibition properties using our single-molecule force spectroscopy approach (Fig. 4a, b). We first measured the BP between the S1 subunit and the ACE2 in the absence of peptide (0 µM), with a contact time of 250 ms, as reference, and then injected our ACE-derived peptides at three different concentrations (1, 10, and 100 µM). For the four peptides, we observed a progressive reduction of the BP as a function of the concentration confirming a specific inhibition. In addition, for each peptide, we noticed a reduction of >50% of the probed interactions already for the 1–10 µM concentration, suggesting a 50% inhibitory concentration (IC_{50}) in the µM range. The [22–44] peptide shows the highest inhibition of the S1–ACE2 complex formation with a measured reduction in the BP of ~76%. The [22–57] peptide shows a similar inhibition potential (~74%), suggesting that the additional amino acids do not influence the overall affinity of the peptide for the S1 subunit, as also confirmed by molecular dynamics (MD) simulations showing that although the peptide 22–57 is longer, less H bonds are established between the peptide and the RBD domain (Supplementary Fig. 10). Overall, these results are in good agreement with the structural insights because these peptides are derived from the *N*-terminal helix of the ACE2 and therefore form with the RBD interface an important network of hydrophilic interactions (including nine hydrogen bonds and a salt bridge). Within the ACE2–RBD complex, the [351−357] fragment is also part of a "hot binding spot" that results in our test by a good score with a reduction of ~60% of the initial specific BP. Finally, the [22–44–g–351–357] peptide was also synthetized and tested based on the fact that in the crystal structure, the distance between S44 and L351 is close enough to be filled by a single amino acid. A glycine residue was added between the two fragments because the two ACE2 fragments have opposite directionality, and glycine has a high propensity to form reverse turns. Nevertheless, under our experimental conditions, we did not notice any strong improvement in the binding inhibition. Altogether, our in vitro assays at the single-molecule level provide direct evidence that ACE2-derived peptides are strong candidates to potentially inhibit SARS-CoV-2 binding to ACE2 receptors (Fig. 4c).

ACE2-derived peptide blocks specific binding to living cells. Finally, we tested whether the [22−57]-binding inhibition peptide could also prevent S1-subunit binding in the cellular context (Fig. 5). The interaction between the S1 subunit and the confluent layer of a coculture of A549 and A549–ACE2 cells was probed before and after addition of the peptide at 100 µM. Before injection, cells overexpressing the ACE2 receptors (A549–ACE2) show higher BP (9.4 ± 1.6% vs. 19.4 ± 7.3%, for A549 and A549–ACE2, respectively) (mean ± S.D., $N = 4$) (Fig. 5a–d), in good agreement with our previous observation (Fig. 3f). After injection of the [22−57] ACE2-derived peptide, we observed a significant decrease of the BP on both cell types (Fig. 5e, f). In particular, the BP on A549–ACE2 cells significantly drops (~70%), reaching a level close to the one of the control cells. Taking into account that undifferentiated A549 cells express little ACE2 and are poorly infected by CoV[23], this result supports the biological relevance of our ACE2-derived peptide acting as potential inhibitor capable of efficiently blocking SARS-CoV-2 binding.

In conclusion, we investigated the interaction established between the SARS-CoV-2 S glycoprotein and the ACE2 receptor using single-molecule force spectroscopy. We demonstrated a specific binding mechanism between the S1 subunit and the ACE2 receptor. By comparing the binding of the S1 subunit and the RBD toward the ACE2 receptor, our experiment evidenced that both domains interact with the same kinetic and thermodynamic properties toward the ACE2 receptor, highlighting that SARS-CoV-2 binding to ACE2 is dominated by the RBD/ACE2 interface. Our measurements show that under our physiologically relevant conditions, the RBD binds the ACE2 receptor with an intrinsic high affinity (~120 nM), which could even be further stabilized at the whole-virus level, thanks to possible multivalent bonds between the S-glycoprotein trimer and ACE2 dimer.

Based on the available crystal structures of the molecular complex, we examined how several ACE2-derived peptide fragments could interfere with the S1–ACE2 complex formation. While all tested peptides show binding inhibition properties, peptides mimicking the N-terminal helix of the ACE2 receptor show the best results. Both [22–44] and [22–57] peptides exhibit an anti-binding activity with IC_{50} in the µM range, resulting in a >70% decrease in the BP observed by AFM on purified receptor and >70% on living cells. On the cellular model, we observed that the BP drops to the level of the control cells (undifferentiated A549 cells) that are poorly infected by CoV[23]. Therefore, those peptides appear as strong therapeutic candidates against the SARS-CoV-2 infection.

Methods

Cell culture and transfection. A549 cells (ATCC® CCL-185) were grown in Ham's F-12 Nutrient Mix with 10% fetal bovine serum, penicillin (100 U ml^{-1}), and streptomycin (100 µg mL^{-1}) (Gibco) at 37 °C in a humidified atmosphere with 5% CO_2. pcDNA3.1(+) ACE2–eGFP was transfected using Lipofectamine LTX (Invitrogen) according to the manufacturer's protocol. In brief, 2 µg of

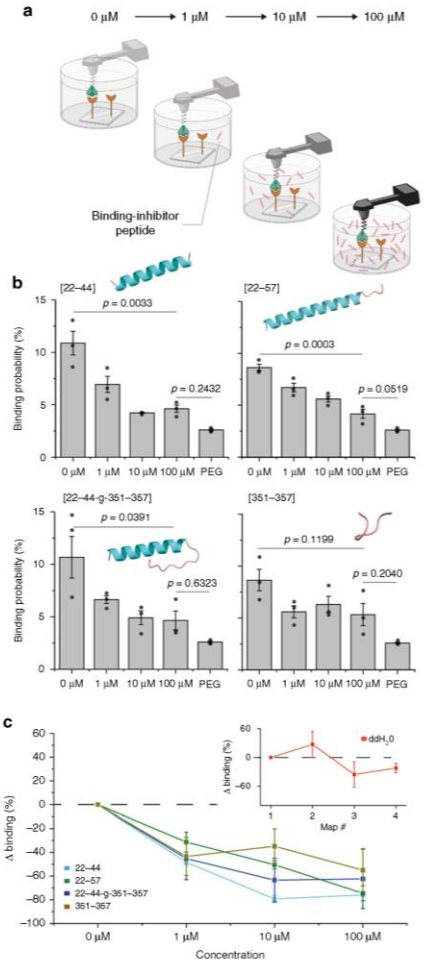

Fig. 4 Anti-binding effects of ACE2-derived peptides on S1-subunit binding. a Efficiency of blocking peptides is evaluated by measuring the binding probability of the interaction between the S1 subunit and ACE2 receptor on model surface before and after incubation of the functionalized AFM tip with the four different peptides at increasing concentration (1–100 µM). **b** Histograms, with the corresponding data points overlaid in dark gray, showing the binding probability without peptide (0 µM) and upon incubation with 1, 10, or 100 µM of ACE2-derived peptides ([22–44], [22–57], [22–44–g–351–357], and [351–357]). The binding probability measured with a polyethylene glycol (PEG) tip enables to evaluate the nonspecific binding level. The prediction of the structure of the ACE2-derived peptides is shown in the inset. The structure of the peptides is based on the structure of the peptide in the crystal structure (PDB ID: 6m0j). For the [22–44–g–351–357] peptide, its structure was generated using homology modeling[41]. The error bar indicates s.d. of the mean value. **c** Graph showing the reduction of the binding probability. Control with ddH_2O is provided in the inset showing that repetitive measurements do not result in a similar decrease of the binding probability. Data are representative of at least $N = 3$ independent experiments (tips and sample) per peptide concentration. *P* value was determined by two-sample *t* test in Origin. The error bar indicates s.d. of the mean value. Source data are provided as a Source Data file.

pcDNA3.1(+) ACE2–eGFP was transfected to A549 cells (60-mm plate) using 6 µl of Lipofectamine LTX and 2 µl of PLUS reagent (Invitrogen).

Functionalization of AFM tips. PFQNM-LC and MSCT-D cantilevers (Bruker) were used to probe the interaction between S1 subunit (Genscript, #U5377FC120) or RBD protein (Genscript, #U5377FC120) and ACE2 protein (Sino Biological, 90211-C02H). NHS-PEG_{24}-Ph-aldehyde linkers were used to functionalize AFM tips as previously described[30]. Briefly, the cantilevers were immersed in chloroform for 10 min and further cleaned in a UV radiation and ozone (UV-O) cleaner (Jetlight), and immersed overnight in an ethanolamine solution (3.3 g of ethanolamine in 6.6 ml of DMSO). They were washed with DMSO and ethanol three times, respectively. Ethanolamine-coated cantilevers were immersed in NHS-PEG_{24}-Ph-aldehyde solution (3.3 mg of it was diluted in 0.5 ml of chloroform and 30 µl of triethylamine) and finally washed 3 times with chloroform and dried with nitrogen.

For AFM tips functionalized with S1-subunit protein, 50 µl of S1-subunit protein solution (0.1 mg/ml) was put onto the cantilevers placed on Parafilm (Bemis NA) and 2 µl of fresh $NaCNBH_3$ solution (6 wt% vol-1 in 0.1 M NaOH(aq)) was mixed in the protein solution. The cantilevers were incubated in the solution for 1 h on ice. Then, 5 µl of 1 M ethanolamine solution was carefully added to the protein solution and incubated 10 min to quench the reaction and finally washed three times with PBS.

For AFM tips derivatized with the RBD protein, 100 µl of a 100 µM tris-nitrilotriacetic amine 540 trifluoroacetate (Toronto Research Chemicals, Canada) (tris-NTA) solution was put onto them placed on Parafilm, and 2 µl of fresh $NaCNBH_3$ solution was mixed in the protein solution. They were incubated in the solution for 1 h on ice. Then, 5 µl of 1 M ethanolamine solution in the protein solution was added and incubated for 10 min. The mixture of 50 µl of RBD solution (0.1 mg ml^{-1}) and 2.5 µl of 5 mM $NiCl_2$ were put onto them and they were incubated for 2 h. After incubation, they were washed in PBS solution three times.

Preparation of ACE2-coated model surfaces. ACE2 protein (Sino Biological, 90211-C02H) was immobilized using NHS–EDC chemistry. Gold-coated surfaces were first rinsed with ethanol, dried with a gentle stream of nitrogen gas, cleaned for 15 min by UV and ozone treatment (Jetlight), and incubated overnight in an alkanethiol solution (99% 11-mercapto-1-undecanol 1 mM (Sigma Aldrich) and 1% 16-mercaptohexadecanoic acid 1 mM (Sigma Aldrich) in ethanol). The chemically activated samples were rinsed with ethanol, dried with nitrogen gas, and immersed for 30 min in the solution of 100 mg of chemically activated dimethylaminopropyl carbodiimide (Sigma Aldrich) and 40 mg of N-hydroxysuccinimide in 4 ml of milliQ water. Finally, the surfaces were rinsed with milliQ water, incubated with ACE2 protein (0.1 µg $µL^{-1}$ in PBS) on Parafilm (Bemis NA), and washed in PBS.

FD-based AFM on model surfaces. FD-based AFM on model surfaces was performed in PBS at room temperature using functionalized MSCT-D probes (Bruker, nominal spring constant of 0.030 N/m and actual spring constants calculated using thermal tune)[31]. A Bioscope Resolve AFM (Bruker) operated in the force–volume (contact) mode (Nanoscope software v9.1) was used. Areas of 5 × 5 µm were scanned, ramp size set to 500 nm, and set point force of 500 pN, with a resolution of 32 × 32 pixels and a line frequency of 1 Hz.

DFS analysis (using a constant approach speed of 1 µm/s and variable retraction speeds of 0.1, 0.2, 1, 5, 10, and 20 µm/s) and kinetic on-rate estimation (measuring the BP for different hold times of 0, 50, 100, 150, 250, 500, and 1000 ms) were performed. Regarding DFS experiments, data including LRs and disruption forces were extracted using Nanoscope analysis (v2.0, Bruker). Origin software (OriginLab) was used to display the results in DFS plots to fit histograms of rupture force distributions for distinct LR ranges, and to apply various force spectroscopy models, as described[8,16]. For kinetic on-rate analysis, the BP (fraction of curves showing binding events) was determined at a certain hold time (t) (the time the tip is in contact with the surface). Those data were fitted and K_D calculated as described previously[32]. In brief, the relationship between interaction time (τ) and

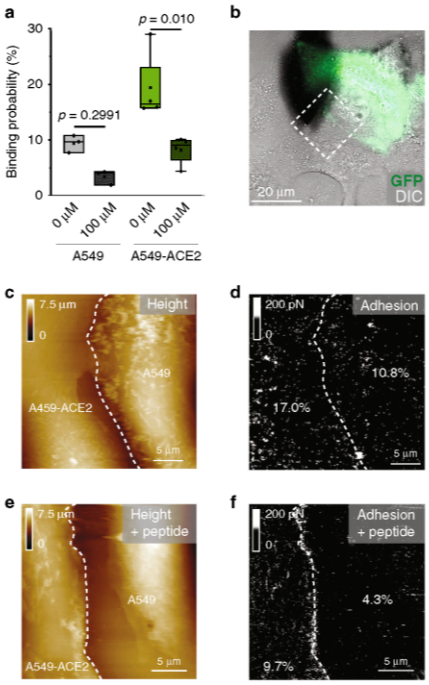

Fig. 5 Blocking of S1-subunit binding using ACE2-derived peptide on living cells. a Box plot showing that the reduction of binding probability measured the S1-subunit-derivatized tip and a mixed culture of A549 and A549-ACE2 cells upon injection of the [22–57] ACE2-derived peptide. The square in the box indicates mean, the colored box indicates the 25th and 75th percentiles, and the whiskers indicate the highest and the lowest values of the results. **b** Overlay of eGFP and DIC images of a mixed culture of A549 and A549-ACE2-eGFP cells. FD-based AFM topography images (**c**, **e**) and the corresponding adhesion map (**d**, **f**) recorded in the specified area in (**b**) (scanned with a scan angle) before (**c**, **d**) and after (**e**, **f**) incubation of the tip with the [22–57] ACE2-derived peptide. The frequency of adhesion events is indicated. Data are representative of at least $N = 4$ cells from $N = 2$ independent experiments. *P* values were determined by two-sample *t* test in Origin. Source data are provided as a Source Data file.

BP is described by the following equation:

$$\mathrm{BP} = A * \left[1 - \exp\left(\frac{-(t - t_0)}{\tau}\right)\right] \quad (1)$$

where A is the maximum BP and t_0 the lag time. Origin software is used to fit the data and extract τ. In the next step, k_{on} was calculated by the following equation, with r_{eff} the radius of the sphere, n_b the number of binding partners, and N_A the Avogadro constant

$$k_{on} = \frac{\frac{1}{2} \cdot 4\pi r_{eff}^3 N_A}{3 n_b \tau} \quad (2)$$

The effective volume V_{eff} ($4\pi r_{eff}^3$) represents the volume in which the interaction can take place. This results in a half-sphere, since only half of the S1 molecules can interact with its corresponding receptor on the substrate.

Peptides and competition-binding assays. To assess the influence of peptides on the S1-subunit–ACE2 interaction, binding probabilities were measured before and after tip incubation with 1, 10, and 100 µM of peptide. Briefly, a first map was recorded as described above (i.e., force-volume mode, 1 µm/s approach and retraction speed, ramp size of 500 nm, an applied force of 500 pN, resolution of 32 × 32 pixels, line frequency of 1 Hz, and hold time of 250 ms), then the peptide at the appropriate concentration was injected, and a new map was recorded.

All the peptides ([22–44], [351–357], [22–57], and [22–44–g–351–357]) were synthesized by Genscript (Hong Kong). Those peptides are designed according to the sequence of the ACE2 receptor in complex with the RBD domain of the S1 glycoprotein.

FD-based AFM and fluorescence microscopy on living cells. An AFM (Bioscope Resolve, Bruker) coupled to a confocal microscope (Zeiss LSM-980) was used to acquire correlative images. The AFM was equipped with a 150-µm piezoelectric scanner. The AFM and the microscope were equipped with a cell-culture chamber allowing maintaining the temperature (37 ± 1 °C). To keep cells alive, the humidified (95 ± 2% relative humidity) synthetic air (80% N_2 and 20% O_2) was supplemented with 5% CO_2 and filled continuously around the cell plate allowing to diffuse into cell-culture media[16]. Fluorescence images were recorded using a water-immersion lens (×63, NA 1.20, Zeiss C-Apochromat). PFQNM-LC cantilevers (Bruker) were used to record AFM images (~25 µm²) at imaging forces of ~500 pN. The cantilevers were oscillated either at 0.25-kHz peak force frequency with a 750-nm amplitude, 0.125 kHz with a 375-nm amplitude in the PeakForce Tapping mode, or at 20 µm s^{-1} retraction speed in fast-force-volume mode. The sample was scanned using 256 pixels per line (256 lines) and a frequency of 0.125 Hz. To study the involvement of other receptors, cells were treated with either 1 mM of 9-O-acetyl-sialogycans or 500 µM of cRGD. AFM images and FD curves were analyzed using Nanoscope analysis software, Origin, Gwyddion, and ImageJ. Optical images were analyzed using Zen software (Zeiss). The fluorescence intensity was measured with Zen software (Zeiss). The same size of the area was taken on A549–ACE2 and A549 cells. The average intensity of the area was calculated with Zen software. The statistical analysis was performed with Prism (Graphpad).

Plasma membrane staining. Plasma membrane-CFP BacMam 2.0 (Invitrogen) was used to check the co-localization of ACE2 protein and plasma membrane according to the manufacturer's protocol. In brief, 2 µl of plasma membrane-CFP BacMam 2.0 per 10,000 cells was added on the cell-culture dish 16 h (37 °C) before imaging. Z-stack image was recorded by confocal LSM-980 (Zeiss) using a water-immersion lens (×63, NA 1.20, Zeiss C-Apochromat) and 445- and 488-nm laser line.

Affinity measurements using BLI. Affinity between the S1 subunit or RBD and ACE2 was also investigated by BLI, using a Blitz® device equipped with amine-reactive second-generation (AR2G) biosensors (Pall ForteBio). After hydrating the biosensor for 10 min and performing an initial baseline (1 min), the biosensor surface was chemically activated (5 min) by a freshly prepared 20 mM EDC and 10 mM NHS (in milliQ water) solution. Then, ACE2 (0.025 µg $µL^{-1}$ in acetate buffer, pH 4) was loaded onto the biosensor during 3 min and the reaction quenched with ethanolamine 1 M (pH 8). After another baseline step (1 min in PBS), binding of S1 subunit or RBD (0.1 mg mL^{-1}) was measured for 5 min. Finally, the dissociation step (5 min) was performed in PBS. Data processing and analysis were run using a routine provided by GraphPad Prism.

MD simulation between ACE2 peptides and S glycoprotein. The PDB (code: 6m0j)[29] was used to perform a MD simulation between ACE2-derived peptides and the SARS-CoV-2 spike protein complex. MD simulations were performed utilizing the Gromacs package[33,34] and carried out using the Amber99SB-ILDN[35] force fields in TIP3P water[36]. The simulation system consisted of a peptide, a protein, and water (about 20,000 molecules) in a cubic box that extended 10 nm from the protein. Appropriate amounts of sodium/chlorine ions were added in the system. For starting the simulation, the environment had to be developed as follows. The steepest descent algorithm was performed either up to 50,000 steps or by 100 kJ mol^{-1} nm^{-1}. Then, the environment of the system changed at 300 K (NVT ensemble) and subsequently at 300 K and 1 bar (NPT ensemble). After developing the environment, the Particle Mesh Ewald[37] method was used to calculate the long-range electrostatic interactions. Short-range dispersion interactions were described by a Lennard–Jones potential with the cutoff of 1 nm. After reaching the equilibrium of temperature and pressure, MDs were conducted for 60 ns at 300 K and 1 bar. The LINCS algorithm[38] was applied to constrain the covalent bonds with hydrogen atoms. The time step of the simulations was set to 2 fs. The interactions above 10 Å were regarded as nonbond. To determine whether a hydrogen bond exists between a peptide and a protein in the MD models, a geometrical criterion was adopted, in which the formation of a hydrogen bond was defined by both atom distance and bond orientation. For example, assuming donor D, hydrogen H, and acceptor A consists of D–H ··· A configuration. Then when the distance between donor D and acceptor A was shorter than 3.5 Å as well as the bond angle H–D ··· A smaller than 60.0°, it has been regarded as a hydrogen bond. The hydrogen bonds are counted for 55–60 ns while running the simulations.

Synthesis of 9-*O*-acetyl-2-α-*O*-propargyl-SC. 2-α-*O*-propargyl SC was synthesized by the protocol described by Dashkan et al.[39]. This molecule was selectively acetylated at the 9-position following the procedure of Ogura et al.[40].

Reporting summary. Further information on research design is available in the Nature Research Reporting Summary linked to this article.

Data availability

The Source data underlying Figs. 2c, e–h, 3f, h, 4b, c, 5a and Supplementary Figs. 2, 6, 7 are provided as a Source Data file. All other relevant data are available from the corresponding authors upon reasonable request. Source data are provided with this paper.

Received: 9 July 2020; Accepted: 18 August 2020;
Published online: 11 September 2020

References

1. Zhou, P. et al. A pneumonia outbreak associated with a new coronavirus of probable bat origin. *Nature* **579**, 270–273 (2020).
2. Tortorici, M. A. & Veesler, D. Structural insights into coronavirus entry. *Adv. Virus Res.* **105**, 93–116 (2019).
3. Yan, R. et al. Structural basis for the recognition of SARS-CoV-2 by full-length human ACE2. *Science* **367**, 1444 (2020).
4. Gallagher, T. M. & Buchmeier, M. J. Coronavirus spike proteins in viral entry and pathogenesis. *Virology* **279**, 371–374 (2001).
5. Simmons, G., Zmora, P., Gierer, S., Heurich, A. & Pohlmann, S. Proteolytic activation of the SARS-coronavirus spike protein: cutting enzymes at the cutting edge of antiviral research. *Antivir. Res.* **100**, 605–614 (2013).
6. Millet, J. K. & Whittaker, G. R. Host cell proteases: critical determinants of coronavirus tropism and pathogenesis. *Virus Res.* **202**, 120–134 (2015).
7. Alsteens, D. et al. Imaging G protein-coupled receptors while quantifying their ligand-binding free-energy landscape. *Nat. Methods* **12**, 845–851 (2015).
8. Koehler, M. et al. Glycan-mediated enhancement of reovirus receptor binding. *Nat. Commun.* **10**, 1–14 (2019).
9. Newton, R. et al. Combining confocal and atomic force microscopy to quantify single-virus binding to mammalian cell surfaces. *Nat. Protoc.* **12**, 2275 (2017).
10. Delguste, M. et al. Multivalent binding of herpesvirus to living cells is tightly regulated during infection. *Sci. Adv.* **4**, eaat1273 (2018).
11. Rankl, C. et al. Multiple receptors involved in human rhinovirus attachment to live cells. *Proc. Natl Acad. Sci. USA* **105**, 17778–17783 (2008).
12. Dobrowsky, T. M., Zhou, Y., Sun, S. X., Siliciano, R. F. & Wirtz, D. Monitoring early fusion dynamics of human immunodeficiency virus type 1 at single-molecule resolution. *J. Virol.* **82**, 7022–7033 (2008).
13. Bell, G. I. Models for the specific adhesion of cells to cells. *Science* **200**, 618–627 (1978).
14. Evans, E., Ritchie, K. & Merkel, R. Sensitive force technique to probe molecular adhesion and structural linkages at biological interfaces. *Biophys. J.* **68**, 2580–2587 (1995).
15. Evans, E. & Ritchie, K. Dynamic strength of molecular adhesion bonds. *Biophys. J.* **72**, 1541–1555 (1997).
16. Alsteens, D. et al. Nanomechanical mapping of first binding steps of a virus to animal cells. *Nat. Nanotechnol.* **12**, 177–183 (2017).
17. Sieben, C. et al. Influenza virus binds its host cell using multiple dynamic interactions. *Proc. Natl Acad. Sci. USA* **109**, 13626–13631 (2012).
18. Wrapp, D. et al. Cryo-EM structure of the 2019-nCoV spike in the prefusion conformation. *Science* **367**, 1260–1263 (2020).
19. Shang, J. et al. Structural basis of receptor recognition by SARS-CoV-2. *Nature* **581**, 221–224 (2020).
20. Li, W. et al. Angiotensin-converting enzyme 2 is a functional receptor for the SARS coronavirus. *Nature* **426**, 450–454 (2003).
21. Dimitrov, D. S. Virus entry: molecular mechanisms and biomedical applications. *Nat. Rev. Microbiol.* **2**, 109–122 (2004).
22. Harcourt, J. et al. Isolation and characterization of SARS-CoV-2 from the first US COVID-19 patient. Preprint at *bioRxiv* https://doi.org/10.1101/2020.03.02.972935v1 (2020).
23. Jia, H. P. et al. ACE2 receptor expression and severe acute respiratory syndrome coronavirus infection depend on differentiation of human airway epithelia. *J. Virol.* **79**, 14614–14621 (2005).
24. Tortorici, M. A. et al. Structural basis for human coronavirus attachment to sialic acid receptors. *Nat. Struct. Mol. Biol.* **26**, 481–489 (2019).
25. Sigrist, C. J., Bridge, A. & Le Mercier, P. A potential role for integrins in host cell entry by SARS-CoV-2. *Antivir. Res.* **177**, 104759 (2020).
26. Prystopiuk, V. et al. Mechanical forces guiding *Staphylococcus aureus* cellular invasion. *ACS Nano* **12**, 3609–3622 (2018).
27. Zhang, H., Penninger, J. M., Li, Y., Zhong, N. & Slutsky, A. S. Angiotensin-converting enzyme 2 (ACE2) as a SARS-CoV-2 receptor: molecular mechanisms and potential therapeutic target. *Intensive Care Med.* **46**, 586–590 (2020).
28. Monteil, V. et al. Inhibition of SARS-CoV-2 infections in engineered human tissues using clinical-grade soluble human ACE2. *Cell* **181**, 905–913 (2020).
29. Lan, J. et al. Structure of the SARS-CoV-2 spike receptor-binding domain bound to the ACE2 receptor. *Nature* **581**, 215–220 (2020).
30. Wildling, L. et al. Linking of sensor molecules with amino groups to amino-functionalized AFM tips. *Bioconj. Chem.* **22**, 1239–1248 (2011).
31. Butt, H. J. & Jaschke, M. Calculation of thermal noise in atomic force microscopy. *Nanotechnology* **6**, 1–7 (1995).
32. Rankl, C. et al. Determination of the kinetic on- and off-rate of single virus-cell interactions. *Methods Mol. Biol.* **736**, 197–210 (2011).
33. Berendsen, H. J. C., van der Spoel, D. & van Drunen, R. GROMACS: a message-passing parallel molecular dynamics implementation. *Comput. Phys. Commun.* **91**, 43–56 (1995).
34. Lindahl, E., Hess, B. & van der Spoel, D. GROMACS 3.0: a package for molecular simulation and trajectory analysis. *J. Mol. Model.* **7**, 306–317 (2001).
35. Lindorff-Larsen, K. et al. Improved side-chain torsion potentials for the Amber ff99SB protein force field. *Proteins* **78**, 1950–1958 (2010).
36. Jorgensen, W. L., Chandrasekhar, J., Madura, J. D., Impey, R. W. & Klein, M. L. Comparison of simple potential functions for simulating liquid water. *J. Chem. Phys.* **79**, 926–935 (1983).
37. Essmann, U. et al. A smooth particle mesh Ewald method. *J. Chem. Phys.* **103**, 8577–8593 (1995).
38. Hess, B. P-LINCS: a parallel linear constraint solver for molecular simulation. *J. Chem. Theory Comput.* **4**, 116–122 (2008).
39. Daskhan, G. C., Pifferi, C. & Renaudet, O. Synthesis of a new series of sialylated homo-and heterovalent glycoclusters by using orthogonal ligations. *ChemistryOpen* **5**, 477–484 (2016).
40. Ogura, H. et al. Synthesis of 9-O-acyl-and 4-O-acetyl-sialic acids. *Carbohydr. Res.* **167**, 77–86 (1987).
41. Fiser, A. & Šali, A. Modeller: generation and refinement of homology-based protein structure models *Methods Enzymol.* **374**, 461–491 (2003).

Acknowledgements

This work was supported by the Université catholique de Louvain, the Foundation Louvain, and the Fonds National de la Recherche Scientifique (FRS-FNRS). This project received funding from the European Research Council under the European Union's Horizon 2020 research and innovation program (grant agreement No. 758224) and from the FNRS-Welbio (Grant # CR-2019S-01). The funders had no role in study design, data collection and analysis, decision to publish, or preparation of the paper. S.P., A.C.D., and D.A. are research fellow, postdoctoral researcher, and research associate at the FNRS, respectively. Q.Z., W.C., and S.P.V. are grateful to China Scholarship Council. Cartoons in Figures 1a–c, 2a, d, 3a, and 4a were created with BioRender.com.

Author contributions

J.Y., S.J.L.P., M.K., A.C.D., and D.A. conceived the project, planned the experiments, and analyzed the data. J.Y., S.J.L.P., and S.D. conducted the AFM experiments. Q.Z. performed MD simulation and structure predictions. S.P., M.K., and P.S. conducted and analyzed the BLItz experiments. W.C. and S.P.V. conceived and synthesized the SA derivative. All authors wrote the paper.

Competing interests

The authors declare no competing interests.

Additional information

Supplementary information is available for this paper at https://doi.org/10.1038/s41467-020-18319-6.

Correspondence and requests for materials should be addressed to D.A.

Peer review information *Nature Communications* thanks the anonymous reviewers for their contribution to the peer review of this work. Peer reviewer reports are available.

Reprints and permission information is available at http://www.nature.com/reprints

Publisher's note Springer Nature remains neutral with regard to jurisdictional claims in published maps and institutional affiliations.

Supplementary Information for

Molecular interaction and inhibition of SARS-CoV-2 binding to the ACE2 receptor

Yang *et al*.

This PDF file includes:

Supplementary Figures 1 to 10

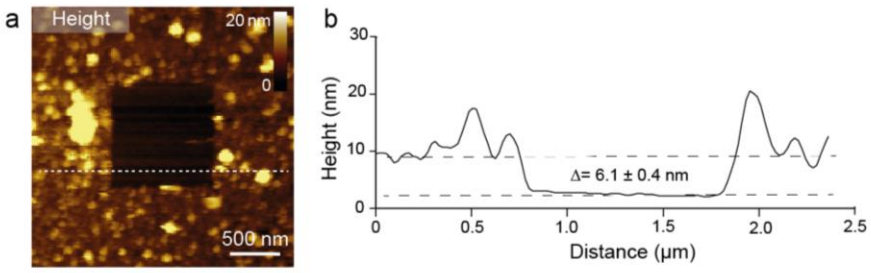

Supplementary Figure 1. Validation of surface immobilization. (**a**) AFM topography image of an ACE2 coated surface after scanning a 1 µm x 1 µm area at high forces (~ 18 nN) to remove the attached biomolecules. (**b**) Cross-section taken along the white dashed line in **a**. The biomolecule-free surface inside the square was ~ 6.1 nm lower in height than the surrounding biomolecule-coated surface, providing an estimate of the thickness of the ACE2 deposited layer. The experiment was repeated 3 times with 3 independent sample preparations.

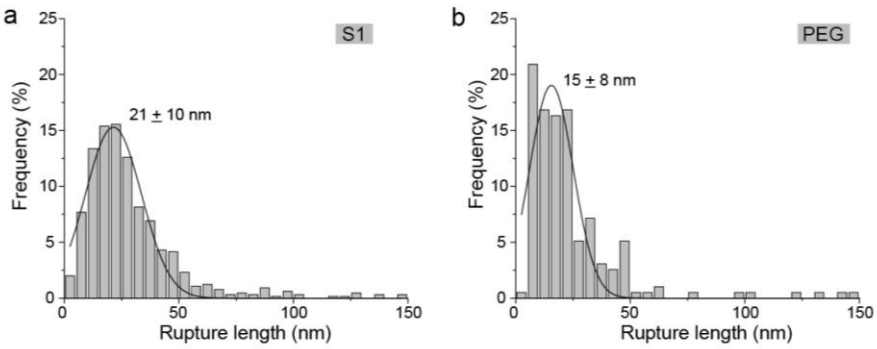

Supplementary Figure 2. Rupture length analysis. Histogram of rupture length for the (**a**) S1-subunit – ACE2 interaction (N = 654 data points) as well as for the (**b**) PEG – ACE2 interaction (N = 196 data points). Multipeak Gaussian fit reveal a maximum of the rupture force at 21 ± 10 nm for the S1-ACE2 interaction and 15 ± 8 nm for the PEG-ACE2 interaction. Source data are provided as a Source Data file.

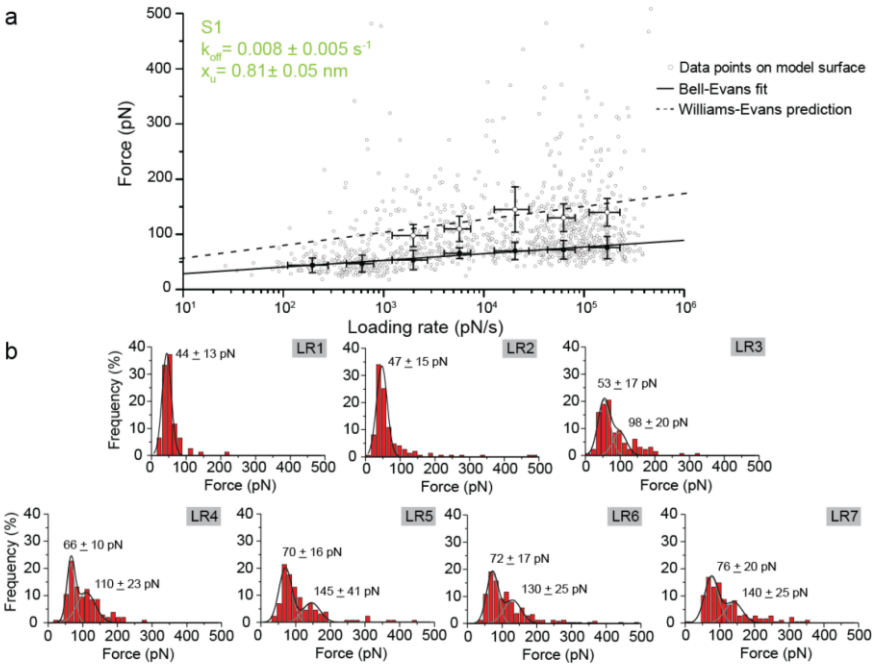

Supplementary Figure 3. Probing S1 binding to ACE2 host receptor on model surface. (**a**) Full-range (0-500 pN) DFS plot showing the distribution of rupture forces measured between S1 and ACE2 coated model surface (grey dots) with average rupture forces determined for seven distinct LR ranges (**b**). Data points corresponding to single interactions are fitted with the Bell-Evans model (black line), whereas the dashed line represent the predicted binding forces for two simultaneous uncorrelated interactions (Williams-Evans model). The error bar indicates s.d. of the mean value. (**b**) Force and LR were extracted from force-distance and force-time curves and sorted in narrow LR ranges (LR1-LR7). The rupture forces for each LR range were plotted as histograms and fitted with multipeak Gaussian fits. N = 1052 from 4 independent experiments.

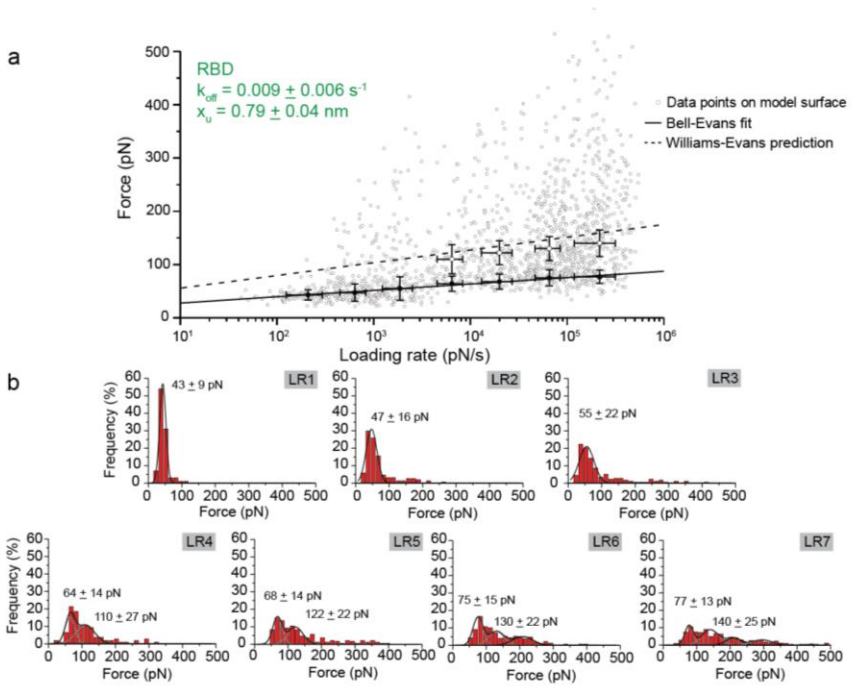

Supplementary Figure 4. Probing RBD binding to ACE2 host receptor on model surface. (**a**) Full-range (0-500 pN) DFS plot showing the distribution of rupture forces measured between RBD and ACE2 coated model surface (grey dots) with average rupture forces determined for seven distinct LR ranges (**b**). Data points corresponding to single interactions are fitted with the Bell-Evans model (black line), whereas the dashed line represent the predicted binding forces for two simultaneous uncorrelated interactions (Williams-Evans model). The error bar indicates s.d. of the mean value. (**b**) Force and LR were extracted from force-distance and force-time curves and sorted in narrow LR ranges (LR1-LR7). The rupture forces for each LR range were plotted as histograms and fitted with multipeak Gaussian fits. N = 1490 from 4 independent experiments.

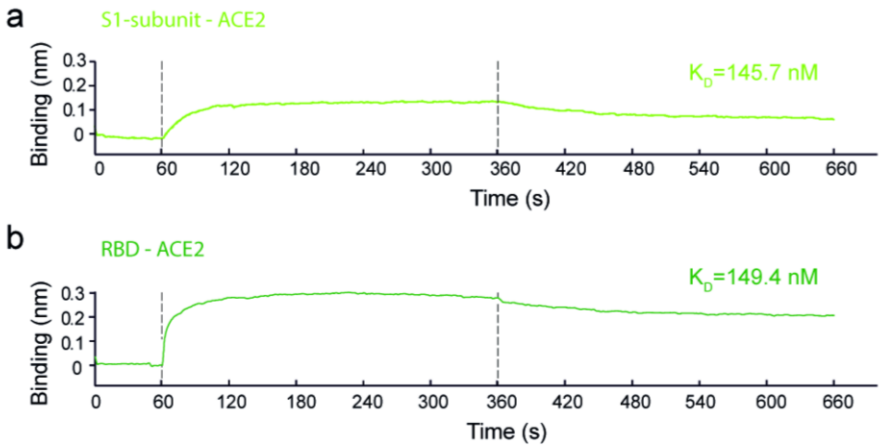

Supplementary Figure 5. Biolayer interferometry data for the binding of S1-subunit and RBD on ACE2 receptors. After a baseline, sensorgram starts with the association (at 60 s) of S1-subunit (**a**) or RBD (**b**) on the ACE2 sensor, followed by the dissociation phase (at 360 s).

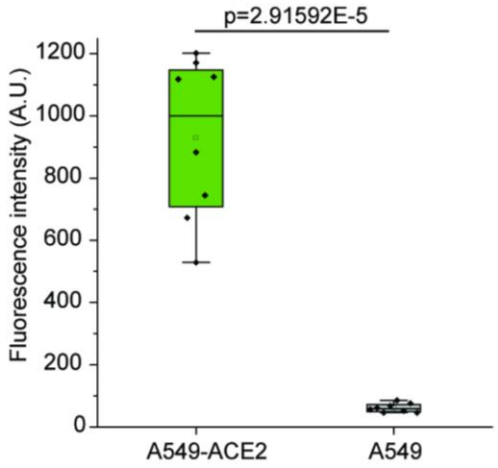

Supplementary Figure 6. Fluorescence intensity of ACE2 transfected (A549-ACE2, green) versus non-transfected (A549, grey) cells. The fluorescence intensity was measured with Zen 3.1 (Zeiss). The same size of area was taken on transfected cells (A549-ACE2) and non-transfected cells (A549) and the average intensity of the area was calculated with Zen 3.1. The statistical analysis was performed with Prism (Graphpad). One data point belongs to the BP from one map acquired at 1 µm/s retraction speed. The square in the box indicates mean, the colored box indicates the 25th and 75th percentile, and the whiskers indicates the highest and the lowest values of the results. The line in the box indicates median. N = 8 cells examined over 3 independent experiments. P-value were determined by two-sample t-test in Origin. Source data are provided as a Source Data file.

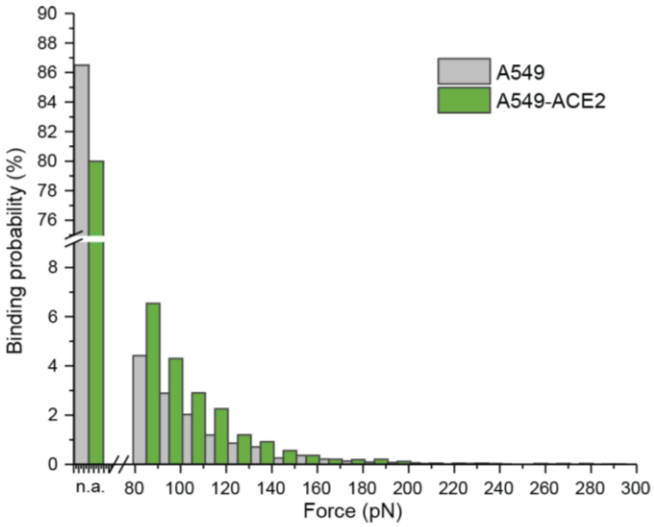

Supplementary Figure 7. Histogram of force distribution extracted on A549 and A549-ACE2 cells (from Fig. 3e). N = 1362 curves on A549-ACE2 cells and N = 891 curves on A549 cells examined over 1 independent experiment. Source data are provided as a Source Data file.

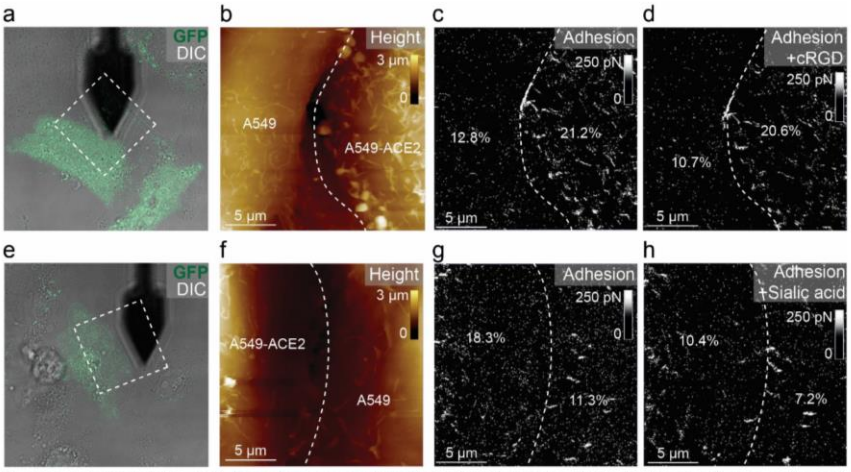

Supplementary Figure 8. Injection experiment to block interactions between living cells and integrins (a-d) or sialic acid (e-h) respectively. (**a**) Overlay of eGFP and DIC images of a mixed culture of A549 and A549-ACE2-eGFP cells. FD-based AFM topography image (**b**) and corresponding adhesion maps (**c,d**) recorded in the specified area in a (scanned with a scan angle) before (**c**) and after (**d**) injection of cRGD to block cell surface exposed integrins. (**e**) Overlay of eGFP and DIC images of a mixed culture of A549 and A549-ACE2-eGFP cells. FD-based AFM topography image (**f**) and corresponding adhesion maps (**g,h**) recorded in the specified area in a (scanned with a scan angle) before (**g**) and after (**h**) injection of sialic acid to block cell surface exposed integrins. The data is representative for at least N = 4 cells from N = 2 independent experiments.

[22-44]	EEQAKTFLDKFNHEAEDLFYQSS
[22-57]	EEQAKTFLDKFNHEAEDLFYQSSLASWNYNTNITEE
[22-44-g 351-357]	EEQAKTFLDKFNHEAEDLFYQSS G LGKGDFR
[351-357]	LGKGDFR

Supplementary Figure 9. Sequences of ACE2-derived peptides.

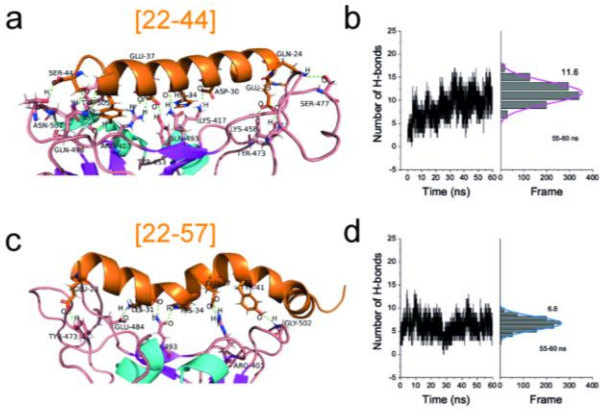

Supplementary Figure 10. Steered Molecular Dynamics (SMD) of ACE2-derived peptides in complex with the RBD. Conformation of peptide 22-44 (**a**) and 22-57 (**c**) in complex with the RBD domain is simulated during 60 ns. During this time frame the number of H-bonds is monitored (**b, d**).